Simulacija promjene opterećenja Francisove hidrauličke turbine

Živković, Dario

Master's thesis / Diplomski rad

2016

Degree Grantor / Ustanova koja je dodijelila akademski / stručni stupanj: **University of Zagreb, Faculty of Mechanical Engineering and Naval Architecture / Sveučilište u Zagrebu, Fakultet strojarstva i brodogradnje**

Permanent link / Trajna poveznica: https://urn.nsk.hr/urn:nbn:hr:235:013186

UNIVERSITY OF ZAGREB
Faculty of Mechanical Engineering and Naval Architecture

MASTER'S THESIS

Dario Živković

Zagreb, 2016.

UNIVERSITY OF ZAGREB
Faculty of Mechanical Engineering and Naval Architecture

SIMULATION OF FRANCIS HYDRAULIC TURBINE LOAD VARIATION

Supervisor:
Assoc. Prof. dr. sc. Željko Tuković

Student:
Dario Živković

Zagreb, 2016.

Acknowledgements

I express sincere gratitude to my supervisor professor Željko Tuković for his time, helpful suggestions and support in making this thesis, especially for always being ready to share knowledge and insights about computational simulations of turbomachinery and the use of foam-extend.

Dario Živković

I hereby declare that this thesis is entirely the result of my own work except where otherwise indicated. I have fully cited all used sources and I have only used the ones given in the list of references.

Dario Živković

SVEUČILIŠTE U ZAGREBU
FAKULTET STROJARSTVA I BRODOGRADNJE
Središnje povjerenstvo za završne i diplomske ispite
Povjerenstvo za diplomske ispite studija strojarstva za smjerove:
procesno-energetski, konstrukcijski, brodostrojarski i inženjersko modeliranje i računalne simulacije

Sveučilište u Zagrebu Fakultet strojarstva i brodogradnje	
Datum	Prilog
Klasa:	
Ur.broj:	

DIPLOMSKI ZADATAK

Student: Dario Živković Mat. br.: 0035173143

Naslov rada na hrvatskom jeziku: **Simulacija promjene opterećenja Francisove hidrauličke turbine**

Naslov rada na engleskom jeziku: **Simulation of load variation of Francis hydraulic turbine**

Opis zadatka:

With the introduction of intermittent energy sources, such as wind and solar power, the need for grid modulation has increased. When hydroelectric power plants are used to stabilize the electric grid, operating conditions of hydraulic turbines need to change on daily basis what significantly affect their operating life. Therefore, the study of transient operation and off-design performance of hydraulic turbines is becoming increasingly important. Computational fluid dynamic (CFD) techniques have been used to study the flow conditions inside hydraulic turbines over the past three decades. Numerical modelling of hydraulic turbines during transient operating conditions is one of the most challenging tasks due to movement of guide vanes and need for dynamic computational mesh. Such numerical models verified with experimental data are still very rare.

In the scope of this thesis, CFD simulation of the Francis-99 turbine transient operation will be performed using open-source finite volume code FOAM-extend. The Francis-99 turbine is a scaled model of a prototype turbine at the Tokke power plant in Norway. It is a high-head Francis turbine consisting of 30 runner blades of which 15 are splitter blades of half length. In the distributor there are 14 stay vanes and 28 guide vanes. The geometry of the turbine together with detailed experimental measurements are freely available at https://www.ntnu.edu/nvks/francis-99. Flow simulation will be performed for load reduction phase where turbine output power is reduced from the best efficiency point to the part load by changing the guide vanes angle from 9.84° to 6.72°. Operating conditions used in the numerical model will be adjusted to the conditions of the corresponding experimental measurements. Numerical solution will be compared with available experimental data.

It is advised to list references used in this work, as well as to acknowledge help and support possibly received during the course of this study.

Zadatak zadan:	Rok predaje rada:	Predviđeni datumi obrane:
29. rujna 2016.	1. prosinca 2016.	7., 8. i 9. prosinca 2016.

Zadatak zadao: Predsjednica Povjerenstva:

Izv.prof.dr.sc. Željko Tuković

Prof. dr. sc. Tanja Jurčević Lulić

Uz.

Table of Contents

Nomenclature

Greek letters

α	Guide vane angle	$^\circ$
ε	Dissipation of turbulence kinetic energy	m^2/s^3
η	Turbine efficiency	–
Γ	Diffusion coefficient	–
γ	Mesh diffusion coefficient	–
ν	Kinematic viscosity	m^2/s
ν_t	Turbulent kinematic viscosity	m^2/s
ν_{eff}	Effective kinematic viscosity	m^2/s
ω	Dissipation of turbulence kinetic energy	s^{-1}
Φ	Passive scalar quantity	-
ρ	Fluid density	kg/m^3
ω	Angular velocity vector	s^{-1}

Latin letters

$\mathbf{u}$	Velocity vector	m/s
$\mathbf{u}_r$	Relative velocity	m/s
$\overline{\mathbf{u}}$	Mean velocity	m/s
$\mathbf{u}'$	Fluctuating velocity	m/s
$\mathbf{a}$	Axis vector	-
$\mathbf{I}$	Identity tensor	–
$\mathbf{n}$	Unit normal vector	-
$\mathbf{r}, \mathbf{x}$	Position vector	-
$\mathbf{u}_S$	Velocity of boundary surface	-

$d_i/\ d_o$	Inlet/outlet diameter	m
g	Gravitational acceleration	m/s^2
H	Head	m
I	Turbulence intensity	–
k	Turbulence kinetic energy	m^2/s^2
l	Turbulence mixing length	m
n	Revolutions per minute	min^{-1}
P	Turbine power	W
p	Kinematic pressure	m^2/s^2
p_0	Kinematic pressure	Pa
Q	Flow rate	m^3/s
S_Φ	Source term of quantity Φ	–
T	Torque	Nm
t	Time	s
T_f	Friction torque	Nm
U_θ	Tangential velocity	m/s
U_r	Radial velocity	m/s
x, y, z	Coordinate axes	–

List of Figures

List of Tables

ABSTRACT

SIMULATION OF FRANCIS HYDRAULIC TURBINE LOAD VARIATION

Dario Živković

Due to intermittentcy in electrical grids introduced with ever larger share of renewable power sources, hydroelectric plant operation saw an increase in load variations and overall off-design operation at prolonged time as they are expected to deliver regulating power for the electric grid. Frequent load variations increased the dynamic loading of turbine parts, particularly runner, affecting the operating life and increasing maintenance-related cost. Detailed studies of transient operating regimes are therefore necessary.

In present work, methods of computational fluid mechanics are applied on Francis 99 high head turbine using the open source finite volume code `foam-extend`. Simulations of both steady state and transient turbine operation were performed. Best efficiency operating point is simulated with both steady-state solver with frozen rotor approach, as well as a transient dynamic mesh solver implementing sliding grid approach. The steady operation simulations were conducted first to test the created mesh and computational modeling choices.

Load variation simulations are implemented for load reduction phase, where discharge is regulated by closing of guide vanes from best efficiency point to part load. Two approaches with custom boundary conditions were tested for the domain inlet, one with prescribed head (total pressure) and another with prescribed flow rate (velocity). The simulation with prescribed head showed good agreement with pressure measurements and realistic trend of other integral values.

Two well established turbulence models were used in present work, namely the "standard" $k-\varepsilon$ and $k-\omega$ SST. All parameters in setup of presented simulations were adjusted to the corresponding conditions during experiments on the Tokke turbine model, results of which were made available by the Francis 99 workshop.

Keywords: Francis 99, load variation simulations, computational fluid dynamics (CFD), mesh motion, turbomachinery, Hydroturbines.

SAŽETAK

(ABSTRACT IN CROATIAN)

SIMULACIJA PROMJENE OPTEREĆENJA FRANCISOVE HIDRAULIČKE TURBINE

Dario Živković

Sve većim udjelom intermitentnih izvora energije povećava se potreba za čestim promjenama radnog režima hidroturbinskih postrojenja. Povećan rad u vanprojektnim radnim točkama, potrebe za variranjem snage i općenito sudjelovanje u pomoćnim uslugama regulacije napona elektroenergetskog sustava uvjeti su s kojima se susreću hidrauličke turbine danas. Sve to uzrokuje dinamička naprezanja s posljedicama po životni vijek i sigurnost rada postrojenja te veće troškove održavanja.

U ovom radu upotrebljavaju se metode računalne dinamike fluida kako bi se analizirao tok u Francis 99 modelu visokotlačne turbine prilikom prijelaznih režima rada. Za tu svrhu korišten je open source kôd `foam-extend`. Prikazane su simulacije radne točke najviše iskoristivosti te simulacije promjene režima rada zakretanjem lopatica statora. Blok strukturirana heksaedarska računalna mreža izrađena je ručno za potrebe rada. Metoda pomičnih koordinatnih sustava te metoda rotacije mreže su korištene za simuliranje stacionarne radne točke.

Zakretanje regulacijskih lopatica statora iz nazivne radne točke u točku smanjene snage modelirano je rješavanjem jednadžbi gibanja točaka geometrijske mreže kontrolnih volumena. Dva pristupa zadavanju rubnih uvjeta su testirana, sa zadanom visinom tlaka te zadanim protokom na ulazu. Simulacija sa zadanom visinom tlaka pokazala je zadovoljavajuće rezultate u usporedbi s eksperimentalnim podacima.

Modeli turbulencije korišteni u radu su "standardni" $k-\varepsilon$ i $k-\omega$ SST. Svi parametri u postavkama numeričkih simulacija odgovaraju uvjetima koji su vladali prilikom eksperimentalnih mjerenja objavljenih od strane organizatora Francis 99 konferencije.

Ključne riječi: Francis 99, promjena režima rada, računalna dinamika fluida (CFD), pomične mreže kontrolnih volumena, turbostrojevi, hidroturbine.

Prošireni sažetak na hrvatskom

(EXTENDED ABSTRACT IN CROATIAN)

1. Uvod

Promjenama na tržištima električne energije zemalja Europske unije zbog sve većeg udjela intermitentnih obnovljivih izvora značajno se mijenja pozicija hidroelektrana i uvjeti njihova rada. Sve više se očekuje sudjelovanje u reguliranju napona elektroenergetskog sustava i skladištenju energije. Rezultat toga su česte promjene opterećenja hidroturbinskih postrojenja, sve dulji rad u vanprojektnim režimima, brže promjene radne točke te velik broj ciklusa pokretanja i zaustavljanja. Sve ovo uzrokuje povećana dinamička naprezanja i skraćuje životni vijek komponenti, posebice kod turbina Francisova tipa, bez mogućnosti zakretanja rotorskih lopatica. U rasponu radnih režima turbine, različite pojave se javljaju u strujanju. Interakcija rotora i statora, vrtloženje u izlaznom kanalu, kavitacija, odvajanje strujanja, itd. Kompleksnost međudjelovanja ovih pojava i čestih promjena režima rada dovodi do potrebe za detaljnim analizama strujanja za vrijeme prijelaznih pojava.

Računalna dinamika fluida važan je alat u analizi i projektiranju turbostrojeva već desetljećima, tako i u rješavanju ovdje navedenih izazova zauzima važno mjesto. Na tragu toga pokrenuta je međunarodna konferencija "Francis 99", organizirana od strane Norveškog sveučilišta znanosti i tehnologije (NTNU) i Luela Sveučilišta u Švedskoj. Za potrebe konferencije otvoren je pristup tehničkoj dokumentaciji, CAD modelima i rezultatima eksperimenata modela turbine instalirane u hidroelektrani *Tokke* u Norveškoj.

Na modelu Francis 99 turbine, u sklopu ovoga rada bit će testiran pristup simuliranju promjene režima rada spomenute turbine upotrebom open source alata za računalnu dinamiku fluida `foam-extend`, točnije njegovim mogućnostima računanja na pomičnim mrežama. Rezultati proračuna uspoređeni su s eksperimentalnim podacima.

2. Numerički model

Model nestlačivog strujanja

Strujanje vode u hidrauličkim turbinama može se opisati jednadžbama gibanja nestlačivog fluida. Strujanje je turbulentno pa se za matematički opis koristi sustav osrednjenih Navier-

Stokesovih jednadžbi. Jednadžba kontinuiteta (zakon očuvanja mase) glasi:

$$\nabla \bullet \overline{\mathbf{u}} = 0 \tag{1}$$

dok je zakon očuvanja količine gibanja:

$$\frac{\partial \overline{\mathbf{u}}}{\partial t} + \nabla \bullet (\overline{\mathbf{u}}\,\overline{\mathbf{u}}) = \nabla \bullet (\nu \nabla \overline{\mathbf{u}}) - \nabla p + \nabla \bullet (-\overline{\mathbf{u}'\mathbf{u}'}) \tag{2}$$

gdje je $\overline{\mathbf{u}}$ osrednjena brzina, ρ gustoća, ν kinemtička viskoznost i p kinemtički tlak.

Cilj je modela turbulencije aproksimirati tenzor Reynoldsovog naprezanja $\overline{\mathbf{u}'\mathbf{u}'}$ koji se pojavljuje u jednadžbi (2) pomoću poznatih varijabli strujanja. Korišten je pristup u kojem se odnos između gradijenta prosječne brzine i Reynoldsova naprezanja pretpostavlja linearnim, korištenjem Boussinesqove hipoteze (jed. 3).

$$\overline{\mathbf{u}'\mathbf{u}'} = \nu_t \left[\nabla \mathbf{u} + (\nabla \mathbf{u})^{\mathrm{T}}\right] + \frac{2}{3} k \mathbf{I} \tag{3}$$

gdje ν_t predstavlja turbulentnu viskoznost, $\mathbf{I}$ je jedinični tenzor, a

$$k = \frac{1}{2}\,\overline{\mathbf{u}' \bullet \mathbf{u}'} \tag{4}$$

se definira kao turbulentna kinetička energija.

Turbulentna viskoznost je funkcija turbulentne kinetičke energije k i njezine disipacije ε ili specifične disipacije ω (ovisno o modelu turbulencije). Ove veličine se aproksimiraju pomoću "standardnog" $k-\varepsilon$ ili $k-\omega$ *SST* modela turbulencije te upotrebom zidnih funkcija u području uz čvrstu nepropusnu stijenku na koju se lijepi fluid.

Način na koji je modelirano gibanje rotora od posebnog je interesa u simulacijama turbostrojava. U ovom radu korištena su slijedeća dva pristupa:

- *rotirajući koordinatni sustav (eng. multiple reference frames)*, poznat kao i *model zamrznutog rotora,* kod kojeg se zadana rotirajuća zona rješava prema modificiranom matematičkom modelu, dodavanjem utjecaja Coriolisovog ubrzanja i centrifugalne sile. Jednadžba (5) prikazuje modificirane jednadžbe toka.

$$\frac{\partial \mathbf{u}}{\partial t} + \nabla \bullet (\mathbf{u}_r \mathbf{u}) + \omega \times \mathbf{u} = -\nabla p + \nabla \bullet (\nu \nabla \mathbf{u}) \tag{5}$$

  gdje je $\mathbf{u}$ apsolutna brzina, $\mathbf{u}_r$ relativna brzina (u rotirajućem koordinatnom sustavu) i ω vektor kutne brzine. Relativna brzina se definira kao

$$\mathbf{u}_r = \mathbf{u} - \omega \times \mathbf{r} \tag{6}$$

- *Rotirajuća mreža kontrolnih volumena* je drugi pristup korišten u ovom radu, kod njega se rotirajuća zona u numeričkoj simulaciji rješava pomakom mreže u svakom vremenskom koraku simulacije. Ova metoda ograničena je na tranzijentne simulacije i zahtjeva veće računalne resurse. Međutim, daje realističnije razultate za proučavanje interakcije rotora i statora.

Na granicama proračunske domene postavljaju se Dirichletovi ili Neumannovi granični uvjeti, ili njihova kombinacija. U računalnoj mehanici fluida granični uvjeti postavljaju se ovisno o tipu granice (ulaz u domenu, izlaz iz domene proračuna, nepropusna granica, itd.). Osim standardnih graničnih uvjeta implementiranih u `foam-extend` računalnom kôdu, u ovom radu bilo je potrebno koristiti i posebne granične uvjete za brzinu fluida na ulaznoj površini u domenu. Prema jednadžbi (7) zadaje se ulazna brzina na cilindričnoj površini, iz zadanih parametara radijalne $\|\mathbf{u}_r\|$, tangencijalne $\|\mathbf{u}_t\|$ i aksijalne $\|\mathbf{u}_a\|$ vrijednosti komponente vektora brzine.

$$\mathbf{u}_{inlet} = \|\mathbf{u}_a\|\hat{\mathbf{a}} + \|\mathbf{u}_t\|\frac{\mathbf{r}\times\hat{\mathbf{a}}}{\|\mathbf{r}\times\hat{\mathbf{a}}\|} + \|\mathbf{u}_r\|\frac{\mathbf{d}\times\hat{\mathbf{a}}}{\|\mathbf{d}\times\hat{\mathbf{a}}\|} \tag{7}$$

gdje je $\hat{\mathbf{a}}$ os cilindrične površine, a vektor $\mathbf{d} = \mathbf{r} - \hat{\mathbf{a}}(\mathbf{r}\bullet\hat{\mathbf{a}})$.

U nekim slučajevima zadaje se smjer vektora brzine, dok je iznos izračunat iz razlike tlaka. Ovaj granični uvjet definiran je jednadžbom 8.

$$\hat{\mathbf{u}}_{inlet} = \frac{\mathbf{u}_{inlet}}{\|\mathbf{u}_{inlet}\|} \tag{8}$$

gdje je $\mathbf{u}_{inlet}$ definiran u jednadžbi (7).

Modeliranje zakretanja statorskih lopatica

U svrhu simulacije promjene radnog režima turbine potrebno je modelirati zakretanje regulacijskih statorskih lopatica. Koristi se matematički model pomične mreže, implementiran u `foam-extend` koji rješava pomake točaka geometrijske mreže kontrolnih volumena pomoću Laplacove jednadžbe:

$$\nabla\bullet(\gamma\,\nabla\mathbf{u}) = 0 \tag{9}$$

gdje $\mathbf{u}$ je brzina jedne točke u mreži kontrolnih volumena i γ koeficijent difuzije. Položaji točaka se određuju prema jednadžbi (10).

$$\mathbf{x}_t = \mathbf{x}_{t-1} + \mathbf{u}\Delta t \tag{10}$$

gdje x predstavlja vektor položaja točke u kartezijanskom koordinatnom sustavu, a Δt je vremenski korak.

Difuzivnost mreže γ može biti konstantna ili funkcija udaljenosti od pomične granice. Prilikom gibanja mreže ovom metodom može doći do narušavanja parametara koji određuju kvalitetu proračunske mreže. Cilj promjenjive difuzivnosti je kontrolirati ovu degradaciju. Iz istog je razloga u ovom radu korišten i pristup zamjene mreže u trenutku kada kvaliteta postane nedovoljna za rješavanje modela strujanja. Nova ručno izrađena mreža se učitava na tom položaju te se simulacija nastavlja nakon mapiranja rezultata sa stare mreže.

Mreža za metodu kontrolnih volumena se može sastojati od proizvoljnih poliedarskih elemenata. Jednadžba (9) diskretizirana je na mreži tetraedara koja se dobije dekompozicijom originalne poliedarske mreže u prethodnom koraku. Rješavanje jednadžbe vrši se Galerkinovom metodom konačnih elemenata. Rješenje se postiže upotrebom "Incomplete Cholesky Preconditioned Conjugate Gradient" iterativnog postupka rješavanja linearnog sustava algebarskih jednadžbi.

Pomicanje mreže zadano je rubnim uvjetima na odabranim granicama, u ovom radu to su površine regulacijskih lopatica statora. Konstantna kutna brzina i zadaje se u $^\circ/s$. Izraz za brzinu točaka na lopatici izveden je iz Rodriguesove formule za rotaciju:

$$\mathbf{u}_i = \frac{\mathbf{p}_0 - \mathbf{p}_{i-1} + \hat{\mathbf{a}}(\hat{\mathbf{a}}\bullet\mathbf{p}_0)(1-cos\alpha_i) + (\hat{\mathbf{a}}\times\mathbf{p}_0)sin\alpha_i + \mathbf{p}_0(cos\alpha_i - 1)}{\Delta t} \tag{11}$$

gdje je

$$\alpha_i = \omega\frac{\pi}{180}(t_i - t_0) \tag{12}$$

kut zakretanja u jednom vremenskom koraku određen zadanom kutnom brzinom $\omega = \frac{d\alpha}{dt}$. $\mathbf{p}_0$ je vektor položaja točke, $\mathbf{p}_{i-1}$ je vektor položaja u prethodnom vremenskom koraku, $\hat{\mathbf{a}}$ je os rotacije i $\Delta t = t_i - t_{i-1}$ vremenski korak.

Model Francis 99 turbine

Model turbine iz hidroelektrane *Tokke* korišten je za Francis 99 studiju. Model je izrađen u mjerilu 1:5,1. Rotor se sastoji od 15 lopatica pune duljine i 15 skraćenih lopatica; stator se sastoji od jednog stupnja nepomičnih lopatica, dok regulacijske lopatice čine drugi stupanj. Parametre modela prikazuje tablica 1. Slika 1 prikazuje model čitave turbine, zajedno sa spiralnim te izlaznim kanalom.

Tablica 1: Parametri modela Francis 99 turbine u radnoj točki najveće iskoristivosti [14].

	$H\ [m]$	$d_{r1}\ [m]$	$d_{r2}\ [m]$	$n\ [min^{-1}]$	$Q\ [m^3/s]$	$P\ [kW]$	$Re\ [-]$
Model	12	0.63	0.349	335	0.2	22	1.8×10^6
Prototype	377	3.216	1.779	375	31	110 000	4.1×10^7

Tokom eksperimenata provedenih u laboratoriju za hidro-energiju sveučilišta NTNU u Norveškoj mjeren je tlak pomoću tlačnih senzora na više lokacija te brzina pomoću laser-doppler anemome-

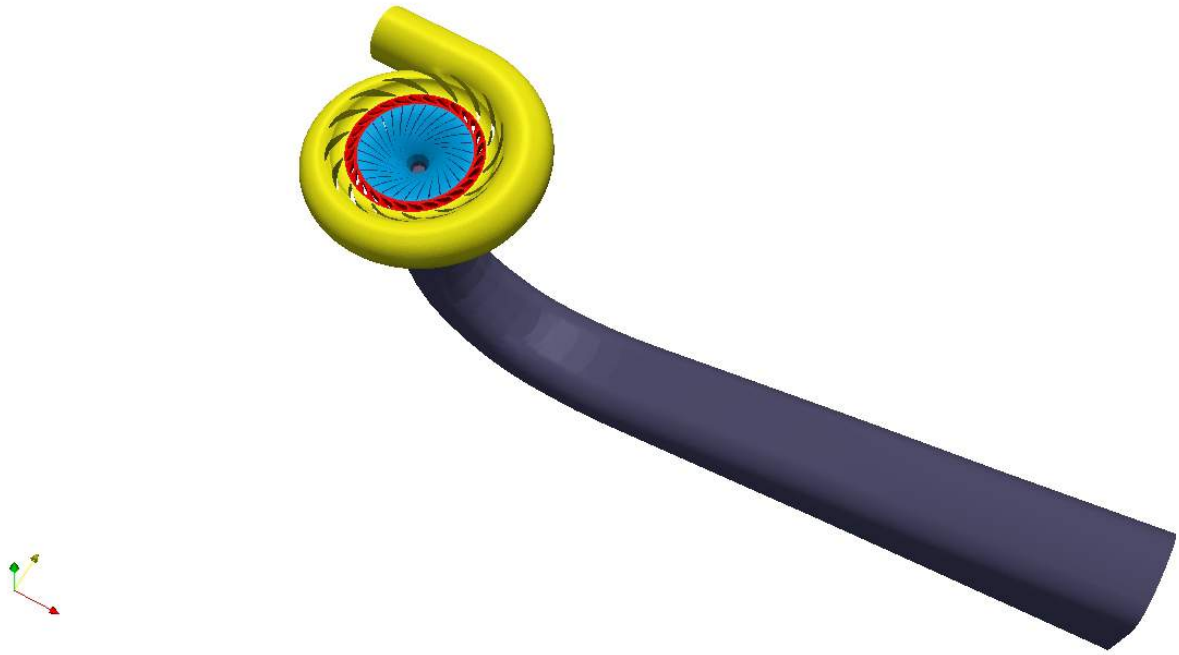

Slika 1: 3D model the Francis 99 turbine.

tra. Mjerne lokacije prikazuje slika 2. Radi usporedbe i validacije numeričkog modela, izračunate vrijednosti uspoređuju se na istim mjestima kao u eksperimentu.

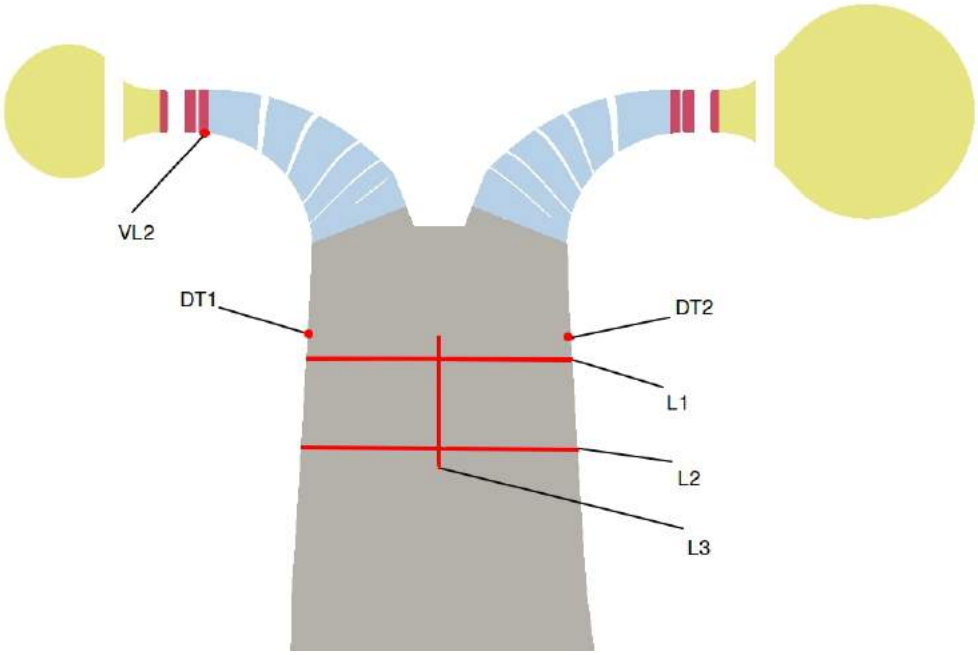

Slika 2: Lokacije eksperimentalnih mjerenja tlaka i brzine strujanja.

Računalna domena

Dvije su geometrijske domene korištene u ovom radu s ciljem smanjenja potrebnih računalnih resursa.

1. *"Model jednog strujnog kanala"*: geometrijski umanjen model koji se sastoji od jedne rotorske lopatice pune duljine te jedne polovične lopatice. Statorski dio modeliran je dvama regulacijskim lopaticama. Na osnosimetričnim granicama postavljen je periodički rubni uvjet. (Slika 3b).

2. *"Cijela geometrija rotora"*: Rotor, izlazni kanal i statorski dio s regulacijskim lopaticama prikazani su u cijelosti (Slika 3a).

(a) (b)

Slika 3: Proračunske domene (a) "Cijela geometrija rotora" (b) "Jedan strujni kanal".

Mreža kontrolnih volumena

Blok strukturirana heksaedarska proračunska mreža izrađena je ručno upotrebom alata Pointwise®. Kako bi se omogućila pravilna upotreba zidnih funkcija visina prvog reda kontrolnih volumena uz nepropusnu stijenku postavljen je tako da $y^+ > 30$. Tablica 2 prikazuje brojnost kontrolnih volumena (ćelija) u pojedinoj mreži dok tablica 3 prikazuje vrijednosti y^+ parametra na površinama statora i rotora. Detalji proračunske mreže prikazani su na slici 4.

Tablica 2: Broj kontrolnih volumena za pojedinu računalnu domenu.

	Model jednog strujnog kanala	Cijela geometrija rotora
Domain part	Broj ćelija	
Stator (regulacijske lopatice)	126 070	1 764 980
Rotor	273 560	4 047 225
Izlazni kanal	88 711	430 474
Total	488 341	6 242 679

Tablica 3: Vrijednosti y^+ parametra na zidovima domene, izračunatog $k-\varepsilon$ modelom turbulencije, u nazivnoj radnoj točki.

	Prosjek	Minimum	Maksimum
Regulacijske lopatice	39.41	14.62	88.6
Rotorske lopatice	34.59	8.79	76.39
Glavina rotora	84.27	15.9	200.3
Pokrov rotora	70.83	19.47	136.54
Ostale strujne površine statora	130.69	25.49	357
Stijenke izlaznog kanala	81.66	45.7	161.1

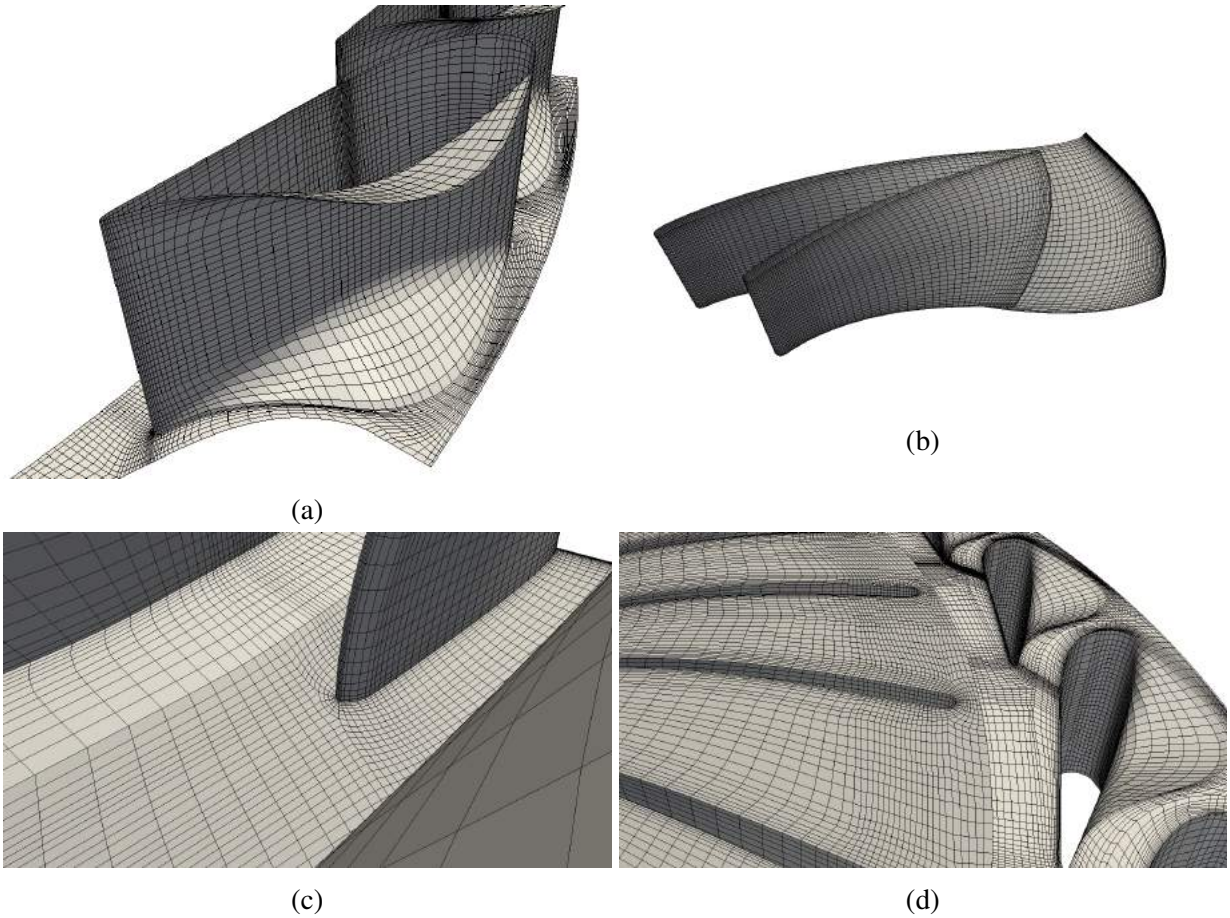

(a) (b) (c) (d)

Slika 4: Detalji mreže kontrolnih volumena.

3. Rezultati

Simulacija stacionarne radne točke

Simulacija u nazivnoj radnoj točki provedena je modelom pomičnog koordinatnog sustava i modelom rotirajuće rotorske mreže. Reducirana računalna domena (domena jednog strujnog kanala) te cjelovita geometrijska domena su korištene i međusobno uspoređene. Uspoređeni su "standardni" $k-\varepsilon$ te $k-\omega$ *SST* modeli turbulencije. Ovim simulacijama provjerene su pretpostavke korištenih modela te potvrđena njihova valjanost.

Kod simulacija nazivne radne točke na ulazu u domenu zadana je brzina strujanja, dok je za tlak zadan nulti gradijent. Na izlaznoj površini zadana je vrijednost tlaka od 0 $[m^2/s^2]$. Zadane su i vrijednosti turbulentnih veličina k i ε odnosno ω, ovisno o korištenom modelu turbulencije. Izračunate su kao funkcija poznate brzine na ulazu i uz pretpostavku intenziteta turbulencije od $I = 7,24\%$. Broj okretaja rotora je konstantan, 333 min^{-1}.

Rezultati integralnih vrijednosti prikazani su u tablici 4. Kratica MRF odnosi se na rotirajući koordinatni sustav (engl. Multiple reference frames). Visina tlaka H definirana je kao $H = \frac{\Delta p_0}{\rho g}$.

Tablica 4: Rezultati snage, iskoristivosti i visine tlaka u radnoj točki turbine s najvišom iskoristivosti.

Model	$P\ [W]$	$\Delta p_0 =$ Jed. (14) $H\ [m]$	$\eta\ [\%]$	$\Delta p_0 =$ Jed. (13) $H\ [m]$	$\eta\ [\%]$
Experiment	21 617	11.94	92.39	-	-
Jedan strujni kanal, MRF, $k-\varepsilon$	22 109	12.41	91.12	11.76	96.28
Jedan strujni kanal, MRF, $k-\omega$	21 847	12.242	91.33	11.52	96.55
Cijeli rotor, MRF, $k-\varepsilon$	22 302	12.54	91.0	11.90	95.92
Cijeli rotor, MRF, $k-\omega$	22 007	12.36	91.1	11.72	96.101
Jedan strujni kanal, rotirajuća mreža, $k-\varepsilon$	23 196	13.84	85.8	13.18	90.07

U numeričkoj simulaciji gravitacijske sile nisu uključene u jednadžbe modela. Razlika totalnog tlaka $\Delta p = p_{0,i} - p_{0,o}$ između ulaza u turbinu i izlaza definirana je kao

$$\Delta p_0 = \Delta p + \frac{1}{2}\rho\left(u_i^2 + u_o^2\right) \tag{13}$$

gdje je $\Delta p = p_i - p_o$ razlika statičkog tlaka, u_i brzina na ulazu, a u_o brzina na izlaznoj površini. U eksperimentalnim podacima preuzetim od organizatora Francis 99 radionice, razlika visine uračunata je kod definiranja visine tlaka, odnosno iskoristivosti (Jed. 14).

$$\Delta p_0 = \Delta p + 0.5\rho\left(u_i^2 + u_o^2\right) + \rho g \Delta z \tag{14}$$

gdje je $\Delta z = z_i - z_o$ visinska razlika između ulazne i izlazne površine. U tablici 4 uspoređuju se rezultati simulacija prije i nakon korekcije za razliku visine.

Dijagram na slici 5 prikazuje rezultate simulacija uspoređene s eksperimentom. Na slici 6 prikazan je tlak (manometarski) u strujnom kanalu regulacijskih lopatica i rotora. Polje brzine na mjestu interakcije rotora i statora prikazano je na slici 7. Usporedba brzine u izlaznom kanalu s rezultatima LDA mjerenja pokazuje da je u numeričkim simulacijama prenaglašeno vrtloženje strujanja oko osi kanala. Ovaj rezultat je u skladu sa sličnim simulacijama provedenim RANS modelom (2) i objavljenim na prvoj Francis 99 konferenciji [14].

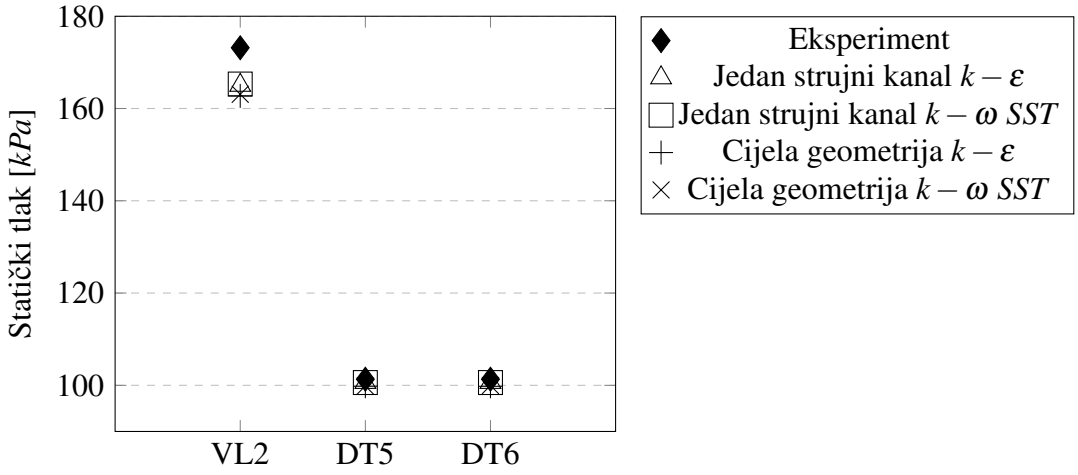

Slika 5: Usporedba apsolutnog tlaka s mjerenjima.

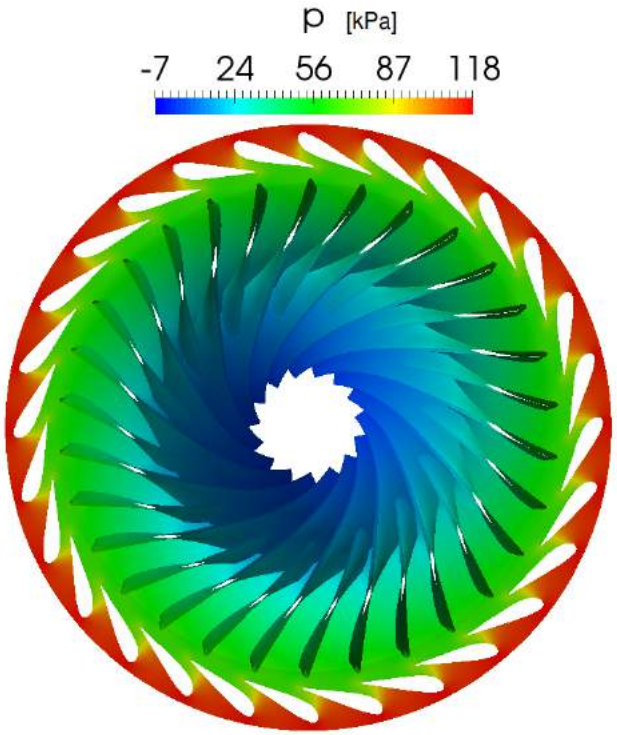

Slika 6: Pretlak p $[kPa]$ u strujnim kanalima regulacijskih lopatica i rotora (Stacionarno, MRF, $k-\varepsilon$).

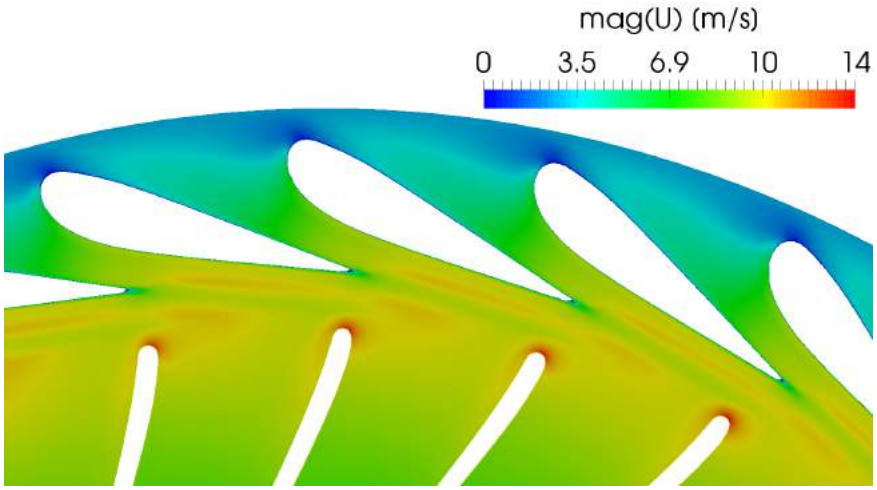

Slika 7: Euklidova norma vektora brzine $\|\mathbf{u}\|$ u strujnom kanalu regulacijskih lopatica turbine i na ulazu u rotor.

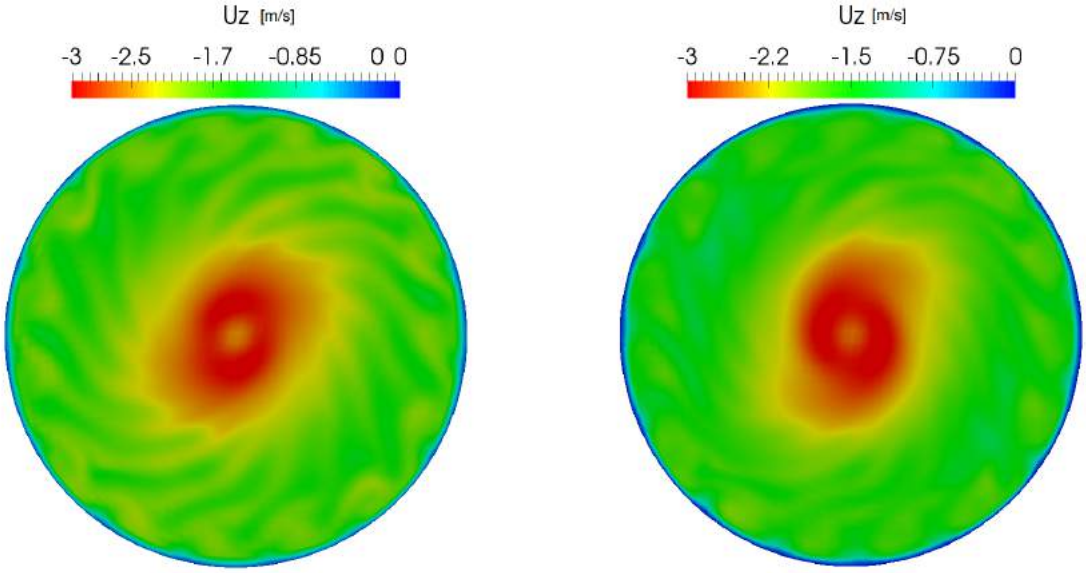

Slika 8: Aksijalna komponenta brzine U_z u izlaznom kanalu, na mjestima LDA mjerenja.

Simulacija promjene opterećenja

Simulacija promjene radne točke s najveće iskoristivosti (nazivne točke) na smanjeni pogon provedena je modelom pomičnog koordinatnog sustava i uz rješavanje jednadžbi gibanja geometrijske mreže za zakretanje regulacijskih lopatica. Pomična mreža korištena je sve dok to ne onemogući postupna degradacija mreže. U tom trenutku, na istoj poziciji lopatica, učitava s slijedeća ručno izrađena mreža.

Uspoređena su dva načina zadavanja rubnih uvjeta na ulazu u domenu:

- zadana visina tlaka H (totalni tlak),
- zadan promjenjivi protok Q (brzina fluida).

U obje simulacije korištena je reducirana domena s jednim strujnim kanalom i "standardni" $k-\varepsilon$ model turbulencije. Broj okretaja rotora je konstantan, 333 min^{-1}. Zakretanje regulacijskih lopatica zadano je kao konstantna kutna brzina od $1.19°/s$.

Kod zadavanja protoka korišten je vremenski profil $Q(t)$ iz eksperimentalnih podataka, iz kojeg su izračunate potrebne brzine, dok je za tlak zadan nulti gradijent. Na izlaznoj površini zadana je vrijednost tlaka od 0 $[m^2/s^2]$. Turbulentnih veličina k i ε izračunate su kao funkcija poznate brzine na ulazu i uz pretpostavku intenziteta turbulencije od $I = 7,24\%$.

U simulaciji sa zadanim totalnim tlakom (izračunatim prema uvjetima koji su vladali na početku eksperimenta) određen je na ulazu smjer vektora brzine dok su vrijednosti izračunate iz pada tlaka u svakom vremenskom koraku. Na izlaznoj površini zadana je vrijednost tlaka od 0 $[m^2/s^2]$. Turbulentne veličine k i ε određene su posredno preko intenziteta turbulencije od $I = 7,24\%$.

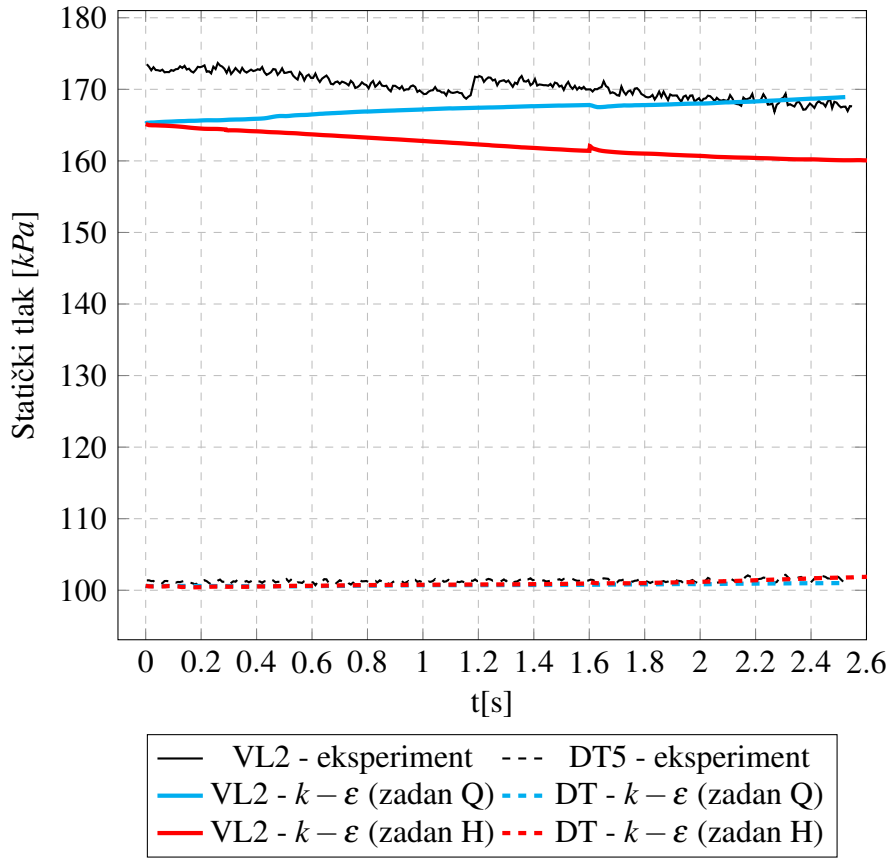

Slika 9: Usporedba statičkog tlaka na lokacijama senzora u scenariju smanjenja opterećenja turbine.

Dijagram promjene tlaka prilikom zatvaranja statorskih lopatica (Slika 9) pokazuje dobro poklapanje s eksperimentom za slučaj zadanog totalnog tlaka na ulazu. Simulacija sa zadanom brzinom na ulazu ne pokazuje podudarnost s mjerenjima. Ni trend nije realističan što dovodi do zaključka da takva postavka proračuna kvalitativno ne odgovara stvarnom slučaju. Uzrok tome je u smanjenoj računalnoj domeni koja počinje preblizu statorskim lopaticama, onemogućavajući pri tom propagaciju tlaka uzvodno.

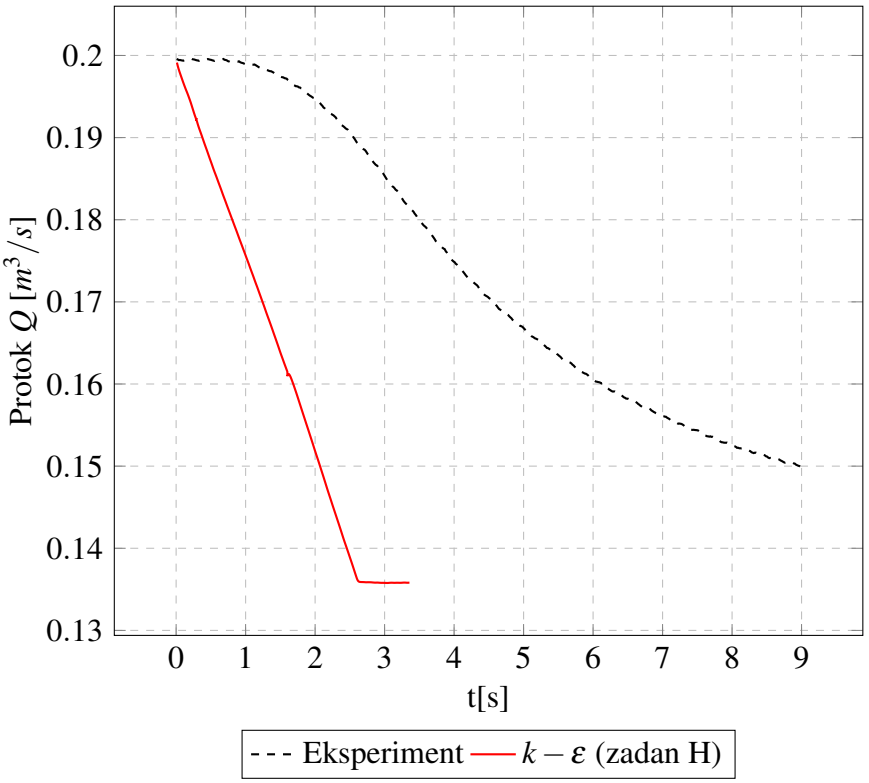

Slika 10: Vremenska promjena protoka prilikom smanjenja opterećenja.

Prilikom simulacije sa zadanim totalnim tlakom na ulazu protok kroz turbinu dio je rezultata. Dijagram na slici 10 prikazuje izračunatu vremensku promjenu protoka za slučaj smanjenja opterećenja. Vidljivo je da se u simulaciji promjena protoka ostvaruje znatno brže nego na eksperimentalnom modelu, iako je konačan rezultat na tragu rezultata mjerenja. Može se pretpostaviti da je razlog tomu smanjena geometrijska domena na kojoj je proveden proračun i da je smanjenjem domene bitno promijenjena inercija, odnosno vremenski odziv sustava. Isto tako, profil protoka je linearan u simulacijama za razliku od eksperimentalnoga što bi moglo biti posljedica zanemarivanja nekih gubitaka u spiralnom i izlaznom kanalu. Simulacije na cjelokupnoj geometrijskoj domeni turbine potrebne su za provjeru i usporedbu rezultata.

Rezultati snage i iskoristivosti na slici 11 u skladu su s predstavljenim rezultatima tlaka i protoka. Uz konstantnu brzinu vrtnje i linearni pad protoka i snaga opada linearno.

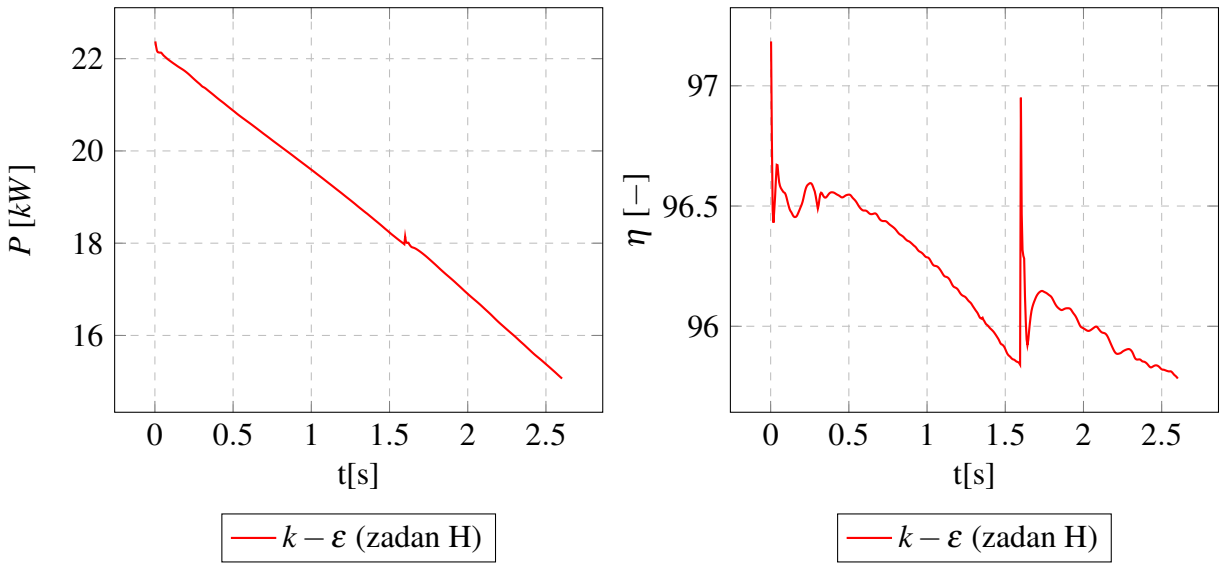

(a) Snaga [W] (b) Iskoristivost (bez utjecaja visine (Jednadžba 13)

Slika 11: Parametri turbine prilikom smanjenja opterećenja.

4. Zaključak

Provedene simulacije nazivne radne točke pokazale su zadovoljavajuće rezultate u usporedbi s rezultatima mjerenja. To vrijedi za stacionarne simulacije, kako na reduciranoj tako i cjelovitoj geometriji rotora. Veće odstupanje primjećuje se kod tranzijentne simulacije s rotirajućom mrežom i jednim strujnim kanalom. Usporedba profila brzine u izlaznom kanalu pokazuje prenaglašeno vrtloženje u numeričkim rezultatima. Vjerojatan uzrok čega su modeli turbulencije s dvije jednadžbe ($k-\varepsilon$, $k-\omega$ *SST*) i njihova jednostavnost. Unatoč tome rezultati integralnih veličina turbine su zadovoljavajuće točni.

Koncept simulacije promjene režima rada zakretanjem lopatica statora pomoću pomične mreže validiran je u ovom radu. Kod zadane visine tlaka na ulazu rezultati tlaka se u zadovoljavajućoj poklapaju s mjerenjima. Ubuduće bi se ovaj pristup mogao implementirati zajedno s rotacijom rotora kako bi se u isto vrijeme mogle izračunati i pulzacije tlaka zbog prolaska kroz vrtložni trag statorskih lopatica. Simulacije pokazuju i dobar potencijal za izračunavanje promjene protoka, kao posljedice pomicanja mreže (povećanja otpora strujanju), međutim dodatna istraživanja, ponajprije na cjelokupnoj geometrijskoj domeni su potrebna za potvrdu ovog rezultata.

Kombiniranjem pristupa s pomičnom mrežom, predstavljenog u ovom radu, s metodama rješavanja naprezanja u komponentama turbine, kao i predikciji brzine vrtnje rotora iz izračunatih sila fluida napravio bi se korak prema realističnim simulacijama prijelaznih pojava kod hidrauličkih turbina.

1 Introduction

1.1 Background and Motivation

Changes in European electricity markets over the past decade have brought a new reality for hydraulic power plants. Aiming to reduce both the carbon footprint and dependency on imported fossil fuels, many countries, primarily in the European Union, implemented the feed-in tariff systems to encourage investment in new and renewable electricity supply. A period of steady increase of such energy sources followed, with a predominance of wind power, which brought a remarkable change in both technical and economical sense. In these new market conditions, the importance of hydro-power plants as providers of both energy storage and grid control capability became essential. Hydro-power plants are nowadays expected to deliver regulating power and participate in ancillary services for the electric grid. This has resulted in frequent load variations, faster response time, emergency shut-downs and restarts, total load rejection events and overall off-design operation at prolonged time. The expected flexibility of turbine control curves reduced time spent at the nominal point, while standby operation, when plants can run for hours at very low flow rates, far away from design point, has become more common. Most of the hydroturbines, especially those of the Francis type were not designed with unsteady operation in mind, which refers to both efficiency and reliability of the machines. In the operating range of a hydraulic turbine, a number of dynamic flow phenomena can be encountered, such as rotor-stator interaction, draft tube instabilities and vortex shedding, etc. All of which can contribute to higher dynamic loads and stresses of turbine elements. Frequent load variation creates unsteady pressure loads on the runner blades, resulting in cyclic stresses and fatigue development. These effects shorten the runner life, increase cost of plant operation, and loss of power generation. Turbine startup and shutdown cycles cannot be avoided, but runner life may be improved by minimizing the unfavorable pressure loading on the blades during transients through strategic movement of guide vanes [1].

Computational fluid dynamics has been an essential tool in turbomachinery design and analysis over the past few decades and further steps in tackling mentioned challenges would be difficult without detailed analysis of flow phenomena. While hydro-power is expected to remain essential component of the electricity systems around Europe, effectively being the only large scale energy storage solution up to date, a number of different issues need to be addressed. Greater flexibility being the first priority, but at the same time, there is a tendency to reduce the blade thickness to achieve high efficiency and limit material costs. In order to increase the availability of power generation there is a need to precisely evaluate the state of fatigue stress which would enable the move from systematic to conditional maintenance leading to significant reduction of downtime.

1.2 The Francis 99 Workshop

The Francis-99 is a series of three workshops organized by the Norwegian University of Science and Technology (NTNU) and Lulea University of Technology (LTU). Workshops offer access to comprehensive design documentation and CAD data, as well as experimental data from the scale model experiments of *Tokke* high head Francis turbine. Experiments were conducted at the Water-power Laboratory at NTNU in Trondheim, Norway.

Researchers can use these data and perform numerical studies by applying different tools and techniques. The workshop thus provides means to evaluate and improve numerical methods used by both industry and universities. The focus of the first workshop was on steady turbine operation at both the best efficiency point and off-design conditions. The second workshop aims to determine the state of the art in simulation capabilities of transient operating conditions, while the third workshop is planed to add further challenge by aiming at coupled fluid-structure interaction simulations.

1.3 Literature Overview

OpenFOAM (Field Operation and Manipulation) is an open-source object-oriented library for computational continuum mechanics with an emphasis on computational fluid dynamics (CFD), written in C++ programming language [2]. Its capabilities for physical modeling, the unstructured polyhedral mesh support, complex geometry handling, robust discretization, etc. are making it a well known option for CFD calculations in both academia and industry, rivaling many of the commercial CFD codes [3].

Turbomachinery simulations are considered a significant challenge given the geometrical complexities of multi-bladed and multi-staged machines, as well as the physical complexities of unsteady rotating turbulent flows. A set of turbomachinery tools for OpenFOAM have been developed over the years to enable tackling such problems. The list of which includes: a multiple reference frames (MRF) modeling of rotating zones, general grid interface (GGI) and mixing plane for coupling interfaces between non-matching grids or distinct rotating mesh zones, specialized boundary conditions, etc. [4], [5]. Implementation of OpenFOAM and its appropriate tools for complex hydro-power turbomachinery applications has been validated by Nilsson [6], Petit [7] and Page, Beaudoin and Giroux [8]. A number of authors contributing to the first Francis 99 workshop used OpenFOAM in their work as well.

A polyhedral mesh motion for finite volume simulations was created and implemented in OpenFOAM by Tuković [9], [10] and Jasak and Tuković [11]. The same is used in present work for blade rotation modeling during turbine transient regime. A method for prediction of hydroturbine characteristics during transient operating regimes by implementing mesh motion for blade position adjustment was applied and validated on an industrial scale case by Kolšek et al. [12].

Experimental and numerical analyses of Tokke turbine model are presented in Trivedi et al. [13]. The study was conducted prior to Francis 99 workshops, providing it with experimental data and a reference point for numerical results. During the first workshop held in 2014, results of steady operating condition simulations were presented. Great majority of submitted works showed similar results to [13], good prediction of hydraulic efficiency at best operating condition and slightly higher load, while deviating from experimental results $10 - 15\%$ at reduced load. Researchers who modeled labyrinth seal losses at part load either by algebraic functions or explicit CFD modeling achieved good agreement with experimental values even at the part load operating point [14].

Different approaches to computational domain modeling were taken by authors. While great majority solved for the entire turbine geometry (spiral casing, guide vanes, runner, draft tube) a single blade passage approach on a Francis 99 turbine model has been validated by Stoessel and Nilsson [15], Mössinger et al. [16], Wallimann and Neubauer [17], Nicolle and Cupillard [18] and Buron et al. [19]. Amstutz et al. [20] demonstrated an approach in which a single blade passage of runner was modeled, while the rest of the turbine parts were represented in full.

1.4 Thesis Goal and Purpose

The aim of present work is to implement mesh motion capabilities and turbomachinery tools of OpenFOAM community driven fork `foam-extend` for prediction of transient operating regime and validate the presented approach against Tokke model experimental values. A new computational grid was created for this purpose to allow strict control over computational resource requirements and perfect mesh quality to suitable level. This thesis presents an attempt to create a minimum working example of a turbine load variation simulation for practical engineering use, using dynamic mesh and well established Reynolds-averaged Navier Stokes (RANS) modeling.

2 Mathematical Model of Incompressible Flow

Flows in hydraulic turbomachinery can be described as incompressible turbulent flows of viscous Newtonian fluid. In this chapter, governing equations and turbulence modeling used in the present work will be described. At the end, definitions of commonly used integral values in hydraulic turbomachinery analysis will be presented.

2.1 Governing Equations

2.1.1 Continuity and Momentum Equations

Equations describing incompressible flow are derived from basic physical laws of conservation:

1. Law of conservation of mass,
2. Law of conservation of momentum,
3. Law of conservation of energy.

Conservation of mass is described by the continuity equation:

$$\frac{\partial \rho}{\partial t} + \nabla \bullet (\rho \mathbf{u}) = 0 \tag{1}$$

where $\mathbf{u}$ is the velocity vector and ρ is the fluid density. With incompressibility taken into account, the density becomes invariant in space and time, which leads to the continuity equation of incompressible fluid:

$$\nabla \bullet \mathbf{u} = 0 \, . \tag{2}$$

Conservation of linear momentum stated by the Newton's Second Law is described by Navier-Stokes equations, which after taking the incompressibility into account become the following expression:

$$\frac{\partial \mathbf{u}}{\partial t} + \nabla \bullet (\mathbf{u}\mathbf{u}) - \nabla \bullet (\nu \nabla \mathbf{u}) = -\nabla p \tag{3}$$

where ν is the kinematic viscosity and p is the kinematic pressure.

The first term on the left hand side of momentum equation (Eq.3) is a temporal derivative while the second one is a convective term. These two terms are called inertial terms. The third term on the left hand side describes the momentum diffusion due to viscosity effects. On the right hand side there is a pressure gradient term. Diffusion and pressure gradient terms represent the divergence of the stress tensor.

2.1.2 Scalar Transport Equation

Generalizing the governing equations for fluid flow demonstrated in (2.1.1), a scalar transport equation can be written as

$$\frac{\partial \Phi}{\partial t} + \nabla\bullet(\mathbf{u}\Phi) - \nabla\bullet(\Gamma\nabla\Phi) = S_\Phi \tag{4}$$

where Φ is a passive scalar transported by two distinct modes:

- convection, governed by velocity field $\mathbf{u}$
- diffusion, governed by a gradient of a scalar field $\nabla\phi$ and a diffusion coefficient Γ.

In Equation (4) S_Φ represents a source or sink term of quantity Φ, consisting of all non-transport effects, such as local volume production or destruction of Φ. The temporal derivative term $\left(\frac{\partial \Phi}{\partial t}\right)$ represents the change of Φ in the local volume.

Both continuity equation (Eq.2) and momentum equation (Eq. 3) can be viewed as a special case of scalar transport equation. Continuity equation (Eq.1) is derived from (4) by substituting Φ with density ρ, and $S_\Phi = 0$. By substituting Φ with three vector components of linear momentum $\rho\mathbf{u}$, and accounting for pressure gradient $S_\Phi = \nabla p$ Navier-Stokes eq. are derived (Eq.3).In Navier-Stokes equations velocity can be viewed as both the property transported by convection and the transporting quantity itself. Linear momentum is a vector, therefore conservation of linear momentum can be divided into three scalar differential equations, each for one spatial component of velocity vector.

2.2 Turbulence Modeling

Turbulence can be described as a state of continuous instability in the flow. It is characterized by irregularity in the flow variables with increased momentum diffusivity and energy dissipation. Turbulent flows are always three-dimensional and time dependent, even if the boundary conditions of the flow do not change in time. With flows in hydraulic turbomachinery regularly being turbulent, a need for turbulence modeling in current work arises.

2.2.1 Reynolds Averaged Navier-Stokes equations

Turbulence modeling uses the fact that it is still possible to separate the fluctuations from the mean flow quantities in most turbulent flows. Using the Reynolds averaging technique, instantaneous variables are simply decomposed into time-averaged mean value $\overline{\Phi}$ and the fluctuating component Φ' as presented here for velocity and pressure:

$$\begin{aligned} \mathbf{u} &= \overline{\mathbf{u}} + \mathbf{u}' \\ p &= \overline{p} + p' \ . \end{aligned} \tag{5}$$

By separating the local value of the variable into the mean and the fluctuation around the mean, it is possible to derive the equations for the mean properties only. The result is a set of Unsteady Reynolds Averaged Navier-Stokes (URANS) equations:

$$\nabla \bullet \overline{\mathbf{u}} = 0 \tag{6}$$

$$\frac{\partial \overline{\mathbf{u}}}{\partial t} + \nabla \bullet (\overline{\mathbf{u}}\ \overline{\mathbf{u}}) = \nabla \bullet (\nu \nabla \overline{\mathbf{u}}) - \nabla p + \nabla \bullet (-\overline{\mathbf{u}'\mathbf{u}'}) \tag{7}$$

Unsteady stands for the transient term which is solved for in the equation (7), unlike steady RANS equations which solve for quasi-steady state by approximating $\frac{\partial \overline{\mathbf{u}}}{\partial t} = 0$. A new term, $\overline{\mathbf{u}'\mathbf{u}'}$, emerged in Eq. (7) which consists of solely fluctuating part of velocity (Eq. 5). This term is called Reynolds stress tensor. It is a symmetric, second order tensor value and it's divergence: $\nabla \bullet (-\rho \overline{\mathbf{u}'\mathbf{u}'})$, represents momentum diffusion due to turbulence. With addition of Reynolds stress tensor, six new unknowns are introduced into URANS equations (Eq. 7). In order to close the system of equations, further modeling is required.

The goal of turbulence modeling is to approximate the Reynolds stress tensor in terms of known variables. An approach is used in which the relationship between mean velocity gradient and values of Reynolds stresses is prescribed, namely the Boussinesq hypothesis, which approximates a linear dependence between the two:

$$\overline{\mathbf{u}'\mathbf{u}'} = \nu_t \left[\nabla \mathbf{u} + (\nabla \mathbf{u})^{\mathrm{T}} \right] + \frac{2}{3} k \mathbf{I} \tag{8}$$

where ν_t is the turbulent viscosity, $\mathbf{I}$ is the identity tensor, and

$$k = \frac{1}{2} \overline{\mathbf{u}' \bullet \mathbf{u}'} \tag{9}$$

is the defined as turbulence kinetic energy.

With such simplification, instead of six components of Reynolds stress tensor, only one unknown needs to be modeled, the turbulent viscosity ν_t. The final form of incompressible unsteady Navier-Stokes equations implemented in Computational Fluid Dynamics, according to Ferzinger and Perić [21] is presetnted by Equation (10).

$$\frac{\partial \overline{\mathbf{u}}}{\partial t} + \nabla \bullet (\overline{\mathbf{u}}\ \overline{\mathbf{u}}) - \nabla \bullet (\nu_{eff} \nabla \overline{\mathbf{u}}) - \nabla p \tag{10}$$

where ν_{eff} is the effective viscosity, which is equal to the sum of the molecular and turbulent (eddy) viscosity:

$$\nu_{eff} = \nu + \nu_t\ . \tag{11}$$

Widely popular approach in numerical modeling of turbulent viscosity ν_t, and the one used in present work is the "two-equation" turbulence modeling, in which turbulent kinetic energy k $[m^2/s^2]$ and its dissipation rate ε $[m^2/s^3]$ are solved by their own respective transport equations. Computational cost and accuracy are two defining characteristics of turbulence models, the $k-\varepsilon$ family of models and the more recent $k-\omega$ *SST* are predominantly used in Computational Fluid Dynamics for being a good balance between the two.

Turbulence models implemented in `OpenFOAM`, precisely the `foam-extend` fork, used in present work were `kEpsilon` and `kOmegaSST`.

2.2.2 The $k-\varepsilon$ Turbulence Model

One of the most commonly used models is the $k-\varepsilon$ model, often named *standard* $k-\varepsilon$, implemented according to Jones and Launder [22]. Model equations for incompressible flow will be presented here.

Turbulent viscosity is represented as a function of turbulent kinetic energy and its dissipation rate:

$$\nu_t = C_\mu \frac{k^2}{\varepsilon} \tag{12}$$

Governing transport equation of turbulent kinetic energy k reads:

$$\frac{\partial k}{\partial t} + \nabla\bullet(\overline{\mathbf{u}}k) - k\nabla\bullet\overline{\mathbf{u}} - \nabla\bullet(\nu_{eff}\nabla k) = G - \varepsilon \tag{13}$$

where effective turbulence viscosity ν_{eff} is defined by Equation (11) and production of k is defined as

$$G = -\overline{\mathbf{u}'\mathbf{u}'}\nabla\overline{\mathbf{u}} = \nu_t S^2 \tag{14}$$

with S being the modulus of the mean rate-of-strain tensor:

$$S = \left| \frac{1}{2}\nabla\overline{\mathbf{u}} + (\nabla\overline{\mathbf{u}})^{\mathrm{T}} \right| \tag{15}$$

Dissipation of turbulent kinetic energy is modeled by equation:

$$\frac{\partial \varepsilon}{\partial t} + \nabla\bullet(\overline{\mathbf{u}}\varepsilon) - \varepsilon\nabla\bullet\overline{\mathbf{u}} - \nabla\bullet\left[\left(\nu + \frac{\nu_t}{\alpha_\varepsilon}\right)\nabla\varepsilon\right] = C_1\frac{\varepsilon}{k}G - C_2\frac{\varepsilon^2}{k} \tag{16}$$

Model coefficients are necessary to be defined in order to determine the above system of equations. Coefficients used in simulations in present work are showed in Table 1.

Table 1: Coefficients of *Standard* $k-\varepsilon$ turbulence model.

C_μ	0.09
C_1	1.44
C_2	1.92
α_ε	0.76923

2.2.3 The $k-\omega$ *SST* turbulence model

The $k-\omega SST$ (Shear Stress Transport) turbulence model, implemented according to Menter [23] is a "two-equation" turbulence model which, apart form turbulent kinetic energy, models its dissipation as specific turbulent dissipation quantity ω. A version of the $k-\varepsilon$ model is used far from the walls and the $k-\omega$ model close to the walls, attempting to combine the best properties of both models by implementation of blending functions.
Turbulent kinetic energy equation is defined by

$$\frac{\partial k}{\partial t}+\nabla\bullet(\overline{\mathbf{u}}k)-\nabla\bullet(\nu_{k,eff}\nabla k)=min(G,C_1\beta^*k\omega)-\beta^*k\omega \tag{17}$$

where effective viscosity in k equation (Eq. 17) is defined as $\nu_{k,eff}=\alpha_k=\nu_t+\nu$.
Specific dissipation rate equation reads

$$\begin{aligned}\frac{\partial\omega}{\partial t}+\nabla\bullet(\overline{\mathbf{u}}\omega)-\omega\nabla\bullet\overline{\mathbf{u}}-\nabla\bullet(\nu_{\omega,eff}\nabla\omega)=\gamma\,min\left[S^2,\frac{c_1}{a_1}\beta^*\omega max\left(a_1\omega,\,b_1\,F2\,S\right)\right]\\ -\beta\omega^2+(1-F_1)CD_{k\omega}\end{aligned} \tag{18}$$

where effective viscosity in ω equation (Eq. 18) is defined as $\nu_{\omega,eff}=\alpha_\omega=\nu_t+\nu$, S is the the modulus of the mean rate-of-strain tensor defined in Eq. (15), and $G=\nu_tS^2$ is production of k.
Turbulent viscosity is defined as

$$\nu_t=\frac{a_1k}{max\left(a_1\omega,\,F_2S\right)} \tag{19}$$

Each of the model constants are determined by blending functions F_1 and F_2:

$$\begin{aligned}\alpha_k&=F_1(\alpha_{k_1}-\alpha_{k_2})+\alpha_{k_2}\\ \alpha_\omega&=F_1(\alpha_{\omega_1}-\alpha_{\omega_2})+\alpha_{\omega_2}\\ \beta&=F_1(\beta_1-\beta_2)+\beta_2\\ \gamma&=F_1(\gamma_1-\gamma_2)+\gamma_2\end{aligned} \tag{20}$$

Blending functions F_1 and F_2 being:

$$F_1 = tanh\left\{\left[min\left(max\left[\frac{\sqrt{k}}{\beta^*\omega y}, \frac{500\nu}{y^2\omega}\right], \frac{4\alpha_{\omega_2}k}{CD_{k\omega+}y^2}\right), 10\right]^4\right\} \tag{21}$$

$$F_2 = tanh\left\{\left[max\left(\frac{2\sqrt{k}}{\beta^*\omega y}, \frac{500\nu}{y^2\omega}\right), 100\right]^2\right\} \tag{22}$$

Positive portion of cross-diffusion term is introduced for numerical stability:

$$\begin{aligned} CD_{k\omega+} &= max(CDk\omega, 10^{-10}) \\ CD_{k\omega} &= 2\alpha\omega_2\frac{\nabla k \bullet \nabla\omega}{\omega} \end{aligned} \tag{23}$$

Model coefficients are showed in Table 2.

Table 2: Coefficients of $k-\omega$ *SST* turbulence model.

C_μ	0.09
C_1	10
α_{k_1}	0.85034
α_{k_2}	1
α_{ω_1}	0.5
α_{ω_2}	0.85616
β_1	0.075
β_2	0.0828
β^*	0.09
γ_1	0.5532
γ_2	0.4403
a_1	0.31

2.2.4 Near-wall Treatment

The behavior of turbulent flow near the no-slip boundaries, i.e. in the boundary layer is considerably different then in the outer part of the flow domain. Turbulent instabilities are dampened in the presence of the impermeable surface, hence turbulent viscosity becomes negligible.

The inner turbulent boundary layer can be approximately divided into three sublayers:

- inertial sublayer ($30 < y^+ < 300$),
- buffer layer ($5 < y^+ < 30$),

- viscous linear sublayer ($y^+ < 5$),

where y^+ is the normalized distance to the wall boundary defined by Launder and Spalding [24] as:

$$y^+ = y\frac{C_\mu^{1/4}k^{1/2}}{\nu} \tag{24}$$

Turbulent viscosity is dominant in the *inertial sublayer* molecular viscosity contribution being negligible. Mean velocity profile follows the log-law, while the rate of turbulence production and dissipation are equal. In the *viscous sublayer* on the other hand, turbulence effect are not present, molecular viscosity is dominant and velocity profile is linear. The *buffer sublayer* is a transition zone between the two, where there is a mixed influence of both viscous and turbulent viscosity.

Two approaches to near-wall modeling are possible at this point. With *Low-Re* modeling, the center of first cell is placed it the viscous sublayer ($y^+ < 5$), a procedure which demands computational grid resolution in the boundary layer to be very fine.

Another possibility is an approximation in form of *standard wall functions*, which is the one used in present work, in which first cell center is placed in the inertial sublayer ($30 < y^+ < 300$). Flow variables in the boundary layer are approximated using algebraic expressions which avoids the need to integrate the RANS model equations all the way to the wall by making use of the universal behavior of near-wall flows discussed earlier. Placing the cell center in the buffer layer should be strongly avoided.

Using this simplified model of turbulence it is possible to bridge the regions of high gradients near the wall and couple them with the high-*Re* $k-\varepsilon$ or $k-\omega$ *SST* models in the rest of the domain, substantially reducing the computational cost.

2.3 A Definition of a Vortex

In analysis of fluid flow, an often used expression for qualitative description of common flow structures is the one where a structure is called a *vortex*. However, an often ambiguous identification of vortices requires an objective and reference-frame-independent definition. One proposed solution is the Q-criterion, which defines a vortex as a spatial region where:

$$Q = \frac{1}{2}\left[|\Omega|^2 - |S|^2\right] > 0 \tag{25}$$

In the Equation (25) S is the rate-of-strain tensor:

$$S = \frac{1}{2}\left[\nabla\mathbf{u} + (\nabla\mathbf{u})^{\mathrm{T}}\right] \tag{26}$$

and

$$Q = \frac{1}{2}\left[\nabla\mathbf{u} - (\nabla\mathbf{u})^{\mathrm{T}}\right] \tag{27}$$

is the vorticity tensor. Q is positive in a region where the Euclidean norm of the vorticity tensor is grater then the one of the rate of strain.

2.4 Hydrodynamical Integral Quantities Definition

There is a number of physical properties and non-dimensional parameters used to characterize hydraulic machinery with regards to their power, efficiency etc. For engineering applications, here presented integral properties are used, meaning that they represent an average of flow variables over a certain flow section or other surface or volume [25]. The most important such surfaces are the inlet and outlet, with their areas defined as A_i and A_o respectively. The turbine head is determined by a total pressure difference between inlet and outlet surfaces of the runner:

$$H = \frac{\Delta p_0}{\rho g} \tag{28}$$

where ρ is the fluid density and g is gravitational acceleration constant. Total pressure difference $\Delta p = p_{0,i} - p_{0,o}$ is defined as

$$\Delta p_0 = \Delta p + \frac{1}{2}\rho \left(u_i^2 + u_o^2\right) \tag{29}$$

where $\Delta p = p_i - p_o$ is the static pressure difference between inlet and outlet surfaces, u_i is the velocity at the inlet surface and u_o is the velocity at the outlet surface.
In the presented Francis 99 workshop data (Section 4.1.1) height difference is accounted for in the results, meaning the total pressure difference is

$$\Delta p_0 = \Delta p + 0.5\rho \left(u_i^2 + u_o^2\right) + \rho g \Delta z \tag{30}$$

where $\Delta z = z_i - z_o$ is the distance between runner inlet and outlet surfaces in z axis direction.
Effective turbine power output is defined as

$$P = \omega T \tag{31}$$

where ω is the angular velocity of turbine runner and T is the torque exerted on the turbine shaft. Turbine efficiency is defined as

$$\eta = \frac{P}{\Delta p_0 Q} = \frac{\omega T}{\Delta p_0 Q} \tag{32}$$

where the maximum available power is defined by the total pressure difference and flow rate in the denominator [25].

3 Numerical Modeling

3.1 The General Grid Interface

The General Grid Interface (GGI), developed by Beaudoin and Jasak [5], is a coupling interface for `foam-extend` that, by using weighted interpolation joins a pair of conformal or non-conformal patches from separate mesh regions into a singe computational domain. The ability to couple the non-conformal mesh surfaces is especially welcome in dealing with often complex grids of rotor and stator regions in turbomachinery applications, for they are extremely difficult to match with a point-to-point conformal grids. A number of mesh interfaces is derived from the basic GGI. The `cyclicGgi` handles non-conformal periodic surfaces by implementing GGI interpolation together with a coordinate transformation. To simulate the topologically un-fitting patches `overlapGgi` is used. With the assumption that the uncovered part of the surfaces are rotationally symmetric, patches are expanded to create a complete mapping surface. Once a pair of expanded mapping surfaces is established, field data is interpolated and transfered to the corresponding patch [4].

3.2 Rotor-stator Interaction Modeling

Special interest is given to interactions between rotating and stationary parts in turbomachinery analysis, as they are both complex and important for efficiency and reliability. Even at steady operation, a transient pressure loading is acting on the runner blades as they pass trough wakes of the stator blades. Complex flow structures are induced as a result of rotor-stator interaction, making a way in which the interface between these two parts is resolved of key importance for the level of simulation accuracy. Two different approaches used in this work are presented, the frozen-rotor, and sliding grid approach.

3.2.1 The Frozen-rotor Approach

Both rotating and stationary parts of the machine are represented by a static computational mesh, while rotation-related influence on the flow physics is accounted for by addition of centrifugal and Coriolis force source terms in the momentum equation. In present work the *multiple reference frame* (MRF) model, implemented in `foam-extend` is used. In this model, an absolute velocity formulation is present and volumetric face flux is calculated directly based on $\boldsymbol{\omega} \times \mathbf{r}$ for each rotating coordinate system. The absolute velocity formulation does not require a transformation of the velocity vector at the interface between rotating zones [4]. Equation (33) shows

the formulation of URANS equations for rotating frames, implemented in `OpenFOAM`.

$$\frac{\partial \mathbf{u}}{\partial t} + \nabla \bullet (\mathbf{u}_r \mathbf{u}) + \omega \times \mathbf{u} = -\nabla p + \nabla \bullet (\nu \nabla \mathbf{u}) \tag{33}$$

where $\mathbf{u}$ is the absolute velocity, $\mathbf{u}_r$ is the relative velocity (the velocity viewed from the rotating frame) and ω is the angular velocity vector. Relative velocity being defined by Eq. (34).

$$\mathbf{u}_r = \mathbf{u} - \omega \times \mathbf{r} \tag{34}$$

where $\mathbf{r}$ is the position vector, whose origin is the center of rotation for a given rotating frame.

To implement the *multiple reference frame* modeling for the transient turbine operation, namely the closing of guide vanes, which is the task of present work, a custom `OpenFOAM` solver application had to be created by adding the MRF-zone sources to the standard `pimpleDyMFoam`. In the resulting application (`MRFpimpleDyMFoam`) *dynamic mesh* handling is used solely for guide vane rotation, while MRF-zones handle the constant-speed runner rotation.

3.2.2 The Sliding Grid Approach

A rotation of computational grid is carried out at each time-step in sliding grid method, changing the relative position of rotor and stator parts in a way that corresponds to the way it happens in actual rotary machines. The connectivity between rotor and stator parts of the mesh needs to be handled specifically since the notion of neighbor cells is in the very basis of finite-volume method's mathematical formulation. By rotating one part of the mesh, neighboring cells from the first instant drift further apart, as the simulation progresses. A GGI interface described in (3.1) is used to connect the corresponding mesh regions at their interfaces. Dynamic mesh capabilities of `foam-extend` ([26]) are used for this purpose in present work, precisely the `turboFvMesh` class which rotates a chosen number of mesh regions about an prescribed axis at each time step.

The sliding grid approach, utilizing the moving mesh, is the most accurate simulation technique for rotor-stator interaction dominated flows, with the drawback of being the most computationally demanding one.

3.3 Guide Vane Rotation Modeling

A moving-mesh finite volume method provides flow solution when the spatial domain changes with time. In present work, a vertex-based unstructured mesh motion solver implemented in `foam-extend` is used for this purpose. The solver rearranges mesh points at each time step to allow for gradual rotation of guide vanes which is prescribed as a boundary condition.

3.3.1 Finite Volume Method on Moving Meshes

Finite volume method is derived by integrating the governing equations of fluid flow (Section 2.1) over an arbitrary moving control volume (cell) V, enclosed by a surface S. For a tensorial property Φ of n-th rank a transport equation states:

$$\frac{\partial}{\partial t}\int_V \rho\Phi\partial V + \oint_S \rho\mathbf{n}\bullet(\mathbf{u}-\mathbf{u}_S)\Phi\partial S - \oint_S \rho\gamma_\Phi\,\mathbf{n}\bullet\nabla\Phi\;\partial S = \int_V s_\Phi\partial V \tag{35}$$

where $\mathbf{n}$ is the outward pointing unit normal vector on the boundary surface S, $\mathbf{u}$ is the fluid velocity, $\mathbf{u}_S$ is the velocity of the boundary surface, γ_Φ is the diffusion coefficient, and s_Φ is the volume source of Φ.

Volume of the cell as well as its boundaries are time-dependent variables, governed by the geometric (space) conservation law:

$$\frac{\partial}{\partial t}\int_\partial V - \oint_S \mathbf{n}\bullet\mathbf{u}_S\;\partial S = 0 \tag{36}$$

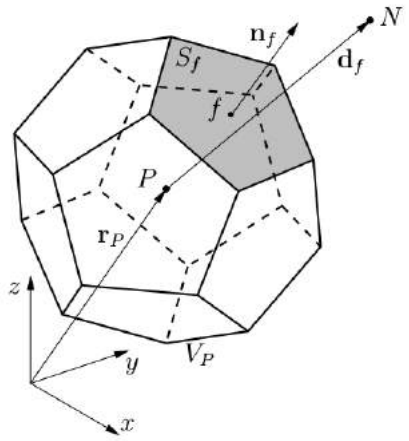

Figure 1: A control volume (cell) [9]

The unstructured finite volume method is applied to a computational domain discretized into a finite number of non-overlapping convex polyhedral cells bounded by convex polygons. The temporal dimension is discretized into a finite number of time intervals due to the parabolic nature of time derivative term. Figure 1 shows a representative finite volume (cell) of a computational domain with P being its computational point (located in its centroid) and a face f with the face area S_f and the face unit normal vector $\mathbf{n}_f$. Position vector $\mathbf{r}_P$ of the computational cell connects the centroid P with the coordinate system origin. Neighboring cell is represented in Fig. (1) by its respective centroid N and a distance vector $\mathbf{d}_f$. Finite volume discretization transforms the Equation (35) in a way that surface integrals become a sum of approximated control volume face integrals, while volume integrals are approximated to second order using mid-point rule [9], [10].

3.3.2 The Polyhedral Mesh Motion Solver

The objective of automatic mesh motion is to execute externally prescribed boundary deformation by changing positions of internal mesh points while preserving the mesh geometrical validity. In `foam-extend` a vertex-based unstructured mesh motion solver exists for this purpose. Mesh is valid if all cell volumes and volume surfaces remain convex, and if mesh non-orthogonality is kept below critical level. As finite volume method provides the solution in cell centers and motion of the points is required, while at the same time, it is extremely difficult to perform a cell to point interpolation which would keep the cells from being severely deformed, a finite element method is used for the task. In order to implement the FEM (finite element method) solution, the polyhedral mesh motion solver needs to split the polyhedral cells into multiple tetrahedrons, first by splitting their faces in triangles, then by connecting a face triangle with a cell centroid to construct a tetrahedron.
The mesh motion is governed by Laplace equation (Eq. 37).

$$\nabla_{\bullet}(\gamma \nabla \mathbf{u}) = 0 \tag{37}$$

where $\mathbf{u}$ is the mesh point velocity field and γ is the diffusion coefficient governing the mesh motion. Point positions are modified as follows from Eq. (38).

$$\mathbf{x}_{new} = \mathbf{x}_{old} + \mathbf{u}\Delta t \tag{38}$$

where x represents the point position vector in Cartesian space and Δt is the time step.

Variable mesh diffusivity γ can be prescribed with intention of mitigating the mesh degradation in certain areas over the course of the simulation. Especially sensitive to mesh distortion is the near-boundary region. By increasing the diffusivity in the region close to the boundary mesh distortion reduces locally, at the same time being increased further away form the boundary, where it is safe to presume that mesh points have more freedom to rearrange.

Several diffusion functions can be prescribed, *Distance-based methods* take into account the cell distance l to one of the user selected boundary patches while calculating the local diffusivity. There is a choice of several laws for this:

- linear, where $\gamma = \frac{1}{l}$,
- quadratic, where $\gamma = \frac{1}{l^2}$ and
- exponential, where $\gamma = \mathrm{e}^{-l}$.

Equation (37) is discretized on the tetrahedrally decomposed mesh using the Galerkin weighted residual finite element method. The solution of discretized equations is achieved using an itera-

tive linear equation solver, namely the Incomplete Cholesky Preconditioned Conjugate Gradient solver.

3.3.3 Mesh Substitution Strategy

When the automatic mesh motion is no longer possible due to the mesh quality degrading below minimum of usability, a new manually crafted mesh is substituted and simulation is continued. The field values are mapped onto a new mesh using the standard `OpenFOAM` field mapper. However, the mapper utility does not preserve conservativeness between meshes, resulting in artificial, numerically originated source that disappears with a certain number of time steps, while flow quantities converge again.

3.3.4 Motion Solver Boundary Condition

The known boundary motion is prescribed as a boundary condition for the motion equation. This may include free boundaries, symmetry planes, prescribed motion boundary, etc. To simulate the guide vane rotation from the Francis 99 load variation experiments a constant angular velocity needs to be set at the guide vane surface boundary. Using a current implementation of `foam-extend`'s boundary condition that calculates angular velocity as a time-dependent oscillatory value, a new boundary condition is derived similarly to Saraf [27], to allow a simple prescription of constant angular velocity directly by the user. Modifications had to be made in present work to allow for mesh substitution described in Section 3.3.3.

Deriving from Rodrigues' rotation formula an expression for calculating the velocity of the boundary mesh points, at the arbitrary time $t = i$ states:

$$\mathbf{u}_i = \frac{\mathbf{p}_0 - \mathbf{p}_{i-1} + \hat{\mathbf{a}}(\hat{\mathbf{a}} \bullet \mathbf{p}_0)(1 - cos\alpha_i) + (\hat{\mathbf{a}} \times \mathbf{p}_0) sin\alpha_i + \mathbf{p}_0(cos\alpha_i - 1)}{\Delta t} \tag{39}$$

where $\mathbf{p}_0$ is the point position vector at the start of the rotation, $\mathbf{p}_{i-1}$ is the point position vector at the previous time step, $\hat{\mathbf{a}}$ is the rotation axis unit vector, $\Delta t = t_i - t_{i-1}$ is the time step and α_i is the rotation angle, defined as:

$$\alpha_i = \omega \frac{\pi}{180}(t_i - t_0) \tag{40}$$

with t_0 being the rotation start time and $\omega = \frac{d\alpha}{dt}$ the angular velocity in degrees per second prescribed by user as a boundary condition. The Position vector ($\mathbf{p}$) of all points on a moving boundary are stored as a `pointField` type in `OpenFOAM`.

3.4 Custom Inlet Boundary Conditions

Inlet surface of the computational domain is located between the row of fixed stay vanes and guide vanes. The surface is of cylindrical shape and flow, being directed by the stay vanes is not normal to that surface. In order to correctly model an inlet in such conditions two new boundary condition formulations in `OpenFOAM` are introduced.

3.4.1 Prescribing Velocity on a Cylindrical Surface

A velocity vector on a cylindrical plane defined by origin in $(0,0,0)$, radius $\mathbf{r}$ and axis vector $\hat{\mathbf{a}}$ can be prescribed by the user with the normal (radial) $\|\mathbf{u}_r\|$, tangential $\|\mathbf{u}_t\|$ and axial $\|\mathbf{u}_a\|$ component magnitudes. The resulting velocity vector is calculated by `cylindricalInletVelocity` boundary condition using Equation (41).

$$\mathbf{u}_{inlet} = \|\mathbf{u}_a\|\hat{\mathbf{a}} + \|\mathbf{u}_t\|\frac{\mathbf{r}\times\hat{\mathbf{a}}}{\|\mathbf{r}\times\hat{\mathbf{a}}\|} + \|\mathbf{u}_r\|\frac{\mathbf{d}\times\hat{\mathbf{a}}}{\|\mathbf{d}\times\hat{\mathbf{a}}\|} \tag{41}$$

where vector $\mathbf{d}$ is defined as:

$$\mathbf{d} = \mathbf{r} - \hat{\mathbf{a}}(\mathbf{r}\cdot\hat{\mathbf{a}}) \tag{42}$$

3.4.2 Prescribing Velocity Direction on a Cylindrical Surface

On a same cylindrical surface described in Section (3.4.1) velocity direction can be prescribed by the user with the normal(radial), tangential and axial vector components. The resulting velocity orientation in (x,y,z) coordinates is calculated by `pressureDirectedCylindricalInletVelocity` boundary condition using Equation (43).

$$\hat{\mathbf{u}}_{inlet} = \frac{\mathbf{u}_{inlet}}{\|\mathbf{u}_{inlet}\|} \tag{43}$$

where $\mathbf{u}_{inlet}$ is defined by Eq.(41). Inlet velocity magnitude is calculated using pressure driven flow rate at each control volume.

3.5 Turbulence Inlet Boundary Conditions

Boundary conditions for turbulent flow at the inlet of a computational domain have to be calculated if the inlet velocity is known, and imposed as Dirichlet boundary conditions, i.e. by specifying the scalar value of the variable at the boundary.

The turbulence kinetic energy is calculated as

$$k = \frac{3}{2}(u\,I)^2 \tag{44}$$

where $u = \|\mathbf{u}\|$ is inlet velocity magnitude and I is the turbulence intensity defined as ratio of root mean square of the velocity fluctuating part u' and mean velocity magnitude $\overline{u}$:

$$\begin{aligned} I &= \frac{\sqrt{\overline{(u')^2}}}{\overline{u}} \\ u &= \overline{u} + u' \end{aligned} \tag{45}$$

Turbulence dissipation rate ε and specific dissipation rate ω are calculated by

$$\begin{aligned} \varepsilon &= C_\mu \frac{k^2}{\beta \nu} \\ \omega &= \frac{k}{\beta \nu} \end{aligned} \tag{46}$$

where $\beta = \nu_t/\nu$ is the ratio of turbulent and molecular viscosity.

4 Computational Model of Francis 99 turbine

4.1 Test Case Description

The model of a turbine used as a Francis 99 test case, located at *Hydropower Laboratory* at NTNU (Section 1.2), is a $1:5.1$ scaled model of the turbines operating at Tokke power plant in Norway. The runner has 30 blades, of which 15 are splitter blades of half the length and 15 full blades. In the distributor there are 28 guide vanes and 14 stay vanes. It is a high head Francis turbine with the rated head of the prototype of 377 m and power output of 110 MW, with a runner inlet diameter of 3.216 m and outlet diameter of 1.779 m. Full-length runner blades are twisted by an angle of 180 $^\circ$ looking from runner inlet to the outlet. A cut drawing of the turbine model with all the key parts is shown in Figure 2.

Table 3: Francis 99 model and prototype parameters at best efficiency point [14].

	$H\ [m]$	$d_{inlet}\ [m]$	$d_{outlet}\ [m]$	$n\ [min^{-1}]$	$Q\ [m^3/s]$	$P\ [kW]$	$Re\ [-]$
Model	12	0.63	0.349	335	0.2	22	1.8×10^6
Prototype	377	3.216	1.779	375	31	110 000	4.1×10^7

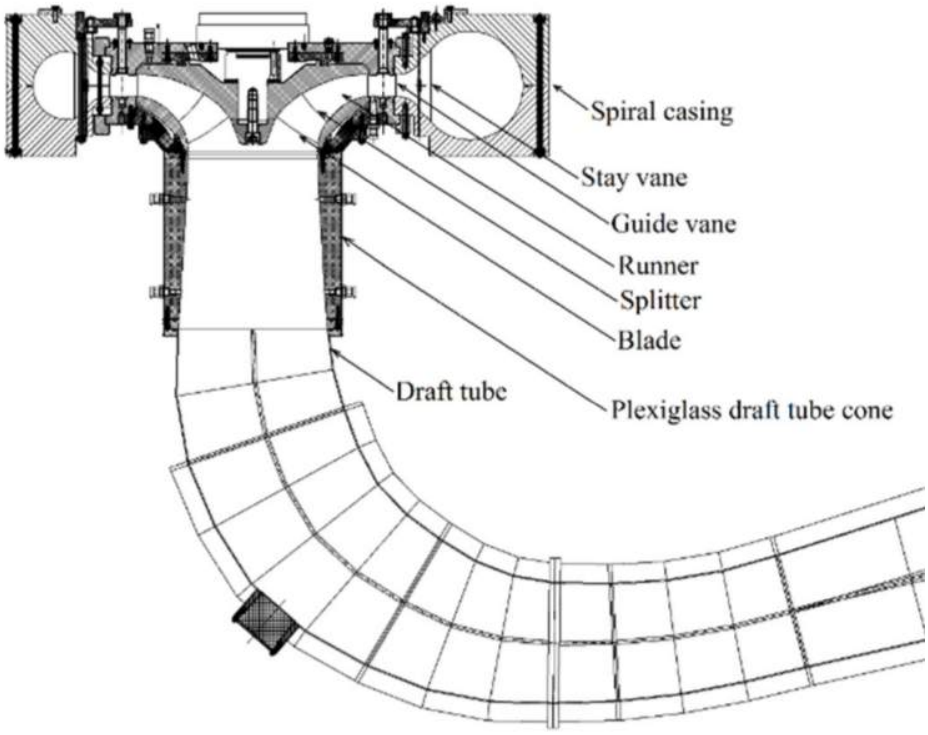

Figure 2: Cut view of the Francis 99 turbine model [14].

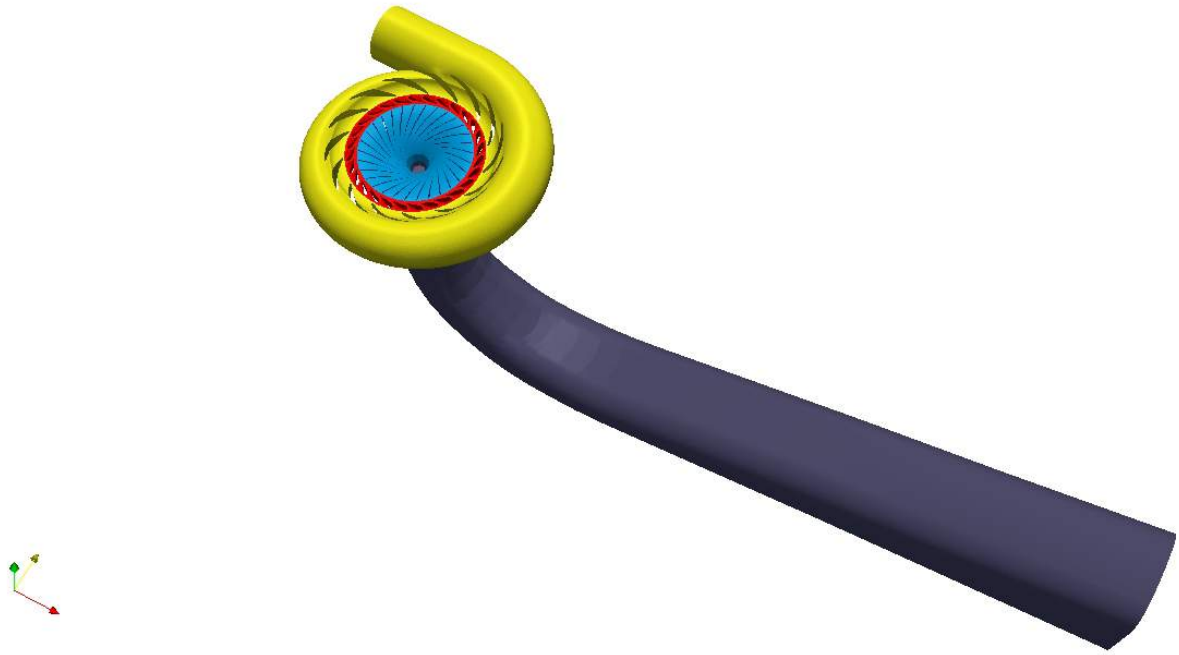

Figure 3: 3D model the Francis 99 turbine.

Pressure and velocity data at an array of locations were acquired during the experiments on the Francis 99 turbine model (Figure 4). The measurement data and test description is available at F99 web page [28], as well as in Trivedi et al. [13],[14]. An estimation of random uncertainty was carried out for measured values.

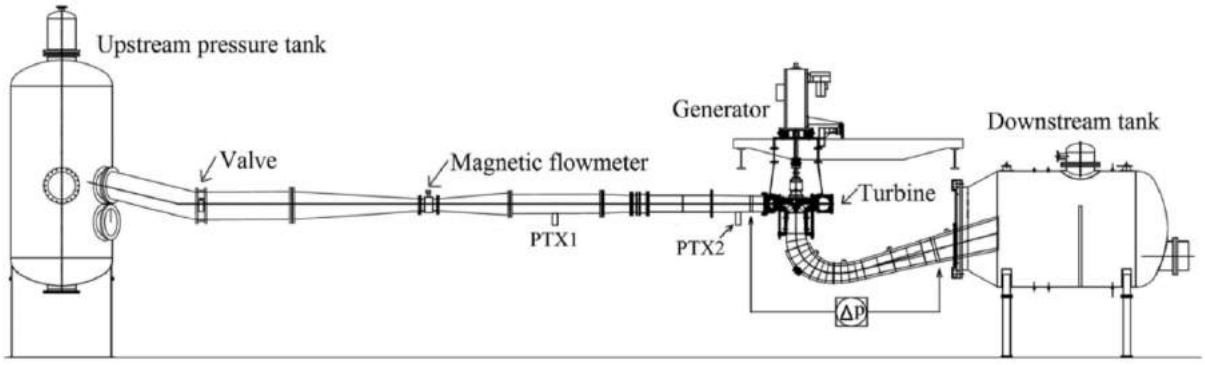

Figure 4: Francis 99 model test rig [13].

For the sake of comparison and validation of numerical results, data acquisition during post-processing was done at the corresponding locations. Naming of the sensor locations and the coordinates of points were given according to Francis 99 official material [28]. The reference coordinate system is shown in Figure 5.

For the pressure measurements three sensors were mounted, VL2 in the vaneless space be-

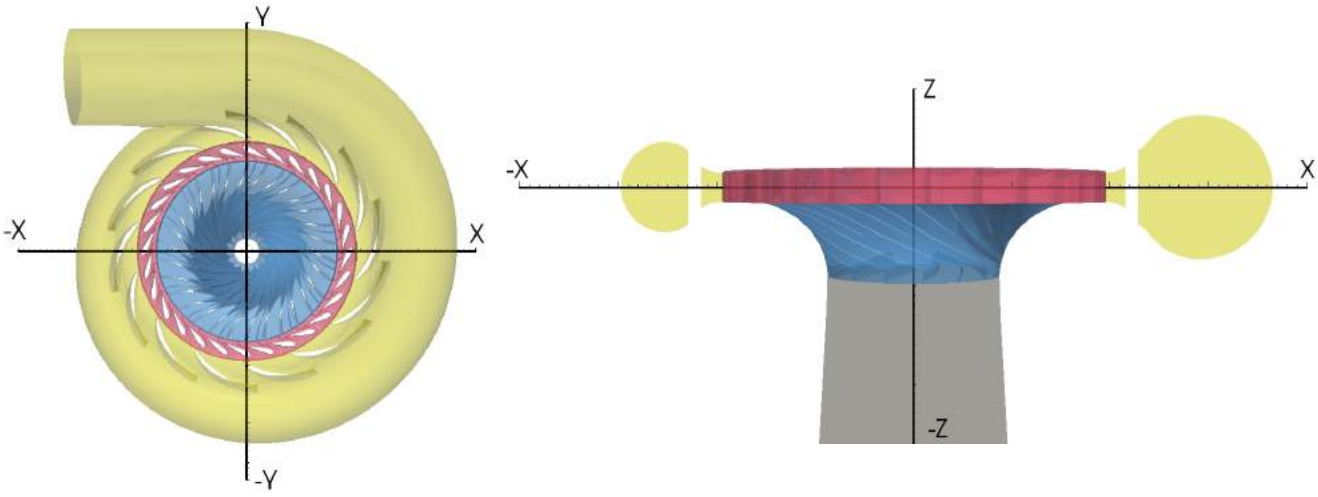

Figure 5: Reference coordinate system.

tween guide vanes and runner, DT5 and DT6 in the draft tube. Coordinates are provided in Table 4. Laser Doppler Anemometry (LDA) measurements of velocity profiles was done along three lines in the draft tube. Table 5 shows the coordinates of the line start- and endpoints. Both LDA lines and pressure sensors are displayed in Figure 6.

	$x\ [mm]$	$y\ [mm]$	$z\ [mm]$
VL2	-320	62.2	-29.4
DT5	-149.1	-100.6	-305.8
DT6	149.1	100.6	-305.8

Table 4: Pressure measurement locations.

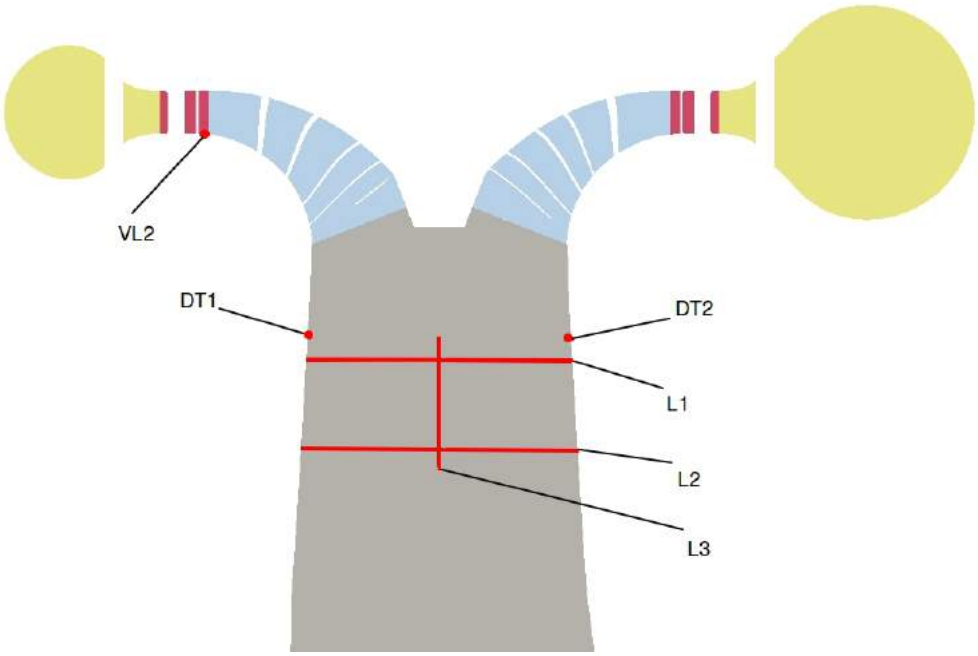

Figure 6: Pressure sensor and velocity measurement locations.

	$x\ [mm]$	$y\ [mm]$	$z\ [mm]$	n_{points}
L1 Start	25.96	133.55	-338.6	
L1 End	-25.56	-131.49	-338.6	28
L2 Start	25.96	133.55	-458.6	
L2 End	-25.56	-131.49	-458.6	28
L3 Start	0	0	-488.6	
L3 End	0	0	-308.6	18

Table 5: Velocity measurement lines.

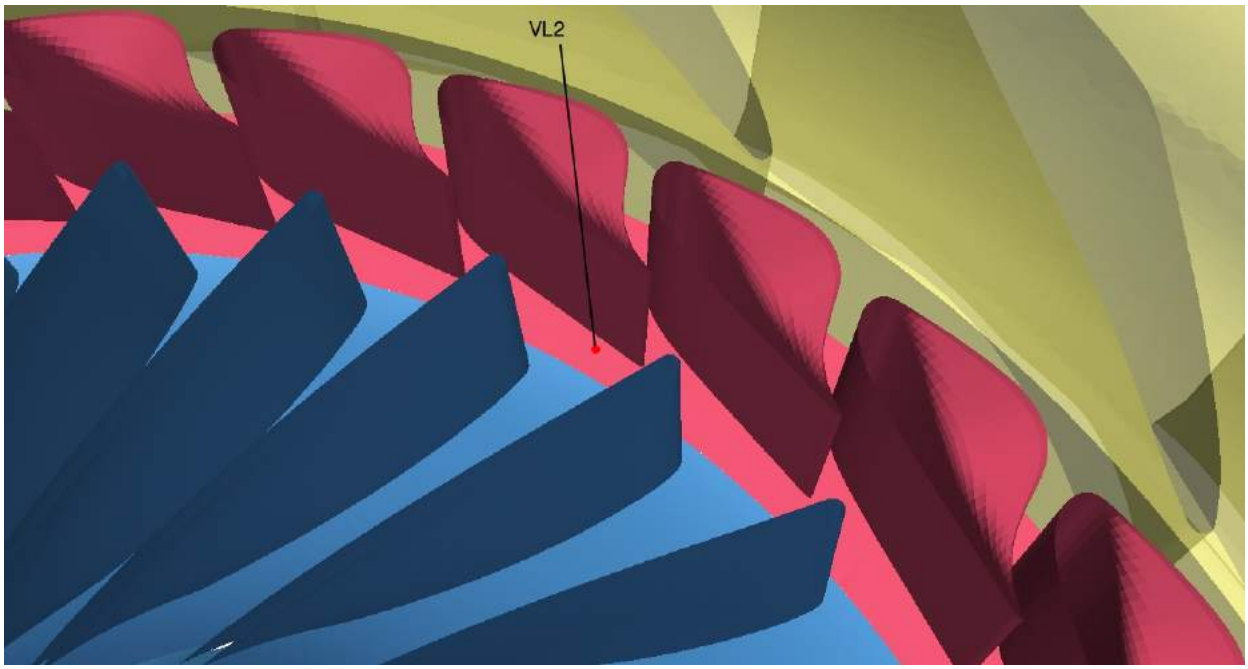

Figure 7: VL2 pressure sensor, located between guide vane suction surface and runner blade leading edge.

4.1.1 Operating Conditions

Experiments were conducted in both steady (constant flow rate/power output) and transient operating regimes. Three operating points were selected for the steady state measurements: part load (PL- guide vane angle 6.72°), best efficiency point (BEP - guide vane angle 9.84°), and high load (HL - guide vane angle 12.43°). Four different transient regime scenarios were experimentally investigated. However, in present work, flow simulation is performed only for load reduction phase, which is achieved by rotating the guide vanes from best efficiency point position (BEP) to part load (PL). During the experimental investigation of transient regimes the runner rotation speed was held constant at 333 min^{-1}. Operating conditions used in the numerical model are adjusted

to the corresponding experimental conditions. Quantities of net head and efficiency presented by Francis 99 workshop (Table 6) are calculated by Equation (30).

Table 6: Three characteristic operating points of steady operation experiments. [28]

Parameter	Part load	BEP	High load
Guide vane angle α [◦]	6.72	9.84	12.43
Net head H $[m]$	11.87	11.94	12.43
Flow rate Q $[m^3/s]$	0.13962	0.19959	0.24246
Torque T $[Nm]$	416.39	616.13	740.54
Friction torque T_f $[Nm]$	4.40	4.52	3.85
Runner rotation speed min^{-1}	332.84	332.59	332.59
Casing inlet abs. pressure p_i $[kPa]$	218.08	215.57	212.38
Draft tube outlet abs. pressure p_o $[kPa]$	113.17	111.13	109.59
Hydraulic efficiency η [%]	90.13	92.39	91.71
Water density ρ $[kg/m^3]$		999.8	
Kinematic viscosity ν $[m^2/s]$		9.57e-07	

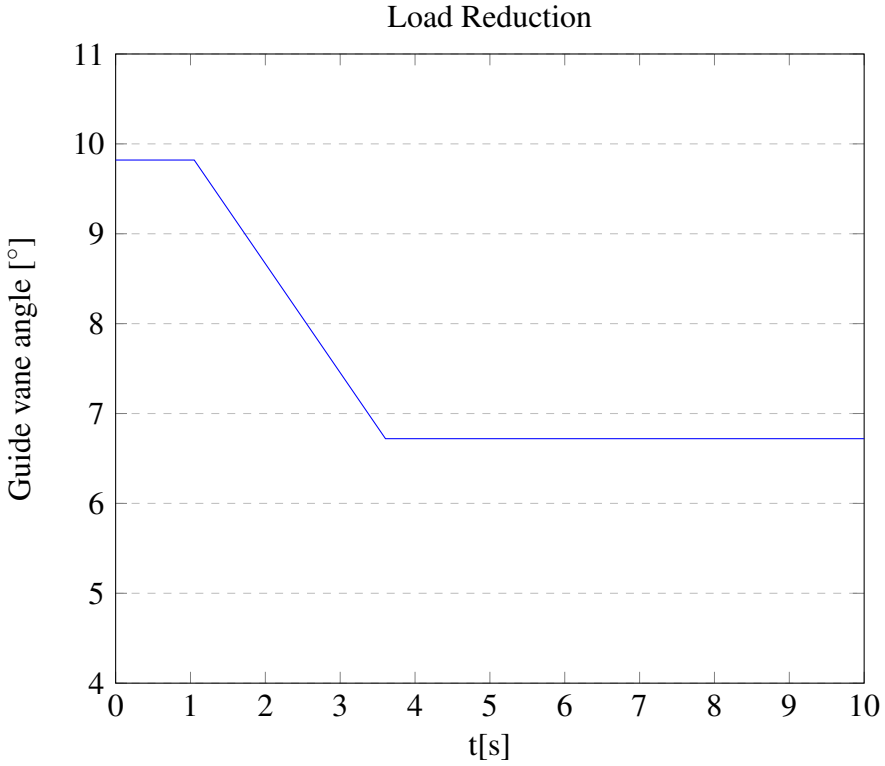

Figure 8: Guide vane angle change during load reduction experiments.

4.2 Computational Domain

A number of modeling approaches have been used regarding the choice of the computational domain and rotor-stator interface. Balancing between level of detail and computational resources have been a major issue. Two types of computational domains are used in present work:

1. *Single flow channel model*: a reduced model is used, comprised of a single flow channel with periodic boundaries (Figure 10b).

2. *Full runner model*: guide vane stage, runner and draft tube are represented with their entire geometry (Figure 10a).

In both cases spiral channel with stay vanes isn't modeled, making the plane between the guide vanes and stay vanes a domain inlet, as shown in Figure 9. Since the runner consists of fifteen full blades and fifteen splitter blades, the single representative flow channel is defined to include both a splitter and a full blade, while in the distributor two guide vanes are modeled explicitly. The interface between distributor and runner is a cylindrical surface which in full model (Figure 10a) encircles the domain entirely.

In the reduced model only a part of inlet surface is represented, with the height in z direction constant, the length of the arc a depends on the number of blades included in the model.

On the distributor side it is:

$$a = 2 \times \frac{360^\circ}{n_{guide\ vanes}} = 2 \times \frac{360^\circ}{28} = 25.714^\circ \tag{47}$$

On the runner side it is:

$$a = 2 \times \frac{360^\circ}{n_{runner\ blades}} = 2 \times \frac{360^\circ}{30} = 24^\circ \tag{48}$$

In order to avoid uncovered mesh faces for the sake of numerical stability in sliding grid simulation, a modeling assumption is made that these arcs are equal, matching the interface surfaces of the runner and distributor mesh zones. The runner zone periodic boundaries are rotated by $\frac{25.714-24}{2} = \pm 0.857^\circ$ around the z axis, extending the runner zone slightly. The validation of this approach is achieved by comparison of full model results (Fig. 10a) with the reduced model (Fig. 10b) in Section 5.3.

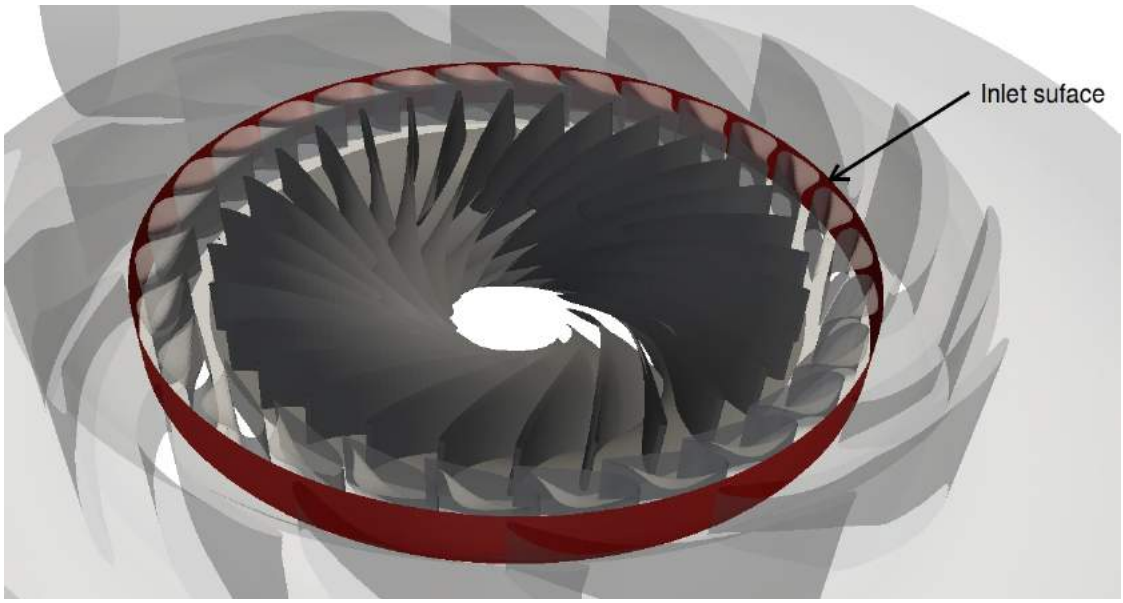

Figure 9: Inlet surface of the reduced computational domain.

(a) (b)

Figure 10: Computational domains used in present work: (a) "Full model" (b) "Single flow channel model".

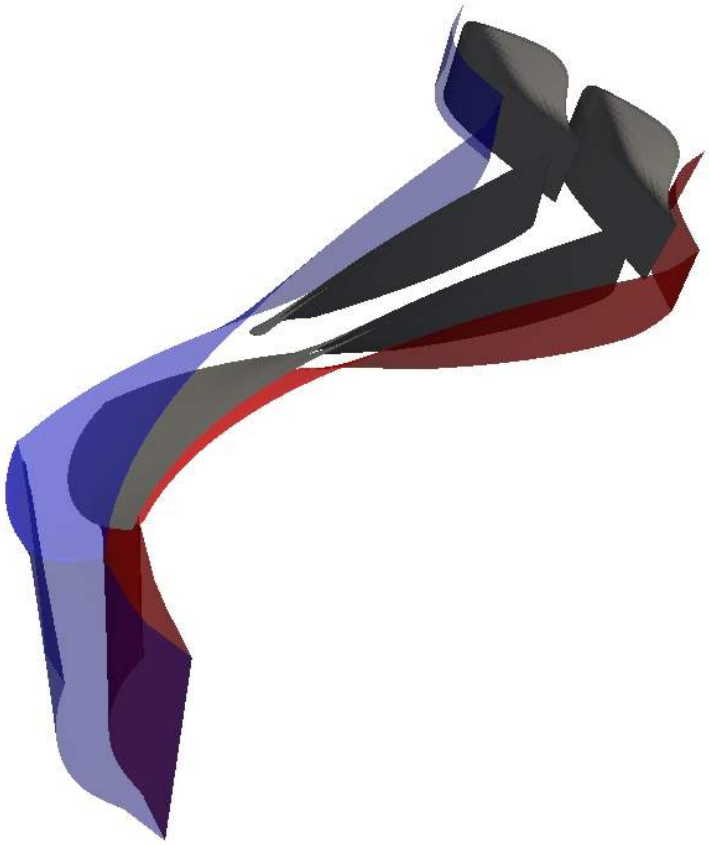

Figure 11: Periodic surfaces of the single flow channel domain.

4.3 Computational Grid

A fully block structured hexahedral mesh was created manually using mesh generation tool Pointwise®. The unusual irregularity of the guide vane surface, as well as highly twisted runner blades had to be approached carefully. Another focus in mesh generation was towards near wall spacing, in order to allow for proper wall function modeling i.e. $y^+ > 30$ (Section 2.2.4).

4.3.1 Mesh Size and Quality

Mesh was created for the single blade passage domain first, and the full model grid is subsequently constructed by copying and merging single channel mesh segments along the turbine rotation axis. Interface between distributor and runner mesh zone, as well as runner and draft tube zone is handled by GGI interface feature in `foam-extend` described in Section 3.1. Mesh size is presented in Table 7. Mesh quality is assessed using `OpenFOAM`'s diagnostic tool `checkMesh`,

Table 7: Mesh sizes for the two computational domains.

	Single flow channel	Full model
Domain part	Number of cells	
Distributor (guide vanes)	126 070	1 764 980
Runner	273 560	4 047 225
Draft tube	88 711	430 474
Total	488 341	6 242 679

the results are showed in Table 8. There are no skewed or severely non-orthogonal faces in the domain at the beginning of the simulation. Due to mesh motion these values change with time as well, as soon as mesh quality degrades, i.e. an inverted face appears, a new manually generated mesh is supplied at that time step.

Table 8: Mesh quality metrics.

	Maximum	Average	Threshold
Non-orthogonality	65.75	25.68	70
Skewness	3.45		4.0
Aspect ratio (Full model)	141.3 (27.57)		

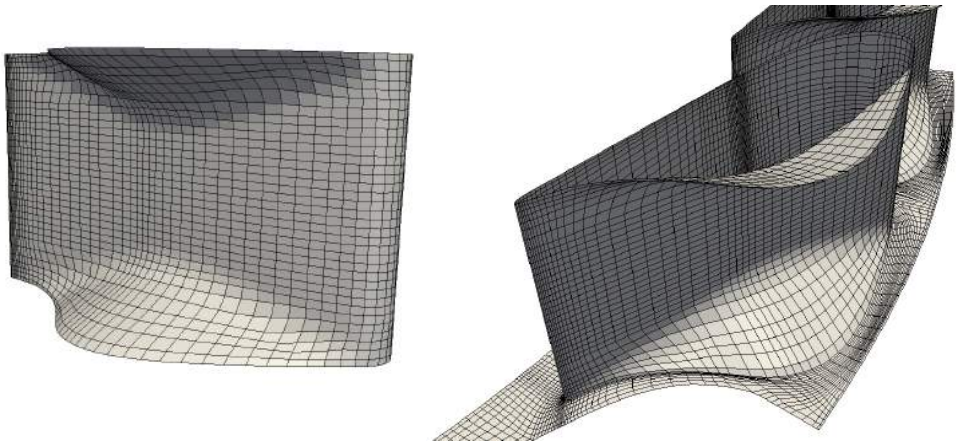

(a) (b)

Figure 12: View of the distributor (guide vane) mesh.

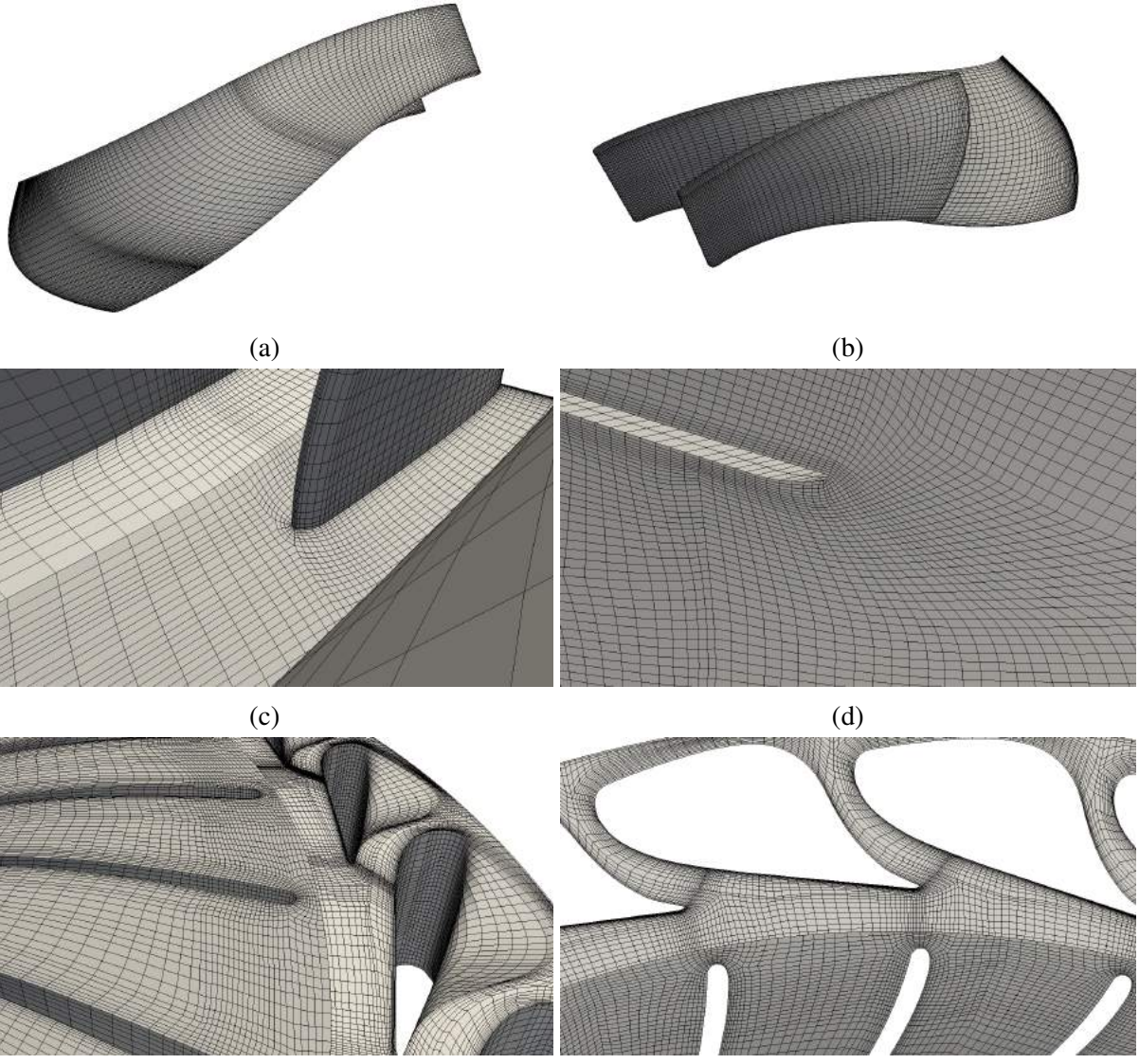

(a) (b)

(c) (d)

(e) (f)

Figure 13: View of the runner mesh (a-d) and distributor/runner interface (e-f).

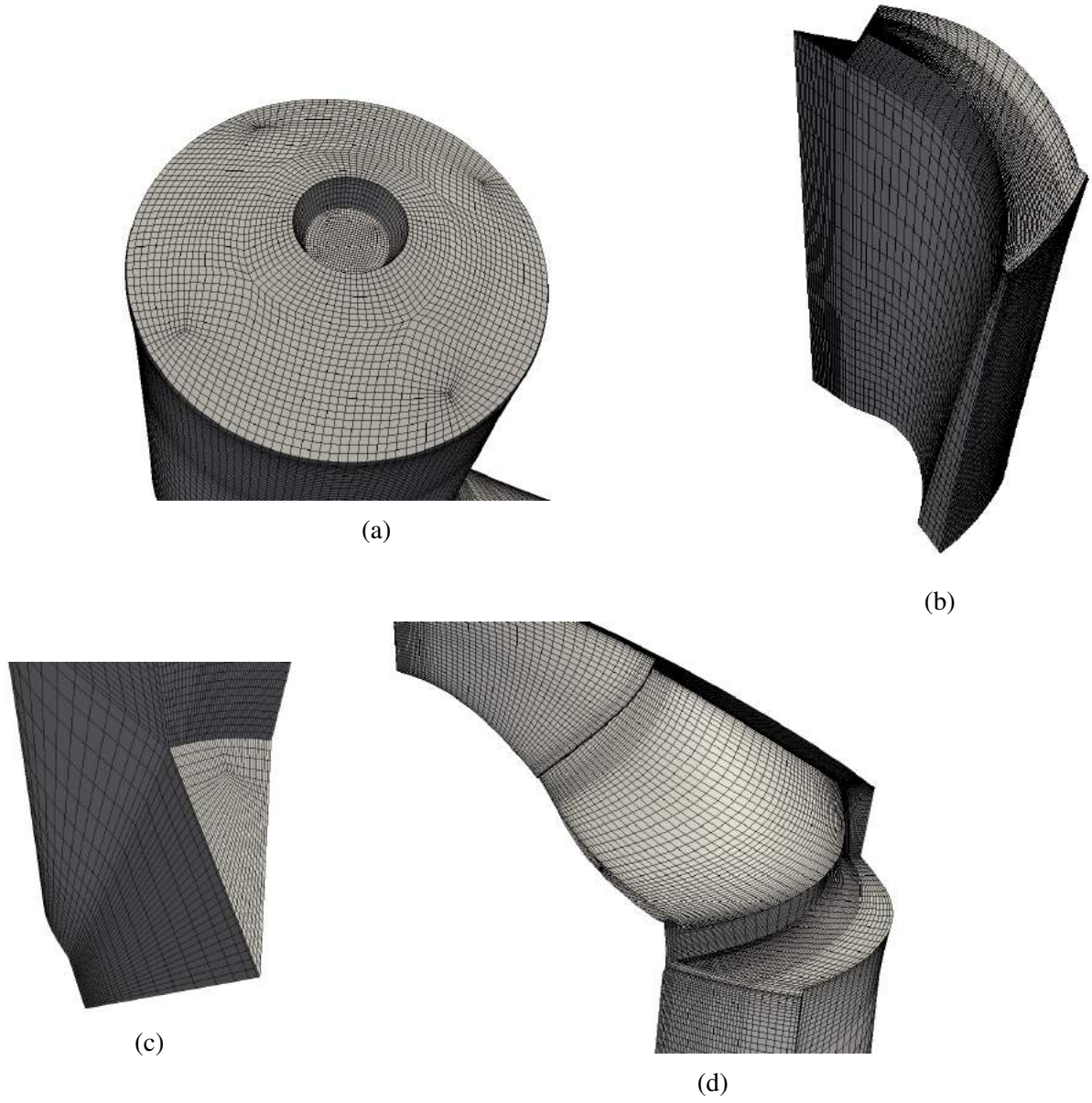

Figure 14: View of the draft tube mesh for full domain (a), single flow channel domain (b-c) and runner/draft tube interface (d).

4.3.2 y^+ Values

Wall function modeling approach for simulation of boundary layer in turbulent flows is used in present work, both in steady state and transient simulations (Section 2.2.4). The y^+ values presented here are calculated using the steady state MRF simulation with standard $k-\varepsilon$ turbulence model (Section 2.2.2). Table 9 shows the average, minimum an maximum y^+ values at the non-slip wall type of domain boundaries.

Table 9: Values of y^+ for $k-\varepsilon$ model at the no-slip wall boundaries, at the BEP operating point

	Average	Minimum	Maximum
Guide vanes	39.41	14.62	88.6
Runner blades	34.59	8.79	76.39
Runner hub	84.27	15.9	200.3
Runner shroud	70.83	19.47	136.54
Distributor hub & shroud	130.69	25.49	357
Draft tube walls	81.66	45.7	161.1

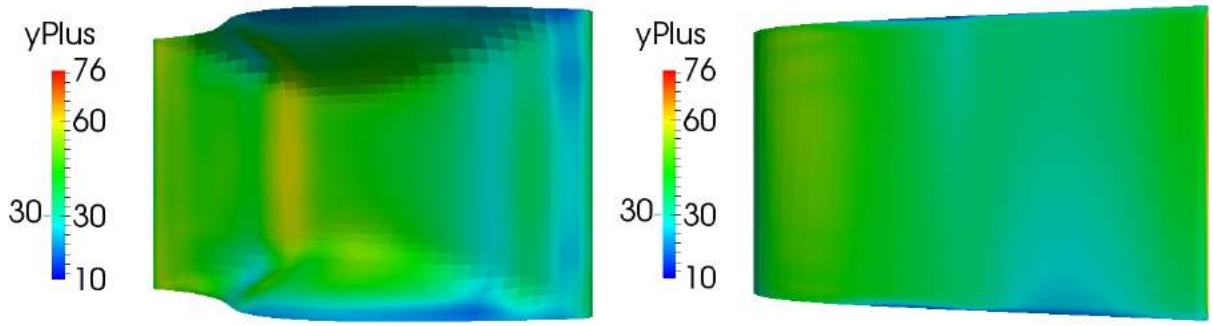

(a) Pressure side (b) Suction side

Figure 15: y^+ values at the guide vane wall

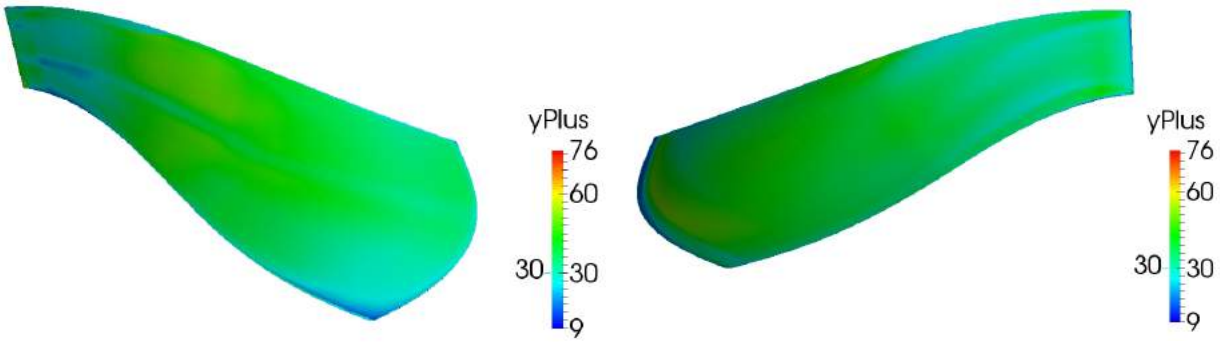

(a) Pressure side (b) Suction side

Figure 16: y^+ values at the runner blade wall

5 Simulations of Steady Operating Regime

In this section a steady turbine operation, at the best efficiency operating point will be presented. Both transient sliding-grid approach (Section 3.2.2) and steady-state, multiple reference frames model (Section 3.2.1) were used for this purpose, and calculations were made for both reduced and full geometry computational domains (Section 4.2).

5.1 Boundary Conditions

Dirichlet, Neumann or mixed conditions are set at the computational domain boundaries. Inlets and outlets between distinct mesh zones (distributor/runner, runner/draft tube) are coupled using `ggi` for steady and `overlapGgi` for sliding grid simulation. For single representative flow channel domain, the periodic boundaries are handled by `cyclicGgi` boundary condition. Table 10 systematizes domain boundary conditions for modeled quantities with their respective values. Some of the prescribed values are clarified in following subsections.

Table 10: Boundary conditions for steady operating point simulations.

Quantity	Boundary Surface	Type	Value
U	Inlet	`cylindricalInletVelocity`	$U_r = -1.4123$ $[m/s]$ $U_t = -2.1185$ $[m/s]$
	Outlet	`zeroGradient`	-
	Walls	`fixedValue`	$(0,0,0)$ $[m/s]$
	Runner (Sliding grid simulation)	`movingWallVelocity`	–
p	Inlet	`zeroGradient`	-
	Outlet	`fixedValue`	0 $[m^2/s^2]$
	Walls	`zeroGradient`	-
k	Walls	`kqRWallFunction`	-
	Inlet	`fixedValue`	0.05097 $[m^2/s^2]$
	Outlet	`zeroGradient`	-
ε	Walls	`epsilonWallFunction`	-
	Inlet	`fixedValue`	24.432 $[m^2/s^2]$
	Outlet	`zeroGradient`	-
ω	Walls	`omegaWallFunction`	-
	Inlet	`fixedValue`	5326 $[m^2/s^2]$
	Outlet	`zeroGradient`	-

5.1.1 Inlet Velocity

Velocity prescribed at the inlet boundary, closely in front of the guide vanes (Figure 9) is specified from the known volumetric flow rate and the inlet surface area. Constant normal (radial) and

tangential velocity components are set at the inlet using the `cylindricalInletVelocity` boundary condition, defined by Eq. (41). The velocity direction (Figure 17) is determined by stay vane trailing edge angle.

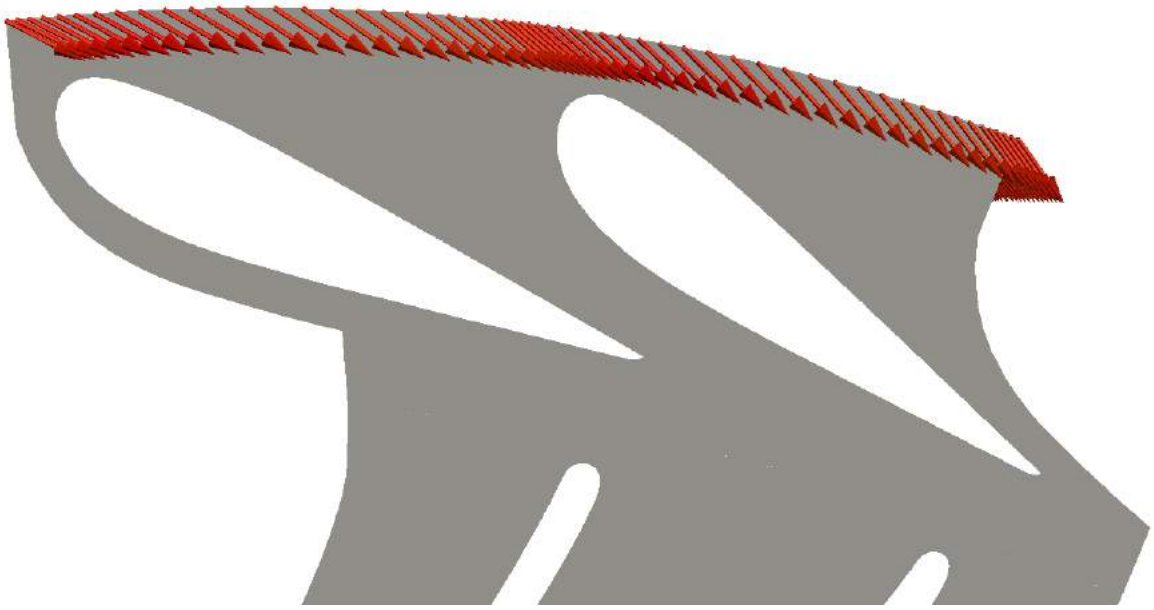

Figure 17: Inlet velocity direction prescribed as boundary condition using tangential and normal component.

5.1.2 Inlet Turbulence Quantities

Using measured flow rate oscillations during steady operation of Tokke model experiments, given by Francis 99 workshop [28], the turbulence intensity at the spiral channel inlet can be calculated using Equation (45):

$$I_{SC} = \frac{\sqrt{\overline{(u')^2}}}{\overline{u}} = \sqrt{\frac{1}{N}\sum_{i=1}^{N}\left(u'_{SC}\right)^2}\,\frac{1}{\overline{u}_{SC}} = 1.45\%$$

where N denotes the number of velocity measurements.

Turbulence intensity at the inlet surface of the computational domain is assumed to be around 5 times greater then at the spiral casing entrance, which leads to the estimate of $I = 5I_{SC} = 7.24\%$. With this assumption turbulence kinetic energy is calculated from Equation (44) and a value of $k = 0.05097\ [m^2/s^2]$ is prescribed. Turbulence dissipation rate and specific dissipation rate are calculated using Equation (46) which leads to $\varepsilon = 24.432\ [m^2/s^2]$ and $\omega = 5326\ [m^2/s^2]$. Assumption that $\beta = \nu_t/\nu = 10$ was used thereby.

5.2 Simulation Setup

For steady state calculations presented in this chapter `MRFSimpleFoam` solver application present in `foam-extend 3.2` was used. It calculates incompressible flow based on SIMPLE [21] algorithm for pressure velocity coupling and enables addition of MRF (Section 3.2.1) zones, an ability which was put to use in order to set the constant runner rotation speed of 333 min^{-1}. Table 11 shows linear solver settings, while Table 12 shows chosen relaxation factors. For pressure correction phase an algebraic multi-grid linear solver is chosen (`amgSolver`) with PAMG policy, for the rest of the variables a stabilized bi-conjugate gradient (`BiCGStab`) solver is used with the diagonal incomplete LU decomposition preconditioner.

Table 11: Linear solver settings for steady-state simulations.

Quantity	Linear solver	Absolute tolerance	Relative tolerance
p	amgSolver (PAMG)	1e-07	0.001
U	BiCGStab (DILU)	1e-06	0
k	BiCGStab (DILU)	1e-06	0
ε/ω	BiCGStab (DILU)	1e-06	0

Table 12: Under-relaxation factors for steady-state simulations.

Quantity	Under-relaxation factor (single channel)	Under-relaxation factor (full runner)
p	0.4	0.2
U	0.7	0.5
k	0.7	0.5
ε/ω	0.7	0.5

For sliding grid calculations a transient solver application with dynamic mesh handling `pimpleDyMFoam` present in `foam-extend 3.2` was used. It is an incompressible solver based on PIMPLE algorithm for pressure velocity coupling. Runner rotation is set to be constant at the velocity of 333 $[min^{-1}]$. Table 13 shows linear solver settings, while the under-relaxation factors are the same as in single channel simulations in steady state, as shown in Table 12. For pressure correction phase a preconditioned conjugate gradient linear solver is chosen (`PCG`) with diagonal incomplete-Cholesky preconditioner. For the rest of the variables a stabilized bi-conjugate gradient (`BiCGStab`) solver is used with the diagonal incomplete LU decomposition preconditioner.

A number of discretization schemes of different orders is available in `foam-extend`, here the ones used in present work will be mentioned as they are named in the `OpenFOAM` code. The momentum divergence term was discretized using the second order `linearUpwind` scheme, which is a blend of `linear` and `upwind` schemes. Turbulence terms were discretized using a first order `upwind` scheme. Second order `Gauss linear` scheme is used for discretization of all gradient and `Gauss linear corrected` for Laplacian terms.

Table 13: Linear solver settings for transient sliding grid simulation.

Quantity	Linear solver	Absolute tolerance	Relative tolerance
p	PCG (DIC)	1e-06	0.01
U	BiCGStab (DILU)	1e-06	0
k	BiCGStab (DILU)	1e-06	0
ε/ω	BiCGStab (DILU)	1e-06	0

5.3 Results and Discussion

5.3.1 Integral Quantities

Integral quantities commonly used to describe hydro-turbine performance are defined in Section 2.4. Since `OpenFOAM` incompressible solver applications don't include gravitational forces, the potential energy from height difference between inlet and outlet is not accounted for. The definition of head used by Francis 99 workshop when presenting their experimental results includes the height difference, as showed in Equations (28) and (30). In order to make the comparison with experiments, influence of gravitational potential ρgz was accounted for in calculation of integral values in Table 14, columns 3 & 4. Simulation results prior to addition of gravitational term are showed in columns 5 & 6 of Table 14 for clarity.

Table 14: Results of turbine output power, efficiency and head with comparison of different modeling approaches for steady operation at BEP.

Model	$P\ [W]$	$\Delta p_0 =$ Eq. (30) $H\ [m]$	$\eta\ [\%]$	$\Delta p_0 =$ Eq. (29) $H\ [m]$	$\eta\ [\%]$
Experiment	21 617	11.94	92.39	-	-
Single flow channel, steady, MRF, $k-\varepsilon$	22 109	12.41	91.12	11.76	96.28
Single flow channel, steady, MRF, $k-\omega$	21 847	12.242	91.33	11.52	96.55
Full model, steady, MRF, $k-\varepsilon$	22 302	12.54	91.0	11.90	95.92
Full model, steady, MRF, $k-\omega$	22 007	12.36	91.1	11.72	96.101
Single flow channel, transient, sliding grid, $k-\varepsilon$	23 196	13.84	85.8	13.18	90.07

5.3.2 Pressure Fields

Experimental pressure measurements are described in Section 4.1, with Table 4 and Figure 6 displaying pressure probe locations. Simulation results adjusted for atmospheric conditions are showed in comparison with experiments in Figure 20.

The gauge pressure distribution in distributor and runner flow sections is pictured in Fig. 18. Figure 19 shows gauge pressure isobars, where the guide vane trailing edge suction area is clearly visible, as well as how pressure acts on runner blade sides, contributing to energy transformation which occurs in reaction turbines of Francis type. Absolute pressure values at runner blade suction

and pressure side are showed in Figure 21.

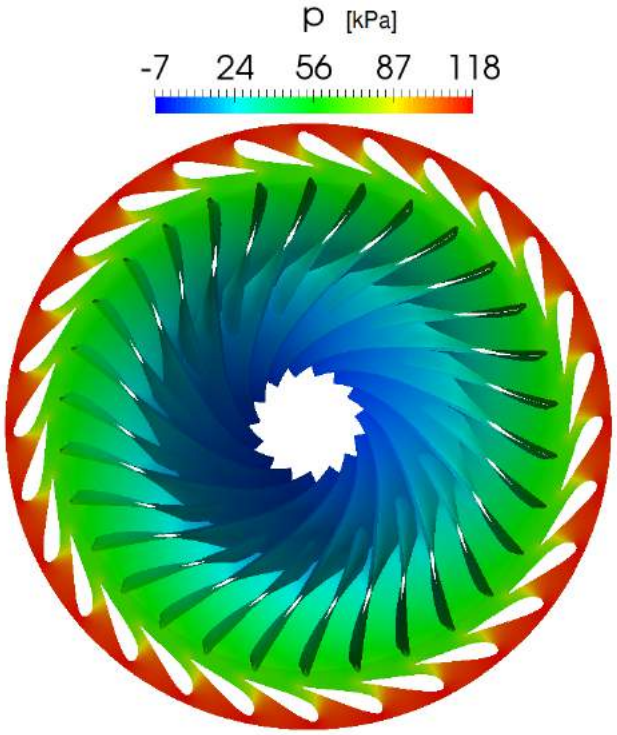

Figure 18: Gauge pressure p $[kPa]$ in the guide vane and runner flow domains (Steady state, MRF, $k-\varepsilon$).

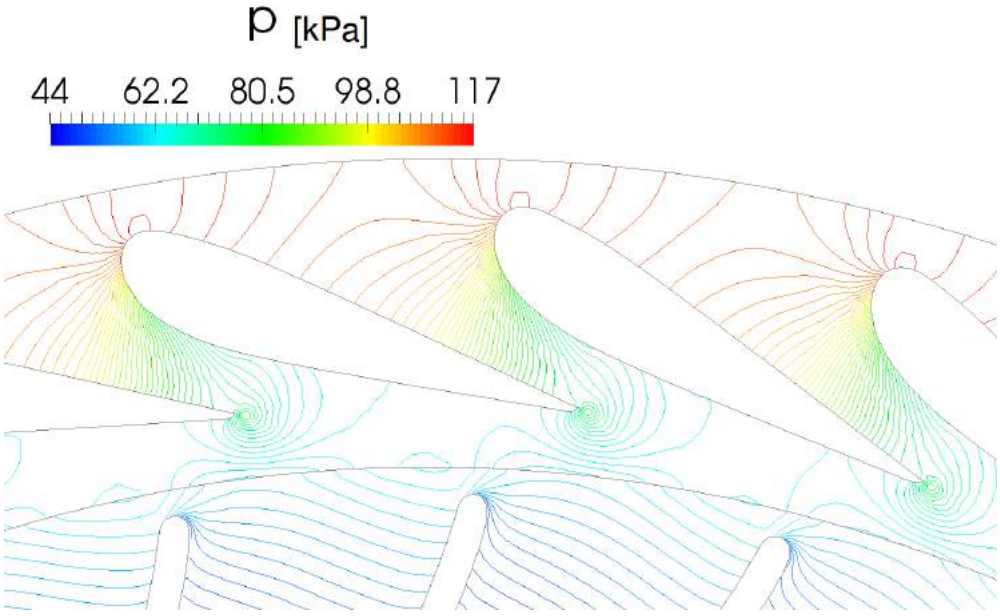

Figure 19: A detail of gauge pressure p $[kPa]$ contours around guide vanes and runner leading edges.

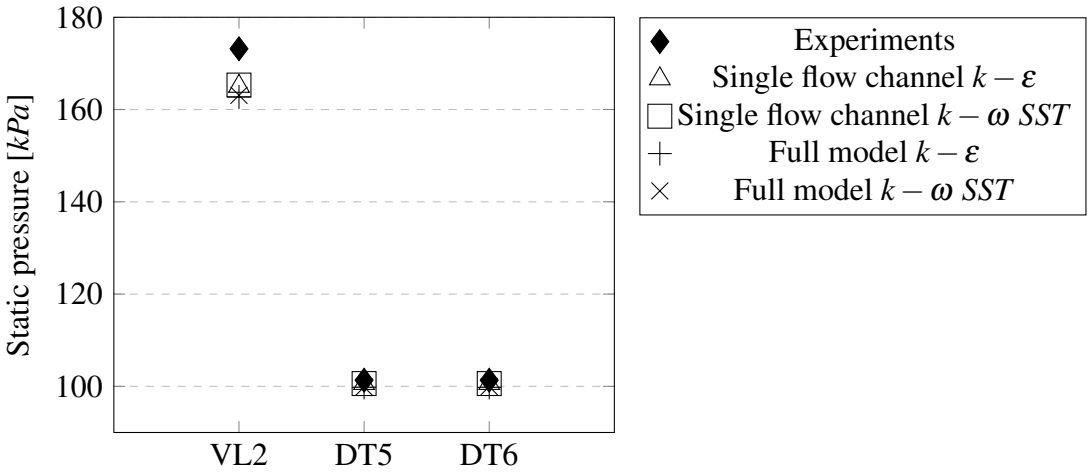

Figure 20: Static pressure (abs) values at measurement locations.

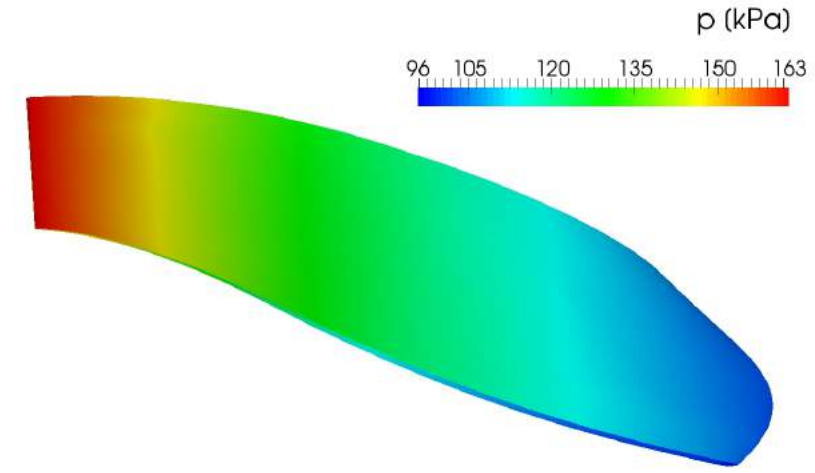

(a) Pressure side

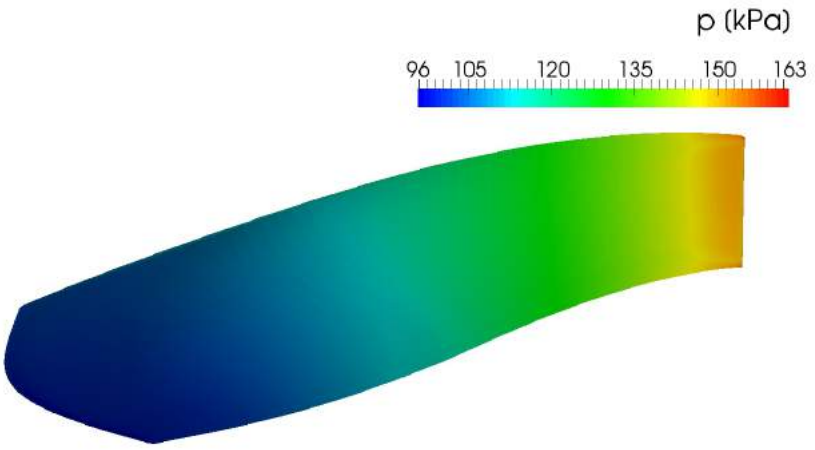

(b) Suction side

Figure 21: Static pressure (abs) values at the runner blade surface.

A transient simulation using sliding grid interface and dynamic mesh for runner rotation was used to estimate the pressure pulsations at experimental probe positions. Time domain comparison of instantaneous pressure values at BEP is presented in Figure 23 as a function of runner rotational position in degrees. At the vane-less space location (VL2) pressure oscillations correspond to runner blade passing frequency $f = 166.667\ Hz$, having an amplitude of $\approx 2\ [kPa]$. The sine wave function with the same parameters is plotted in Figure 23a for comparison with experimental and calculated data. The simulated pressure amplitude doesn't completely agree with the experimental data for VL2, also a data set with more time points would be helpful. For draft tube measurement locations these amplitude discrepancies become even more pronounced.

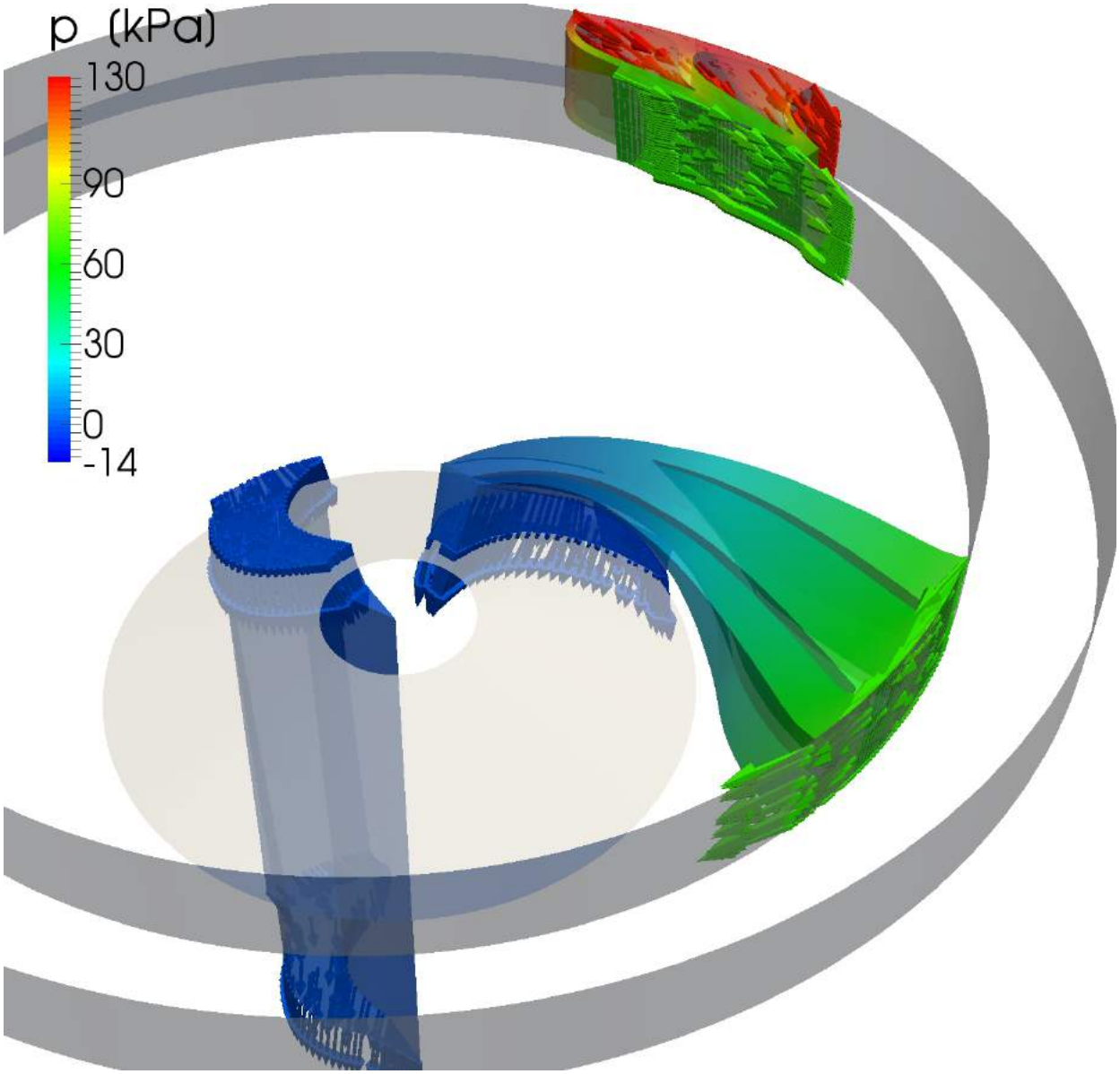

Figure 22: Gauge pressure field during transient simulations of a single flow channel at $t = 0.045\ s$, which corresponds to 90° of rotation. Arrows show velocity vectors at interface surfaces (gray).

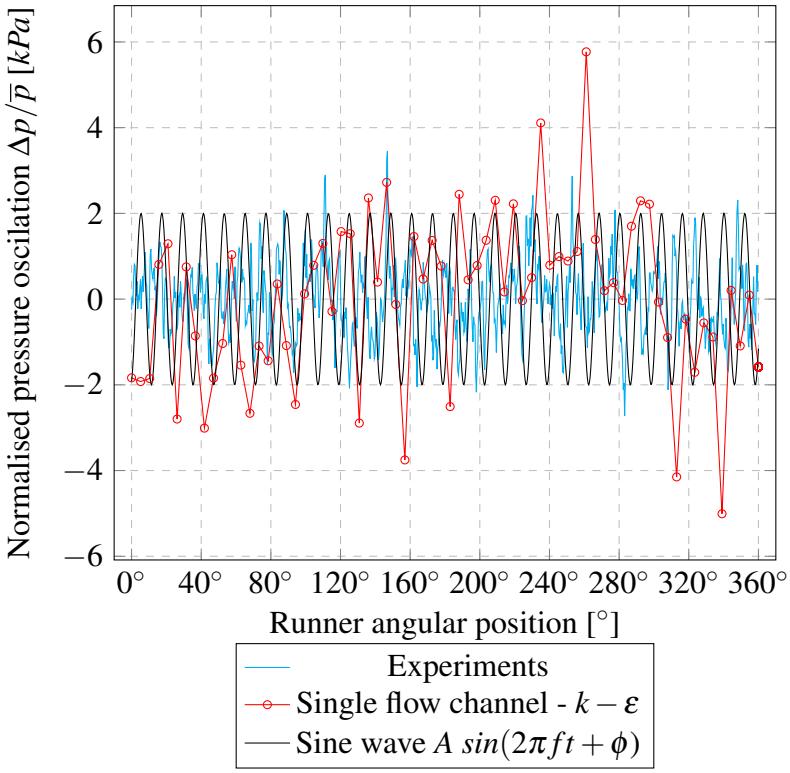

(a) Vaneless space (VL2) measurement location in BEP.

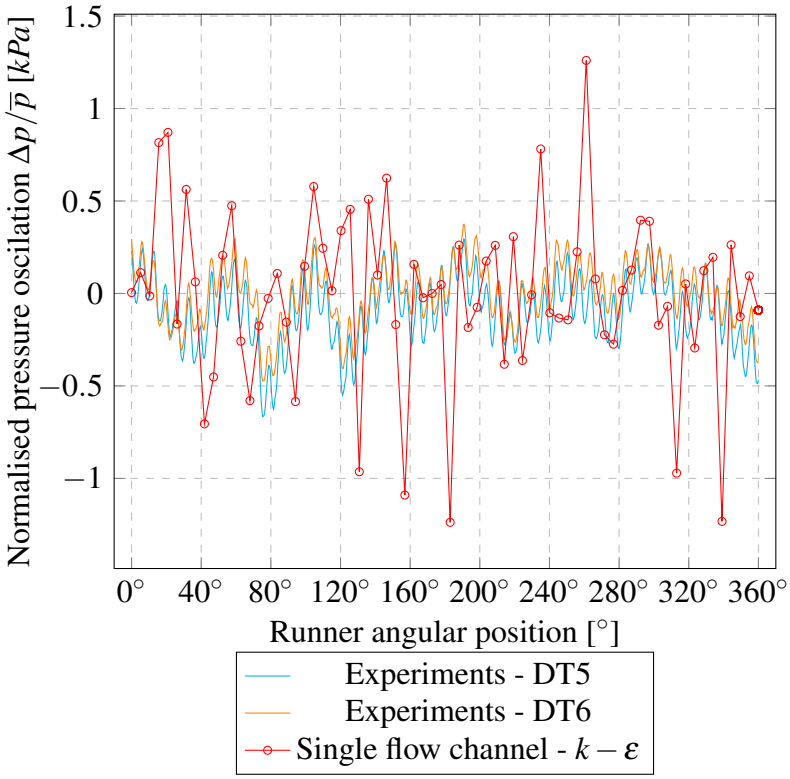

(b) Draft tube measurement locations in BEP.

Figure 23: Time-dependent pressure signal at measurement locations, as a function of runner rotation.

5.4 Velocity Fields

Rotor-stator interaction is of key interest in turbomachinery flow analysis (Section 3.2). Velocity magnitude distribution in Figure 24 shows guide vane trailing edge wakes interacting with runner blades in this area.

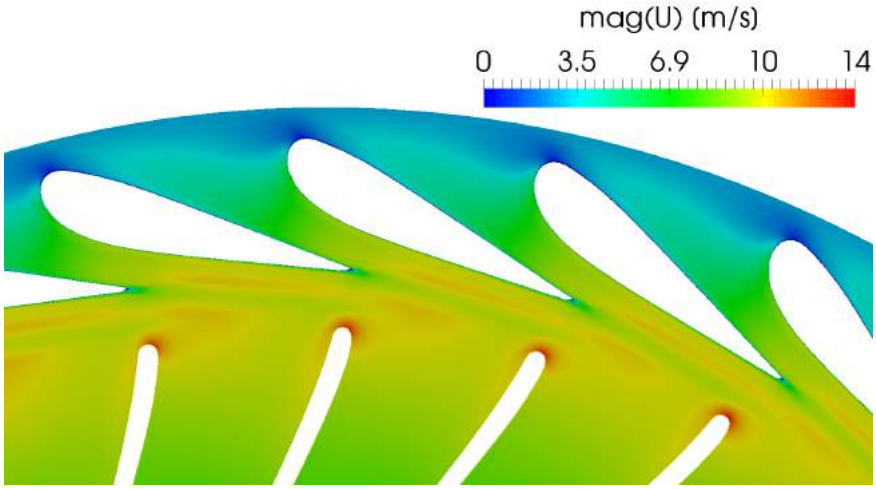

Figure 24: Velocity magnitude field $\|\mathbf{u}\|$ around guide vanes showing interaction between guide vane wake flow and runner leading edge.

A great majority of researchers in F99 first workshop reported the inability to accurately predict draft tube velocity profiles, even et best efficiency point where no swirl is expected in the draft tube [14]. The tangential velocity is negligible in experimental results at that location, but clearly expressed near the draft tube center line in RANS numerical simulations, regardless of turbulence model used. The same behavior is observed in present work, as shown in comparison with experimental data, at measurement locations showed in Figure 6. At lines L1 (Figure 25a) and L2 (Figure 25b) a discrepancy in U_θ values is visible around the centerline ($x/r = 0$), the same is more clearly showed in L3 plot (Figure 25c), as values of U_θ are overpredicted along the entire line length. Tangential velocity represents a vortex swirling around the z axis in the draft tube, also pictured with Q-criterion distribution in Figure 27.

The axial velocity (U_z) profile near the centerline is shaped by the runner hub recirculation zone, and in the vicinity of the draft tube walls, shear stress has a defining influence. U_z profile is plotted along the draft tube radial direction is Figure 25a and Figure 25a, while Figure 26 shows the distribution of U_z in the measurement planes, giving more qualitative insight. U_z is well predicted along the centerline (Fig. 25c) while overpredicted in the $x/r = \pm 0.2$ area. The source of this lies in the wake of the runner hub cone. Wake length in simulations is larger then that determined by experimental investigation. Also at the $x/r > 0$ side there is an overprediction of axial velocity. Fig. 26c shows the influence of draft tube elbow on these profiles.

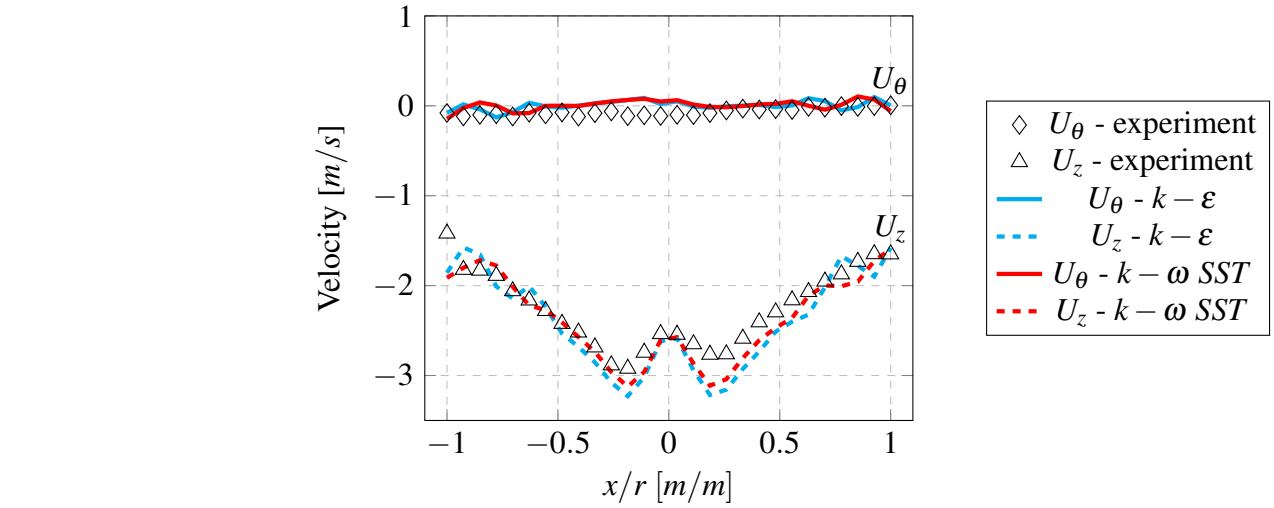

(a) LDA measurement line L1 (Table 5)

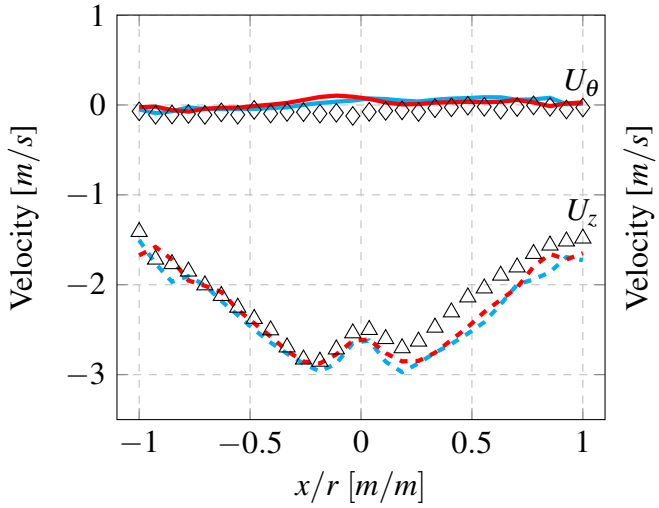

(b) LDA measurement line L2

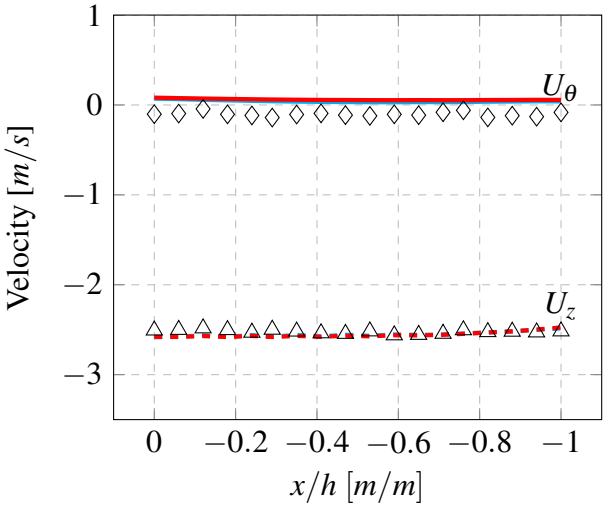

(c) LDA measurement line L3

Figure 25: Tangential (U_θ) and axial (U_z) velocity profiles compared to experimental data.

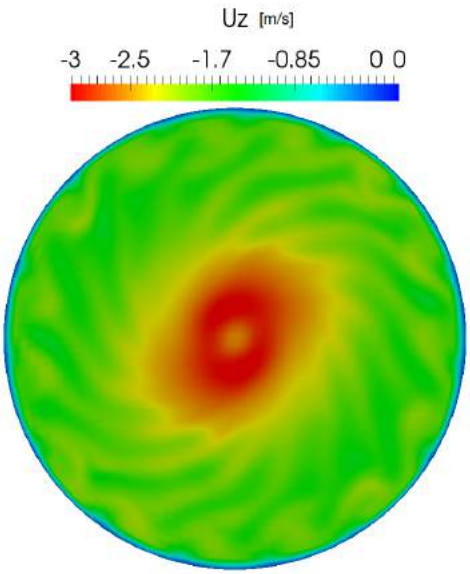

(a) Axial velocity U_z $[m/s]$ at the height of L1 measurement line.

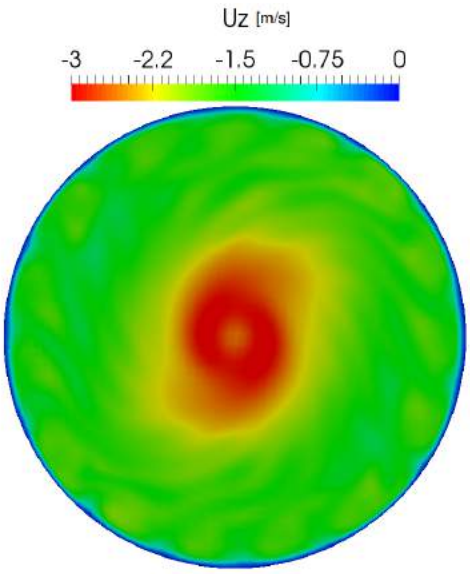

(b) Axial velocity U_z $[m/s]$ at the height of L1 measurement line.

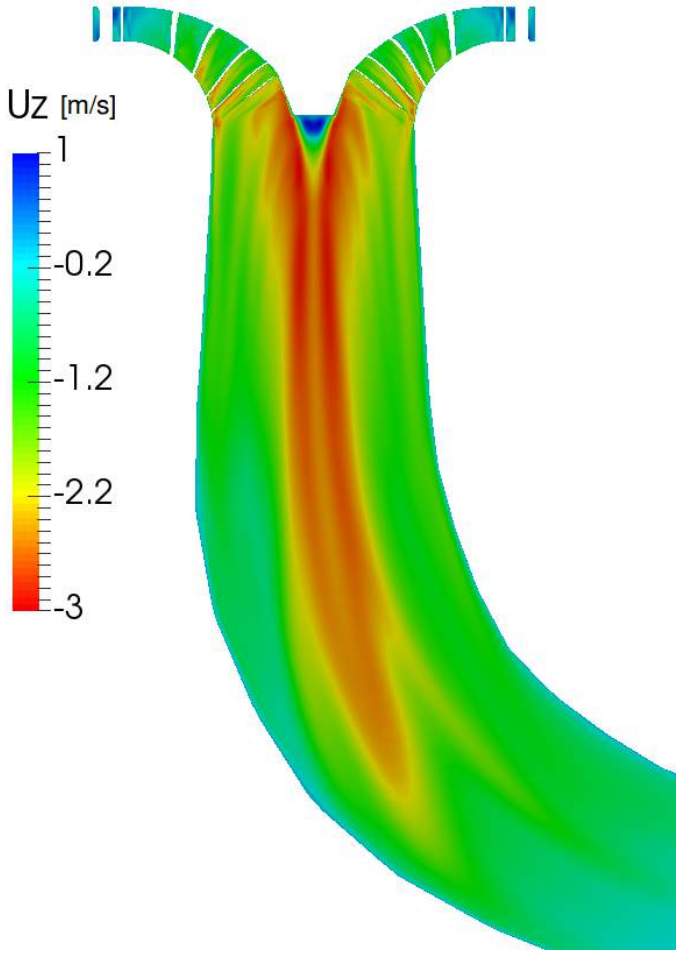

(c) Axial velocity U_z $[m/s]$ at the draft tube cross section plane.

Figure 26: U_z Velocity field in the draft tube, at the LDA measurement locations (Fig. 5).

5.5 Flow structures

Flow structures observed and qualitatively reported using Q-criterion (Section 2.3) are voritces of different scale and origin. Confirming the draft tube centerline phenomena described in previous subsection 5.4 Figure 27 shows Q distribution at the height of L1 and L2 measurement lines. Except the centerline swirl, fifteen runner trailing edge separation voritces can be identified near the wall and below runner full-length blades. Same flow structure can be observed in Figure 28 which shows Q iso-surfaces in the draft tube.

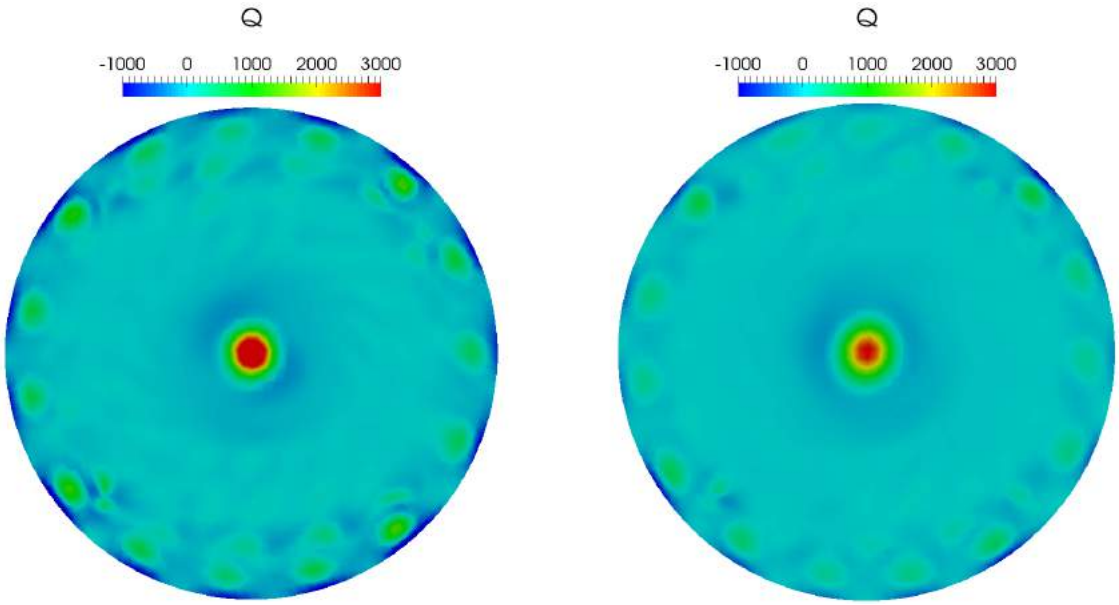

(a) Q-criterion at the height of L1 measurement line. (b) Q-criterion at the height of L2 measurement line.

Figure 27: Distribution of Q-criterion values at the velocity measurement locations (Fig. 5) in draft tube.

The Iso-surfaces of the Q-criterion, in guide vane and rotor inlet area, colored by gauge pressure are showed by Figure 29. At each guide vane pressure side a generation of vortex structures can be observed at the blade thickening, where the blade meets the hub or shroud surfaces. A generation of vortices can also be observed at the runner leading edge suction side. While described guide vane flow separation is conditioned by the unusual shape of the blade pressure side, encountering separation at the runner leading edge in the best efficiency operating point can suggest that this blade angle and position might, in fact, deviate from the actual BEP.

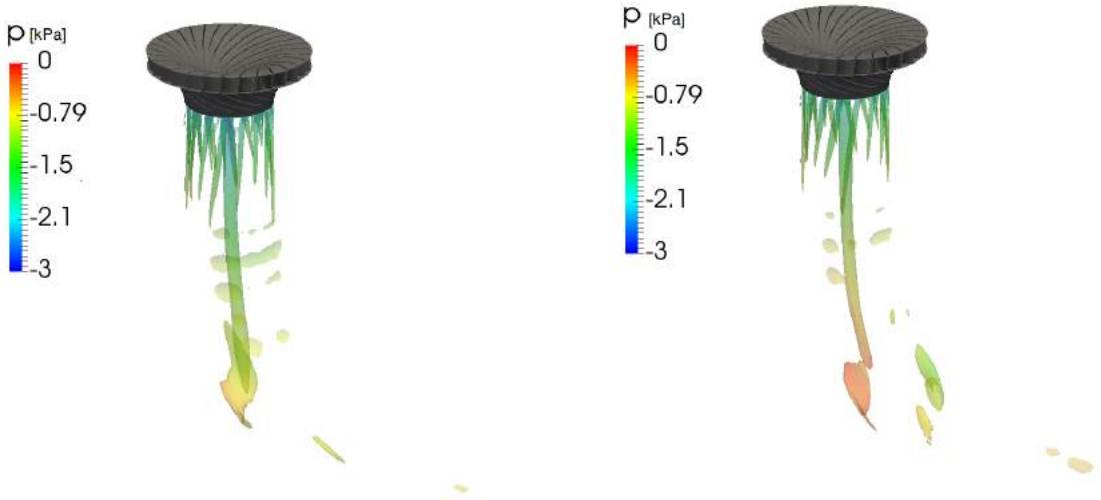

(a) $Q = 200$ iso-surface, $k - \varepsilon$ turbulence model.

(b) $Q = 200$ iso-surface, $k - \omega SST$ turbulence model.

Figure 28: Q-crterion iso-surfaces in draft tube with gauge pressure field in [kPa] at the corresponding location.

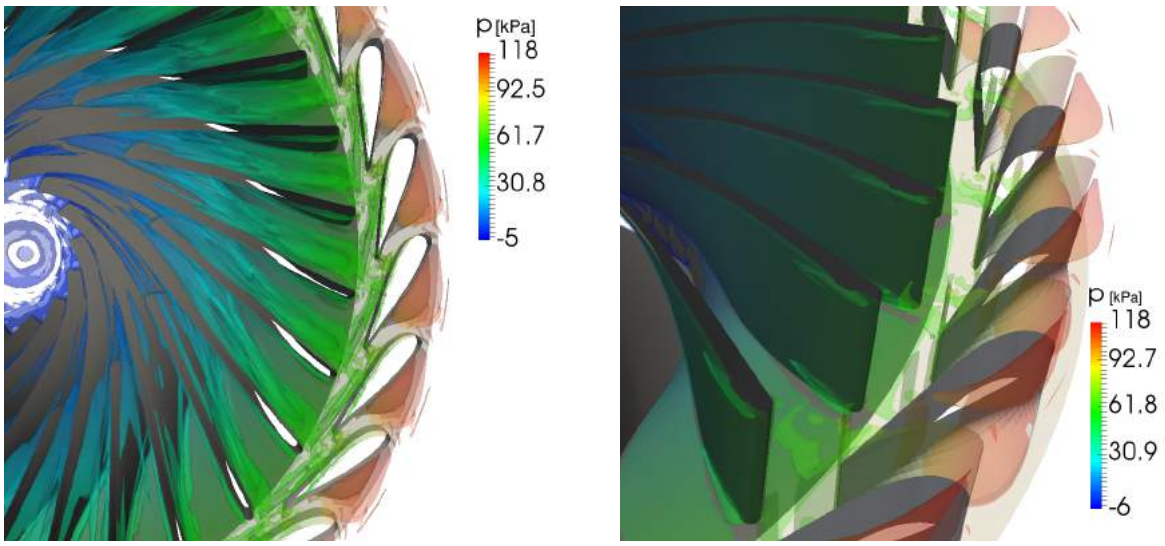

(a)

(b)

Figure 29: Vortices in rotor/stator flow channel expressed with Q-criterion ($Q = 2000$) iso-surfaces with gauge pressure field in [kPa] at the corresponding location.

6 Load Variation Simulations

Turbine transient operation was simulated for load reduction phase, form BEP to part load (Section 4.1.1), using the reduced domain (Section 4.2). Transient modeling with multiple reference frames is used. Two different approaches regarding the choice of boundary conditions are tested. One with prescribed head, in which the reduction of flow rate is part of the solution, and an approach where the flow is prescribed at the inlet as a time-dependent function. $k-\varepsilon$ turbulence model is used in both cases. Closing of guide vanes is accomplished using mesh motion solver described in Section 3.3.

6.1 Boundary Conditions

Dirichlet, Neumann or mixed conditions are set at the computational domain boundaries. Inlets and outlets between mesh zones (distributor/runner, runner/draft tube) are coupled using `ggi` interfaces (Section 3.1). In a reduced domain, a single representative flow channel is modeled (Section 4.2) by splitting the flow domain which introduces the requirement to handle the periodic boundaries with `cyclicGgi` boundary condition.

6.1.1 Prescribed Head at The Inlet

The head is prescribed in `foam-extend` as total pressure at the inlet, calculated from values provided for best efficiency point (Section 4.1.1) using expression (28). Static pressure was prescribed at the outlet. Guide vane rotation is defined as the velocity of surface points by the boundary condition described in Section 3.3.4. Table 15 shows domain boundary conditions for model quantities with their respective values.

Table 15: Boundary conditions for load variation simulations with prescribed head at the inlet.

Quantity	Boundary	Type	Value
U	Walls	`fixedValue`	$(0,0,0)$ $[m/s]$
	Guide vane walls	`movingWallVelocity`	$(0,0,0)$ $[m/s]$
	Inlet	`presureDirected-` `CylindricalInletVelocity`	$\hat{U}_r = 0.5547$ $[-]$ $\hat{U}_t = 0.832$ $[-]$
	Outlet	`zeroGradient`	-
p	Inlet	`totalPressure`	$p_0 = 117.251$ $[kPa]$
	Outlet	`fixedValue`	0 $[m^2/s^2]$
	Walls	`zeroGradient`	-
k	Walls	`kqRWallFunction`	-
	Inlet	`turbulentIntensity-` `KineticEnergyInlet`	$I = 7.24$ $[\%]$
	Outlet	`zeroGradient`	-
ε	Walls	`epsilonWallFunction`	-
	Inlet	`turbulentMixingLength-` `DissipationRateInlet`	$l = 7.73917e-05$ $[m^2/s^2]$
	Outlet	`zeroGradient`	-
pointMotionU	Guide vanes	`angularVelocity`	$\alpha = 1.1923$ $[^\circ/s]$
	Other walls	`slip`	-
	Inlet	`slip`	-
	Outlet	`splip`	-

Inlet Velocity

Velocity prescribed at the inlet boundary (Figure 9) is specified from the calculated pressure difference and user defined direction vector. Normal (radial) and tangential direction vector components are set at the inlet using the `presureDirectedCylindricalInletVelocity` boundary condition defined in Section 3.4.2. The velocity direction is determined by stay vane trailing edge angle.

Inlet Turbulence Quantities

Using measured flow rate, oscillations during steady operation of Tokke model experiments turbulence intensity were calculated using equation 45 as described in Section 5.1.2. Since the flow rate is changing during simulation time, turbulence intensity at the inlet surface of the computational domain is calculated by `turbulentIntensityKineticEnergyInlet` boundary condition using prescribed turbulence intensity $I = 7.24\%$ at each time-step. Turbulence dissipation rate is similarly determined by `turbulentMixingLengthDissipationRateInlet` boundary condition where user prescribes the turbulence length scale quantity l, defined by expression:

$$l = C_v^{3/4} \frac{k^{3/2}}{\varepsilon} \tag{49}$$

6.1.2 Prescribed Flow Rate at the Inlet

Flow rate is prescribed according to experimental data given by Francis 99 workshop (Section 4.1.1), where discharge Q during guide vane rotation is showed in Figure 30.

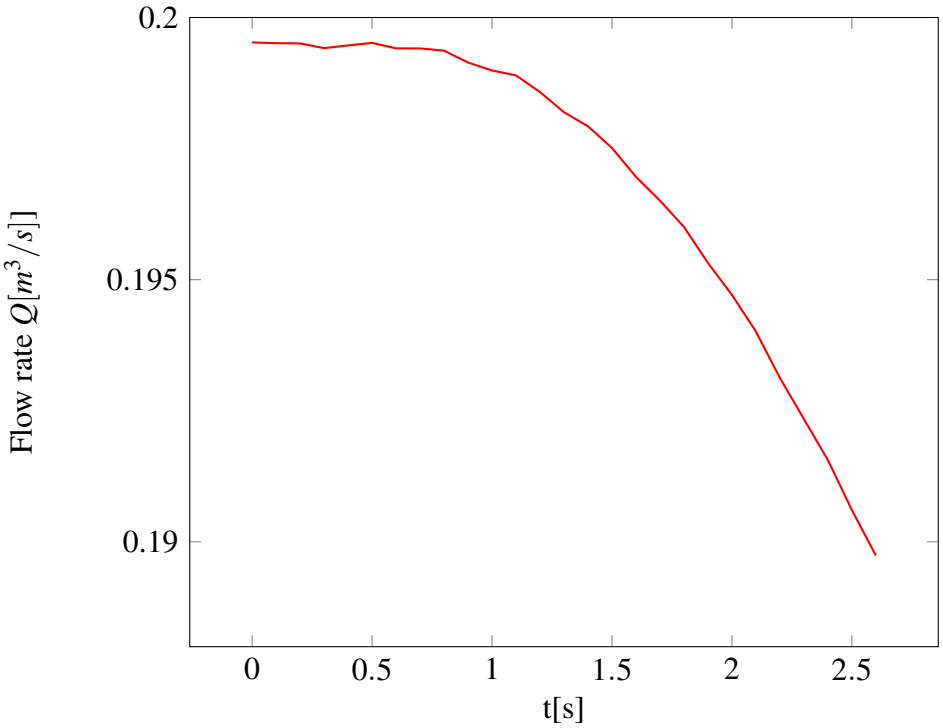

Figure 30: Prescribed flow rate at the inlet during load reduction.

Table 16 shows domain boundary conditions for model quantities with their respective values. The rest of the considerations from Section 5.1 for steady case are valid here as well.
Velocity at the inlet is prescribed using expression (41), as described in Section 5.1.1. The requirement to set the inlet velocity as a time-depending inlet value was met by implementing `groovyBC` feature of *swak4Foam* library [29]. Guide vane rotation is defined as the velocity of surface points by the boundary condition described in Section 3.3.4. Inlet turbulence quantities are defined as described in Section 5.1.2.

Table 16: Boundary conditions for load variation simulations with prescribed flow rate at the inlet.

Quantity	Boundary Surface	Type	Value
U	Inlet	`groovyBC` Eq. (41)	$U_r = -1.4123 \rightarrow -1.343$ $[m/s]$
			$U_t = -2.1185 \rightarrow -2.015$ $[m/s]$
	Outlet	`zeroGradient`	-
	Walls	`fixedValue`	$(0,0,0)$ $[m/s]$
	Guide vane walls	`movingWallVelocity`	$(0,0,0)$ $[m/s]$
p	Inlet	`zeroGradient`	-
	Outlet	`fixedValue`	0 $[m^2/s^2]$
	Walls	`zeroGradient`	-
k	Walls	`kqRWallFunction`	-
	Inlet	`fixedValue`	0.05097 $[m^2/s^2]$
	Outlet	`zeroGradient`	-
ε	Walls	`epsilonWallFunction`	-
	Inlet	`fixedValue`	24.432 $[m^2/s^2]$
	Outlet	`zeroGradient`	-
pointMotionU	Guide vanes	`angularVelocity`	$\alpha = 1.1923$ $[^\circ/s]$
	Other walls	`slip`	-
	Inlet	`slip`	-
	Outlet	`splip`	-

6.2 Simulation Setup

For load variation simulations presented in this chapter a modified version of `pimpleDyMFoam` solver from `foam-extend 3.2` was used. Incorporation of multiple reference frame model to PIMPLE solver had to be done first, as explained in Section 3.2.1 to account for constant runner rotation speed of 333 min^{-1}. Table 17 shows linear solver settings, while Table 18 shows chosen relaxation factors. For pressure correction phase an algebraic multi-grid linear solver is chosen (`amgSolver`) with PAMG policy, for the rest of the flow variables a stabilized bi-conjugate gradient (`BiCGStab`) solver is used with the diagonal incomplete LU decomposition preconditioner. Motion of mesh points is solved using a preconditioned conjugate gradient linear solver (`PCG`) with diagonal incomplete-Cholesky preconditioner.

Table 17: Linear solver settings for load variation simulations.

Quantity	Linear solver	Absolute tolerance	Relative tolerance
p	amgSolver (PAMG)	1e-07	0.001
U	BiCGStab (DILU)	1e-06	0
k	BiCGStab (DILU)	1e-06	0
ε/ω	BiCGStab (DILU)	1e-06	0
cellMotionU	PCG (DIC)	1e-08	0
cellMotionUx	PCG (DIC)	1e-08	0

Table 18: Under-relaxation factors for load variation simulation.

Quantity	Under-relaxation factor (single channel)
p	0.4
U	0.7
k	0.7
ε/ω	0.7

6.3 Results and Discussion

6.3.1 Pressure Data

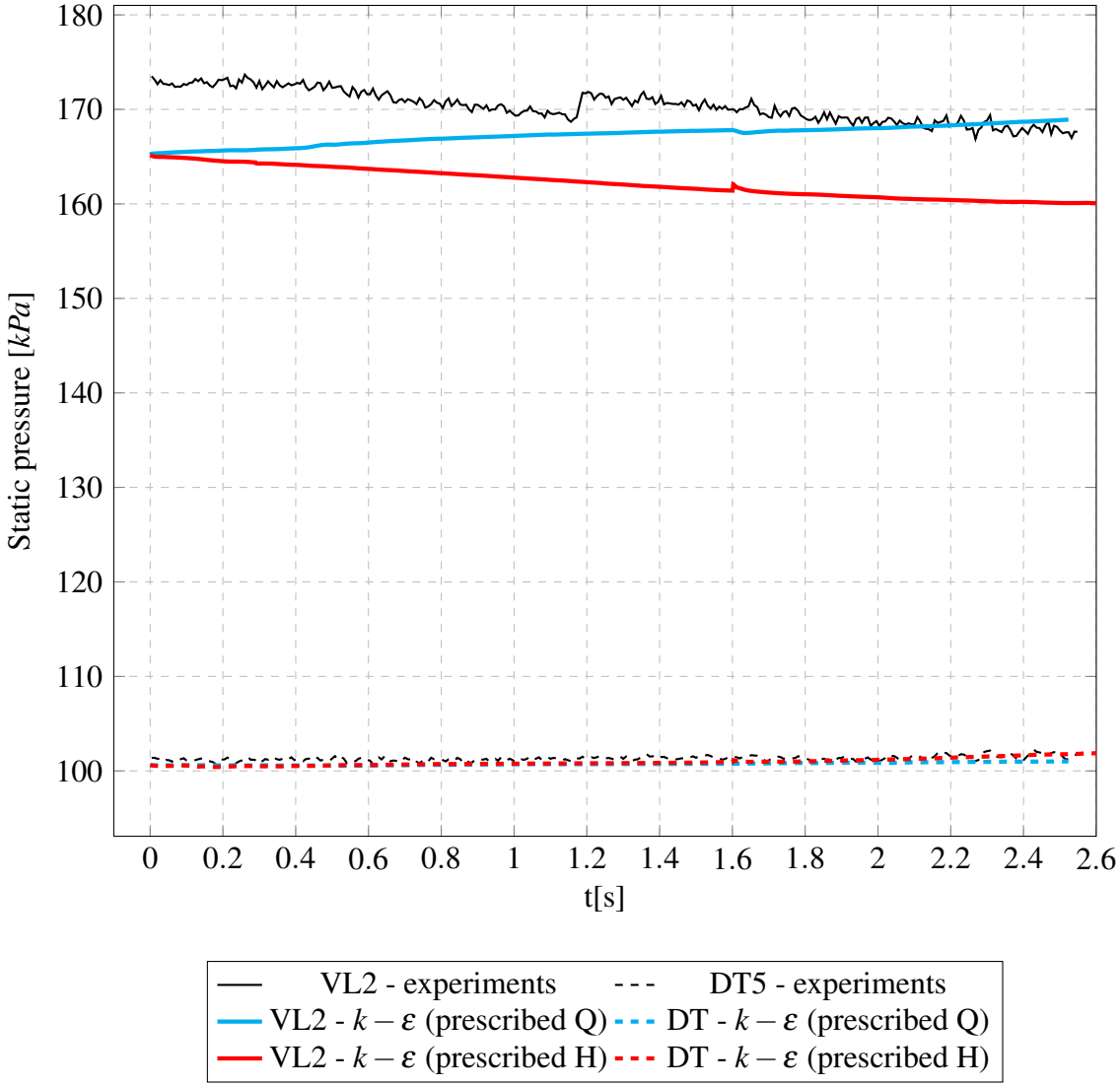

Figure 31: Static pressure (abs) during transient operation, comparison to experimental data.

Measurements of load variation experiments provided by Francis 99 workshop were used to validate the proposed modeling approaches. Figure 31 shows comparison of results at the pressure probe locations. Simulation with prescribed head at the inlet shows good agreement with the

experimental data as the trend in pressure drop matches between the two, suggesting the qualitative agreement between the simulated and real physical processes. Also the values at the draft tube locations do not deviate form the experiments. At the vane-less space (VL2) pressure probe, results show the relative difference of around 5%, matching those in steady state simulations (Fig. 20). Calculated pressure is adjusted for atmospheric conditions. On the other hand, a simulation with prescribed Q shows a pressure rise at the VL2 location which suggests that the simulation setup doesn't correspond to the actual physical process at hand during load reduction.

Experimental measurements appear to have recorded a pressure jump at around 1.2 s after the start of guide vane rotation. Origin of the pressure disturbance is unknown. However, the pressure jump in numerical results at the 1.6 s is due to the mesh substitution, described in Section 3.3.3, which was executed at that time. Mesh requires to be replaced with a new, manually created one due to mesh quality degradation resulting from motion solver reaching a certain insurmountable geometrical obstacle. The artificial pressure jump at 1.6 s originates from field mapping utility not being conservative. The solution converges and recovers from the disturbance quickly. In measured pressure data, except for the unknown step, the transient pulsations of higher frequencies are clearly visible as well. In Section 5.3.2, namely Figure 23a an influence of runner blades passing is observed in form of pressure pulsations with the matching frequency. Transient simulation with a sliding runner grid showed a possibility to resolve those pulsations as seen in Figure 23a. On the other hand, results of load reduction simulations presented in this chapter, Figure 31 show completely smooth pressure profile. This is the result of static gird, multiple reference frames (MRF) modeling used (Section 3.2.1). Regardless of the inability of MRF, being the simpler modeling approach, to capture these finer pressure variations signifying rotor-stator interaction, mean drop of the pressure variable corresponds well to experiments.

Pressure field distribution in the rotor-stator interaction zone is showed in a sequence of cut-field plots in Figure 32. A slight pressure drop is visible at the VL2 location in these pictures as well.

On the other hand, gauge pressure field evolution in Figure 33 shows much higher rise for the case where velocity is prescribed at the inlet surface, regardless of simultaneous drop in inlet velocity as guide vanes are closing (Figure 30). Pressure gradient at the inlet is set to be zero in this setup. With the domain being cut at that particular place, that is, at the guide vane inlet, this assumption is easily seen as erroneous. With pressure being of elliptic nature, it's values are transported both upstream and downstream. Each point is at the same time dependent on all other points in the domain and determines values of all other points. By cutting the domain at this unfavorable position, the communication with upstream section is lost and with it the ability for pressure to stabilize. It can be expected that the rise in pressure due to guide vane closing would propagate gradually upstream if the flow domain included the spiral channel part.

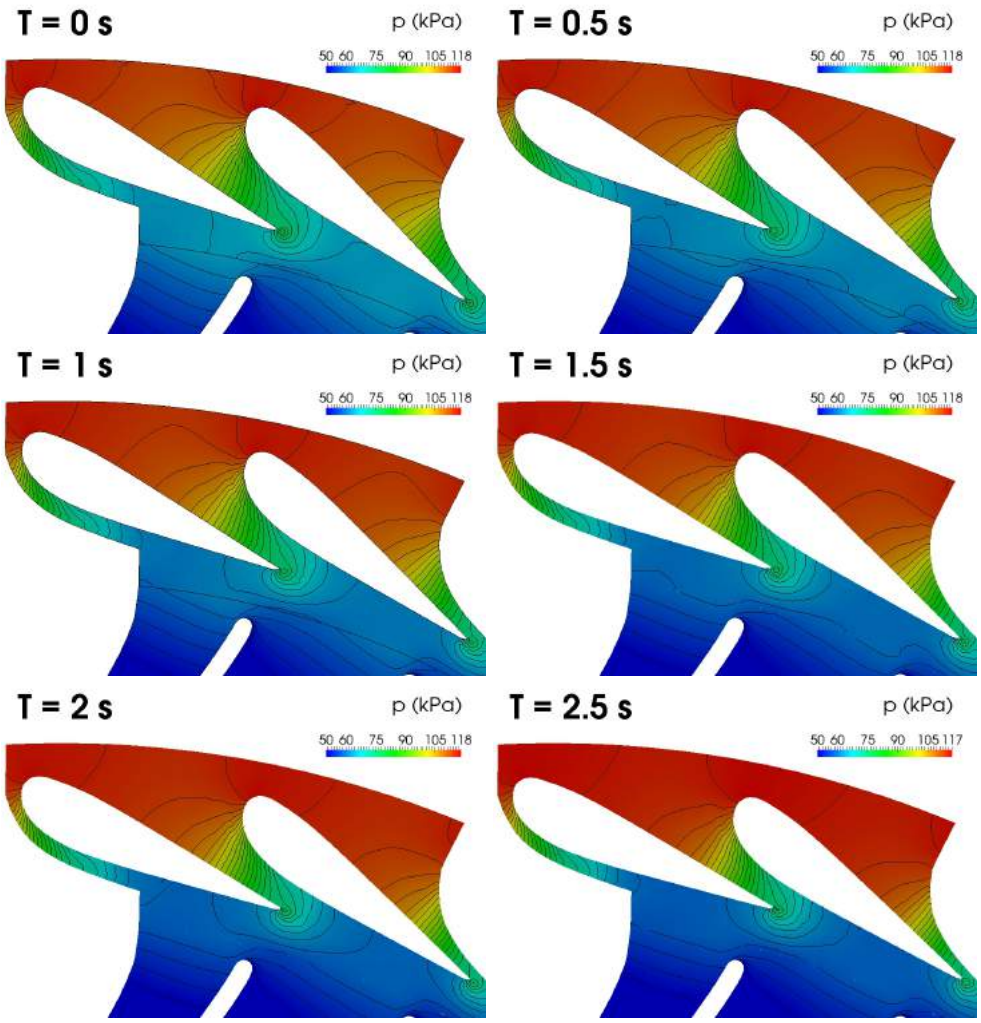

Figure 32: Gauge pressure field distribution around guide vanes for simulation with prescribed head.

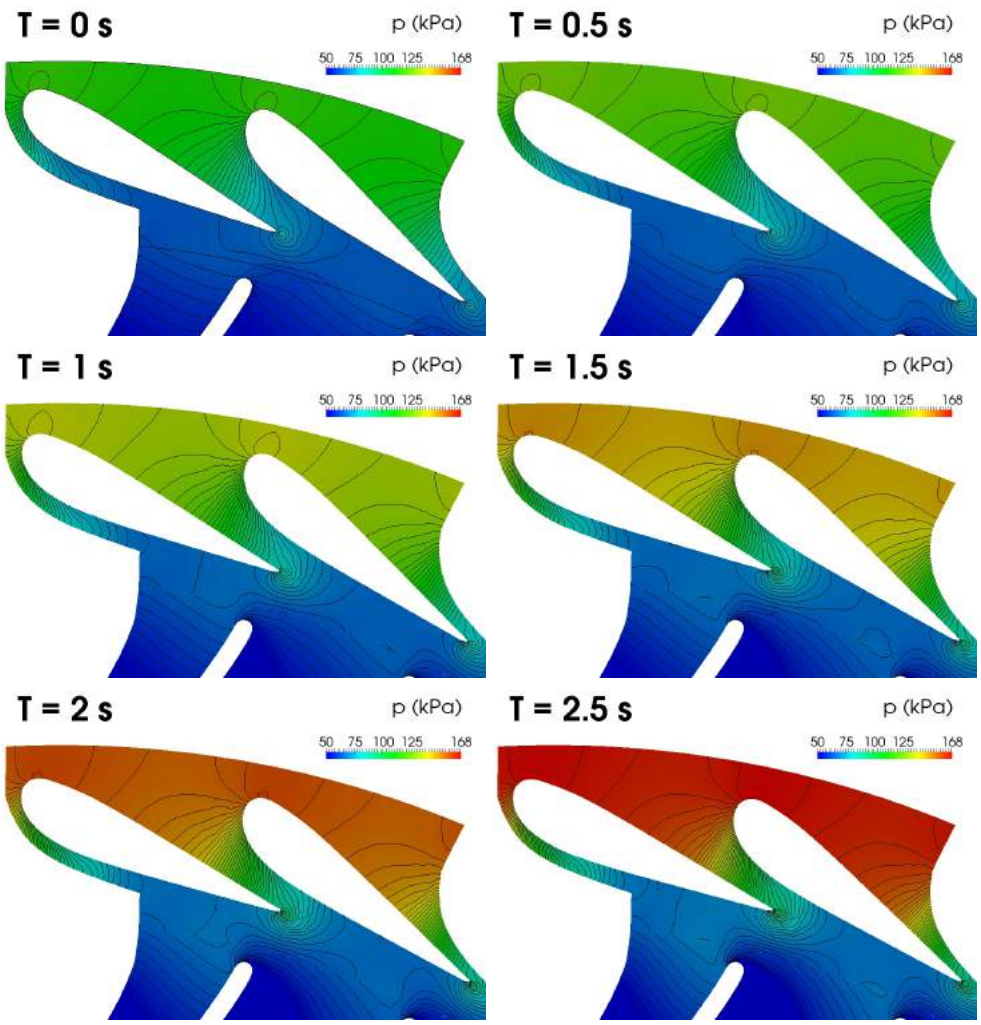

Figure 33: Gauge pressure field distribution around guide vanes for simulation with prescribed flow rate.

The rise in pressure propagates freely downstream in Fig. 33 consequently rising the pressure at the runner blade position. Paradoxically, this would increase the turbine power output in the load reduction phase, clearly marking the model's inability to capture the process, deeming the approach with setting the experimentally determined discharge curve at the inlet together with guide vane rotation deprecated for this particular domain.

6.3.2 Variation of Integral Values During Load Reduction

In the simulation setup with prescribed head as a total pressure at the inlet (Sec. 6.1.1), velocity magnitude is a function of pressure difference as described in Section 3.4.2. The turbine flow rate is consequently being calculated by the model. Figure 34 shows the results of this simulation. It can be observed that calculated value of discharge reaches the similar end result as in provided experimental data, however in the simulations the entire change of flow rate is accomplished during simulation time of 2.6 *s*, while experimental data show this transient response to last more then 9 *s* (the gradient at the end of exp. values curve suggests further decrease). Also the profile is not linear as suggested by the numerical model. These differences can arise from the choice of computational domain. With reduction of its size the system's inertia is reduced. Also a number of other influences are neglected such as draft tube elbow, spiral channel and stay vane losses which can make the response profile non-linear. Further investigations on a full turbine model are needed to determine the validity of these assumptions.

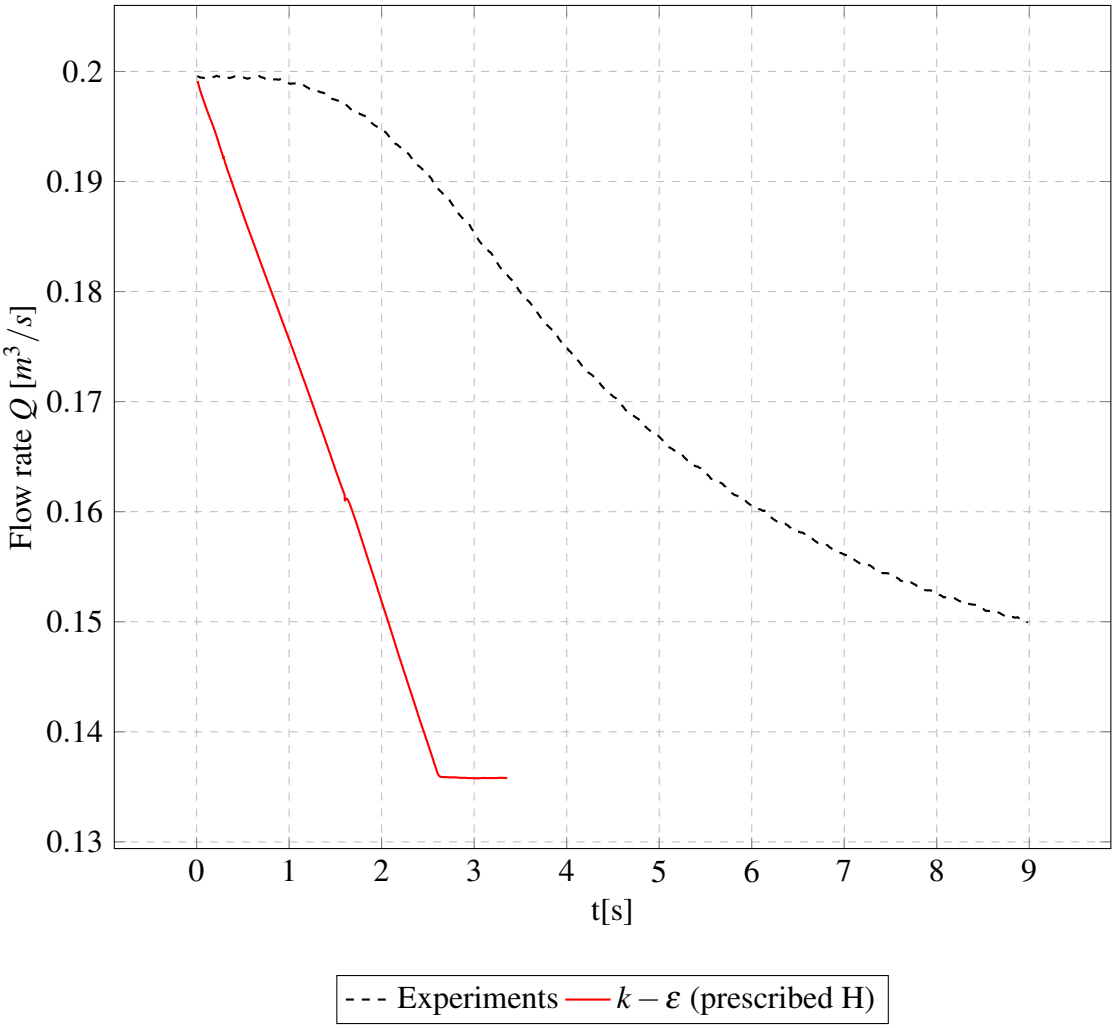

Figure 34: Flow rate during load reduction phase.

The difference between the end result of calculated and experimental flow rate can be attributed to both premature end of measurements (the flow rate still decreases at the end) and more importantly, the probable overestimation of vortical structure causing the resistance to flow. At part load, and in general further from BEP, more flow separation and complex flow structures can be expected, making it a more difficult task for "two equation" turbulence models, used in this study, to accurately predict the flow variables.

Turbine performance characteristics confirm all observations from load reduction results previously presented in this chapter. With discharge decrease and runner rotation speed constant power decreases linearly (Figure 35a). Both efficiency and power curves demonstrate the influence of nonconservative mapping at at $t = 1.6\ s$, which was discussed in Section 3.3.3 and observed in pressure results (Sec. 6.3.1).

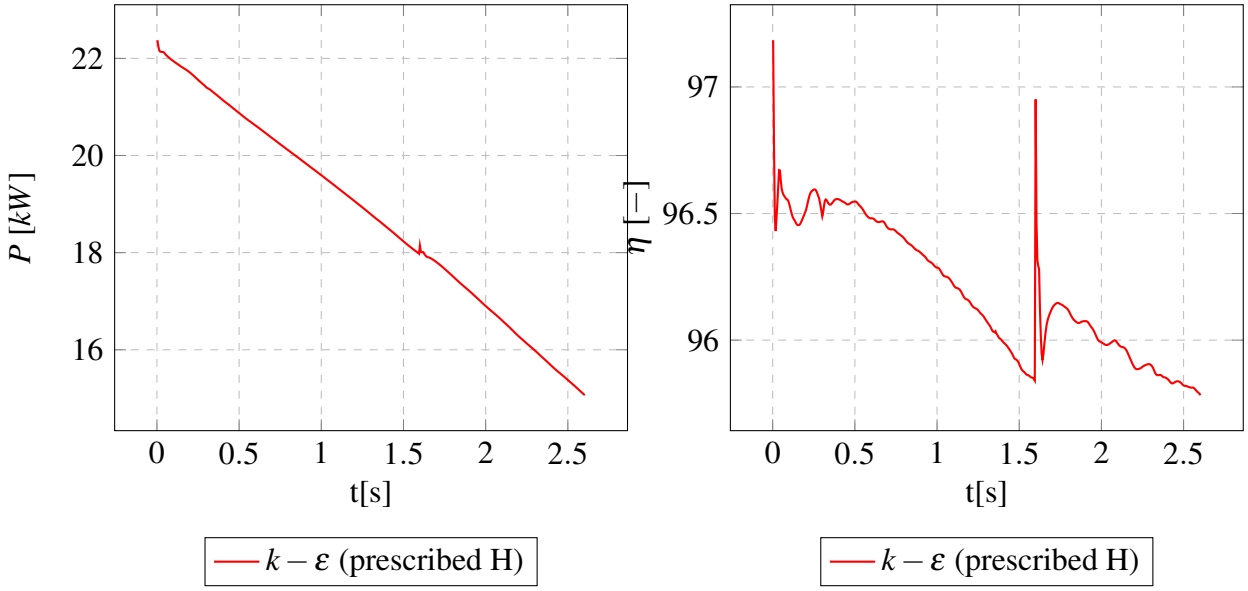

(a) Power [W]

(b) Efficiency (non-adjusted for z, see 5.3.1)

Figure 35: Turbine performance during load reduction phase

7 Conclusion and Future Work

In the course of this thesis, simulations of flow in the Francis 99 high head turbine has been presented. Both steady state and transient operation of turbine were investigated, with load reduction phase in focus of transient regime simulations. An original computational grid was created completely from scratch for this purpose. This was done to avoid some of the quality issues regarding the official Francis 99 meshes, reported in the first workshop papers (Trivedi et al. [14], Stoessel and Nilsson [15]) and to tightly control the requirements for computational resources for present work which were relatively modest. For the same reason most of the simulations were performed on the reduced spatial domain, which included a single representative flow passage. Model of full runner, guide vane and draft tube geometry is used for comparison in steady state calculations. In both computational domains spiral channel with stay wanes was excluded.

Before load variation simulation, best efficiency operating point was simulated with both steady state MRF solvers and a transient dynamic mesh solver implementing sliding grid approach, to test the created mesh and computational domain choices. The results corresponded well with the experimental values in steady state, for both full and reduced domains. Sliding grid simulation with reduced domain showed greater deviation from the measurement data. At steady state, two well established turbulence models were used, namely the "Standard" $k-\varepsilon$ and $k-\omega\ SST$. The difference in efficiency and head calculated with `OpenFOAM` and those reported by Francis 99 can be attributed to influence of height difference on total pressure which is not included in numerical model.

Load variation simulations were conducted on the reduced domain using multiple reference frame model to resolve the runner rotation. This was accomplished by modification of `foam-extend` solver application `pimpleDyMFoam`, the result being named `MRFpimpleDyMFoam`. Two approaches were tested regarding the choice of boundary conditions at the inlet, those were: prescribed head (total pressure) and prescribed flow rate (velocity). Since the used computational domain didn't include a distributor spiral channel, a need for prescribing the inlet at the cylindrical plane between stay and guide vanes was met by case-specific boundary conditions. The simulation with prescribed head showed good agreement with pressure measurements and realistic trend of other integral values. Simulated flow rate drop occurs faster then in an experimental turbine model, while the end result corresponds well. Also, the measured time profile is nonlinear unlike in numerical results. The reason for such different dynamic characteristics is most probably the reduction of computational domain, which changed the overall system inertia, and excluded some of the effects of spiral channel and draft tube losses. Next step would be to repeat the simulations for the entire turbine domain to test this hypothesis.

Creating a detailed CFD simulation of an entire real-world turbine example is normally a task for computational models with tens of millions of control volumes and work stations with serious

computational capabilities. In order to circumvent the need for such capacities, an approach with careful choice of both computational domain and boundary conditions was designed and tested. One of the goals of this thesis was to make an attempt at creating a minimum working example of Tokke turbine transient operation simulation, which would still be viable and offer results and insights useful for industry or other interested parties. It is a sincere hope of the author that present work makes a step in that direction.

Capabilities of an `OpenFOAM` community driven fork `foam-extend` to handle guide vane rotation with its mesh motion solver are validated in present work. Combining the mentioned solver with mesh motion of the runner (with sliding grid between rotor an stator meshes) would be the next proposed approach to investigate. In this way a method to capture the instantaneous effect of both the global pressure change from load variation and smaller pulsations of higher frequencies, such as those originating from rotor-stator interaction. Only one transient operation scenario, that of the load reduction, was simulated in present work. The presented method of discharge control using moving guide vanes should be useful for other scenarios as well, such as turbine startup, shutdown, load acceptance, load rejection, turbine runaway, etc. A method for simulating flow driven rotation was developed for `foam-extend` by Krane [30] in which variable rotational motion of the runner is calculated based on acting forces, from both fluid loads and shaft torque. Coupling this method successfully with guide vane rotation driven discharge presented in this work could open a new range of possibilities for realistic simulations of different turbine operation control scenarios and their evaluation on the basis of the influence on component life expectancy. Another possible route for expanding on present work is coupling the simulated flow physics with structural mechanics calculation into a fully coupled fluid-structure interaction model, for turbine part loading prediction.

References

[1] Gagnon, M., Tahan, S. A., Bocher, P., Thibault, D., Impact of startup scheme on francis runner life expectancy, IOP Conference Series: Earth and Environmental Science 12 (1) (2010) 012107.

[2] Weller, H. G., Tabor, G., Jasak, H., Fureby, C., A tensorial approach to computational continuum mechanics using object-oriented techniques, Computers in physics 12 (6) (1998) 620–631.

[3] Jasak, H., Jemcov, A., Tuković, Ž., Openfoam: A c++ library for complex physics simulations, in: Proceedings of International workshop on coupled methods in numerical dynamics, Vol. 1000, 2007, pp. 1–20.

[4] Jasak, H., Beaudoin, M., Openfoam turbo tools: From general purpose cfd to turbomachinery simulations, in: Proceedings of SME-JSME-KSME 2011 Joint Fluids Engineering Conference, American Society of Mechanical Engineers, 2011, pp. 1801–1812.

[5] Development of a generalized grid interface for turbomachinery simulations with openfoam.

[6] Nilsson, H., Evaluation of openfoam for cfd of turbulent flow in water turbines, in: Proceedings of 23. IAHR Symposium, 2006.

[7] Petit, O., Towards full predictions of the unsteady incompressible flow in rotating machines, using OpenFOAM, *Phd Thesis*, Chalmers University of Technology, 2012.

[8] Page, M., Beaudoin, M., Giroux, A.-M., Steady-state capabilities for hydroturbines with openfoam, International Journal of Fluid Machinery and Systems 4 (1) (2011) 161–171.

[9] Tuković, Ž., Finite volume method on domains of varying shape, Ph.D. thesis, PhD thesis, University of Zagreb, Croatia (2005).

[10] Tuković, Ž., Jasak, H., A moving mesh finite volume interface tracking method for surface tension dominated interfacial fluid flow, Computers & fluids 55 (2012) 70–84.

[11] Jasak, H., Tuković, Ž., Automatic mesh motion for the unstructured finite volume method, Transactions of FAMENA 30 (2) (2006) 1–20.

[12] Kolšek, T., Duhovnik, J., Bergant, A., Simulation of unsteady flow and runner rotation during shut-down of an axial water turbine, Journal of Hydraulic Research 44 (1) (2006) 129–137.

[13] Trivedi, C., Cervantes, M. J., Gandhi, B., Dahlhaug, O. G., Experimental and numerical studies for a high head francis turbine at several operating points, Journal of Fluids Engineering 135 (11) (2013) 111102.

[14] Trivedi, C., Cervantes, M. J., Dahlhaug, O. G., Experimental and numerical studies of a high-head francis turbine: A review of the francis-99 test case, Energies 9 (2) (2016) 74.

[15] Stoessel, L., Nilsson, H., Steady and unsteady numerical simulations of the flow in the tokke francis turbine model, at three operating conditions, Journal of Physics: Conference Series 579 (1) (2015) 012011.

[16] Mössinger, P., Jester-Zürker, R., Jung, A., Investigation of different simulation approaches on a high-head francis turbine and comparison with model test data: Francis-99, Journal of Physics: Conference Series 579 (1) (2015) 012005.

[17] Wallimann, H., Neubauer, R., Numerical study of a high head francis turbine with measurements from the francis-99 project, Journal of Physics: Conference Series 579 (1) (2015) 012003.

[18] Nicolle, J., Cupillard, S., Prediction of dynamic blade loading of the francis-99 turbine, Journal of Physics: Conference Series 579 (1) (2015) 012001.

[19] Buron, J. D., Houde, S., Lestriez, R., Deschênes, C., Application of the non-linear harmonic method to study the rotor-stator interaction in francis-99 test case, Journal of Physics: Conference Series 579 (1) (2015) 012013.

[20] Amstutz, O., Aakti, B., Casartelli, E., Mangani, L., Hanimann, L., Predicting the performance of a high head francis turbine using a fully implicit mixing plane, Journal of Physics: Conference Series 579 (1) (2015) 012009.

[21] Ferziger, J., Perić, M., Computational Methods for Fluid Dynamics, Springer Berlin Heidelberg, 2001.

[22] Jones, W., Launder, B., The prediction of laminarization with a two-equation model of turbulence, International journal of heat and mass transfer 15 (2) (1972) 301–314.

[23] Menter, F. R., Two-equation eddy-viscosity turbulence models for engineering applications, AIAA journal 32 (8) (1994) 1598–1605.

[24] Launder, B. E., Spalding, D., The numerical computation of turbulent flows, Computer methods in applied mechanics and engineering 3 (2) (1974) 269–289.

[25] Dixon, S. L., Hall, C., Fluid mechanics and thermodynamics of turbomachinery, Butterworth-Heinemann, 2013.

[26] Jasak, H., Rusche, H., Dynamic mesh handling in openfoam, in: Proceeding of the 47th Aerospace Sciences Meeting Including the New Horizons Forum and Aerospace Exposition, Orlando, FL, 2009.

[27] Saraf, A., Nilsson, H., Transient simulation of opening and closing guide vanes of a hydraulic turbine, in: "CFD with Opensource Software" course technical report, 2016.

[28] Francis 99 test case.
URL `https://www.ntnu.edu/nvks/test-case`

[29] swak4foam library.
URL `https://openfoamwiki.net/index.php/Contrib/swak4Foam`

[30] Krane, E., Simulations of the flow-driven rotation of the Francis-99 turbine runner, *Master's Thesis*, Chalmers University of Technology, 2015.